



저작자표시-비영리-변경금지 2.0 대한민국

이용자는 아래의 조건을 따르는 경우에 한하여 자유롭게

- 이 저작물을 복제, 배포, 전송, 전시, 공연 및 방송할 수 있습니다.

다음과 같은 조건을 따라야 합니다:



저작자표시. 귀하는 원 저작자를 표시하여야 합니다.



비영리. 귀하는 이 저작물을 영리 목적으로 이용할 수 없습니다.



변경금지. 귀하는 이 저작물을 개작, 변형 또는 가공할 수 없습니다.

- 귀하는, 이 저작물의 재이용이나 배포의 경우, 이 저작물에 적용된 이용허락조건을 명확하게 나타내어야 합니다.
- 저작권자로부터 별도의 허가를 받으면 이러한 조건들은 적용되지 않습니다.

저작권법에 따른 이용자의 권리와 책임은 위의 내용에 의하여 영향을 받지 않습니다.

이것은 [이용허락규약\(Legal Code\)](#)을 이해하기 쉽게 요약한 것입니다.

[Disclaimer](#)



공학박사 학위논문

**Mechanistic Investigation of
Water Oxidation on Manganese Oxide
Nano-catalysts by Impedance Spectroscopy**

임피던스 분석을 통한 망간 산화물 기반
나노 촉매의 물 산화 반응 메커니즘 규명

2021년 2월

서울대학교 대학원
재료공학부

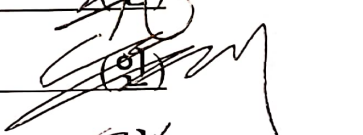
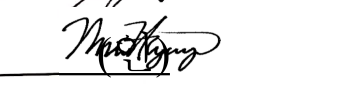
서 흥 민

Mechanistic Investigation of Water Oxidation on Manganese Oxide Nano-catalysts by Impedance Spectroscopy

지도 교수 남기태
이 논문을 공학박사 학위논문으로 제출함
2021년 2월

서울대학교 대학원
재료공학부
서홍민

서홍민의 박사 학위논문을 인준함
2021년 2월

위 원장 장호원 
부위원장 남기태 
위 원 김진영 
위 원 이민형 
위 원 최창혁 

Abstract

Mechanistic Investigation of Water Oxidation on Manganese Oxide Nano-catalysts by Impedance Spectroscopy

Hongmin Seo

Department of Materials Science and Engineering

The Graduate School

Seoul National University

Electrocatalysis plays a crucial role in value-added chemical production and clean energy conversion for future technologies. Hydrogen energy has been regarded as one of attractive candidates for alternative energy source of the next generation due to environmentally characteristics and high energy density. The great part of hydrogen energy was produced by gas reforming process, which needs high temperature and high pressure with unavoidable emission of CO₂ and other pollutants. Electrochemical water splitting is promising approach to obtain hydrogen energy without undesired byproducts. In the overall water electrolysis scheme, hydrogen and oxygen evolution reactions occur as cathodic and anodic half reaction, respectively.

The oxygen evolution reaction (OER) is regarded as major bottleneck for water electrolysis technique. Four electrons and protons are involved in its complex reaction mechanism with large overpotential, compared to hydrogen evolution

reaction. Therefore, highly efficient electrocatalysts need to be developed to reduce large overpotenail for OER. The noble metal based electrocatalysts, such as RuO₂ and IrO_x, are known to exhibit good OER performance, but their scarcity and high cost are regarded as limitation to apply energy conversion industry. Thus, large research effort has been devoted to synthesize transition metal-based electrocatalysts.

On the other hand, manganese attracts considerable attention to achieve high catalytic performance for OER. Manganese is the third most abundant transition metal in the earth. Also, Mn₄CaO₅ clusters in Photosystem II show exceptionally high efficieny for OER compared to artificial electrocatalysts. Inspired by Mn₄CaO₅ clusters, copious Mn-based electrocatalysts have been developed to achieve superior efficiency. However, most Mn-based catalysts showed activity degradation under neutral condition. Therefore, mechanistic investigation and finding key descriptors are important issue to synthesize remarkable Mn-based catalysts.

Our group reported the sub 10 nm-sized Mn oxide nano-catalysts with bengin OER activity in neutral condition in. Futhermore, using electrokinetic studies and *in situ* spectroscopic analyses, we investigated different reaction mechanism on Mn oxide nano-catalysts from conventaional Mn-based catalysts. Here, we performed electrochemical impedance spectroscopy (EIS) to explore multiple electrochemical processes which occur in the Mn oxide nano-catalyst film.

In chapter 2, we conducted EIS analysis for film-type Mn₃O₄ nano-catalysts using our proposed circuit model. From fitting analysis, we can obtain meaningful physical parameters, interface resistance (R_{int}) & capacitance (C_{int}), electron transport resistance (R_{tr}) and reaction rate constant (k). We got three decisive clues for catalytic behavior of Mn₃O₄ NPs from these physical parameters. The overall OER performance for film-type catalysts was determined by the competition between surface catalysis and electron transport process. Also, based on the H/D

isotope experiment, we can conclude that proton are involved in the electron transport process across the nanoparticle film, which directly prove the ongoing hypothesis of oxo-hopping mechanism. Furthermore, we evaluated reaction rate constant (k) for OER catalysis on the film-type electrocatalysts, which represents intrinsic kinetics for surface catalysis.

In chapter 3, we analyzed complex capacitance on Mn_3O_4 nanoparticles (NPs) to understand charge accumulation process during oxygen evolving catalysis. Importantly, charge accumulation is mainly attributed to valency change for active metal center, which plays a crucial role in determining overall catalytic performance for film-type electrocatalysts. We established new parameter, dissipation ratio ($D = \text{Real C} / \text{Imaginary C}$), to demonstrate competition between charge accumulation and dissipation process on Mn_3O_4 nanoparticles with various applied potential and thicknesses. This electrokinetic analysis and mechanism understanding is based on electrochemical impedance spectroscopy (EIS) without equivalent circuit model, that can be generalized to film-type electrocatalysts.

In conclusion, we analyzed various electrochemical processes for Mn_3O_4 NPs catalysts by electrochemical impedance spectroscopy. Our methodology could provide platform to investigate detailed mechanism for the general film-type electrocatalysts.

Keywords: Manganese oxide, Water Oxidation, Electrocatalysts, Mechanistic study, Electrochemical Impedance Spectroscopy

Student Number: 2015-20828

Contents

List of Figures	viii
-----------------------	------

Chapter 1 Introduction	1
------------------------------	---

1.1	The alternative energy source for sustainable energy future ..	1
1.2	Hydrogen energy as future alternative energy source.....	2
1.3	Electrochemical water splitting reaction.....	3
1.3.1	Water electrolysis techniques for hydrogen production	3
1.3.2	General description for electrochemical water splitting.....	7
1.3.3	The hydrogen evolution reaction (HER)	9
1.3.4	The oxygen evolution reaction (OER)	14
1.4	Electrocatalysts for oxygen evolution reaction.....	15
1.4.1	The necessity for the development of OER electrocatalysts	15
1.4.2	Design rule for OER electrocatalysts	17
1.4.3	Reaction mechanism for electrochemical water oxidation...	22
1.5	Lessons in biological system: Photosystem II	28
1.5.1	Introduction to photosystem process.....	28
1.5.2	Water oxidizing catalysis for Mn ₄ Ca cluster	31
1.5.3	Structural characteristic for Mn ₄ Ca cluster	32
1.5.4	Electronic structure change during catalysis	35
1.6	Artificial Mn based electrocatalysts for OER.....	39

1.6.1	Mn-based electrocatalysts with crystalline structure.....	42
1.6.2	Mn-based electrocatalysts with disordered structure	47
1.6.3	Key factors for OER activity in Mn based electrocatalysts .	52
1.7	The sub 10 nm-sized Mn oxide nano-catalysts.....	55
1.7.1	OER activity for Mn oxide nanoparticles.....	55
1.7.2	Reaction mechanism on the Mn oxide nanoparticles	59
1.8	Electrochemical impedance spectroscopy for OER electrocatalysts	69
1.9	Scope of thesis	73
1.10	Concluding remarks	75

Chapter 2 Parametric studies on Mn oxide nanocatalysts using equivalent circuit model

2.1	Introduction.....	76
2.2	Experimental Methods	84
2.2.1	Materials.....	84
2.2.2	Synthesis of the Mn_3O_4 NPs.....	84
2.2.3	Electrode fabrication	85
2.2.4	Scanning electron microscopy (SEM).....	85
2.2.5	Transmission electron microscopy (TEM)	86
2.2.6	Electrochemical measurement.....	86
2.3	Results and Discussions.....	88
2.3.1	Structural analysis and catalytic activityof the Mn_3O_4 NPs ..	88

2.3.2	OER activity for the Mn ₃ O ₄ NPs with various thickness	93
2.3.3	Impedance analysis for the Mn ₃ O ₄ NPs catalyst film.....	95
2.3.4	Our proposed circuit model	105
2.3.5	Fitting results for our proposed circuit model	111
2.4	Concluding Remarks.....	142

Chapter 3 Complex capacitance analysis for charging process with
Mn valency change during catalysis143

3.1	Introduction	143
3.2	Results and Discussions	149
3.2.1	Mn valency change on Mn ₃ O ₄ NPs during catalysis.....	149
3.2.2	Complex capacitance analysis from EIS.....	154
3.2.3	Dissipation ratio (D = C' / C'') for OER onset potential ...	167
3.4	Concluding Remarks.....	172

Chapter 4 Conclusion173

References175

국문 초록	182
-------------	-----

List of Figures

- Figure 1.1.** Schematic illustration of three main types of water electrolysis (a) Alkaline electrolysis cell, (b) Solid oxide cell, (c) Proton exchange membrane cell6
- Figure 1.2.** Schematic of the current to potential curve of overall water splitting reaction.....8
- Figure 1.3.** Experimentally measured exchange current, $\log (J_0)$, for hydrogen evolution over different catalyst plotted as a function of the calculated the free energy for hydrogen adsorption.12
- Figure 1.4.** (a) HER volcano trend for metals and MoS₂ (b) TOF_{avg} plots with linear sweep voltammetry curves for previously reported HER electrocatalysts13
- Figure 1.5.** (a) Overpotential values of reported electrocatalysts for hydrogen evolution raction and oxygen evolution reaction (b) The chronological tend in overpotential of various OER electrocatalysts in acidic and alkaline condition16
- Figure 1.6.** Activity trends towards oxygen evolution reaction for various oxides including rutile, anatase, Co₃O₄, Mn_xO_y oxides.19
- Figure 1.7.** Activity trends towards oxygen evolution reaction for perovskite-type catalysts. The OER activity is defined by the overpotential at 50 μ A cm⁻² state.....20
- Figure 1.8.** The volcano plot for experimental overpotential values of metal-

oxide based electrocatalysts. The OER activity is defined by the overpotential at 1 mA cm ⁻²	21
Figure 1.9. Schematic representation of water oxidation mechanism (a) Acid-Base (AB) mechanism and (b) Radical-Coupling (RC) mechanism for O-O bond formation	27
Figure 1.10. Schematic representation of Photosynthetic process in photosystem. (a) Scheme of Z-schematic electron flow in light reaction (b) energy diagram of Z-schematic electron flow.....	30
Figure 1.11. The Kok cycle with spectroscopically consistent structures of the Mn cluster and their spin states.....	37
Figure 1. 12. Structural model for all S _i states of the Mn cluster: atomic structure of the Mn cluster, Mn-Mn distances(Å) of optimized geometries, the nature of magnetic couplings(AF for antiferromagnetic coupling and F for ferromagnetic coupling), and total spin numbers respectively. (c) Proposed S ₃ intermediate states upon S ₂ -S ₃ transition. The loss of the Asp61/W1 hydrogen bond with subsequent low-barrier water insertion via the Asp61 channel and rearrangement is involved	38
Figure 1. 13. (a) Crystal structure of the various manganese oxides, MnO, Mn ₃ O ₄ , Mn ₂ O ₃ and MnO ₂ (b) Crystal tstructure of various MnO ₂ polymorphs	40
Figure 1.14. Calculated Pourbaix diagram of Mn-O-H phases.	41
Figure 1.15. (a) Demonstration of the crystal structure and d-orbital electronic configuration of Mn ₂ O ₃ and γ-MnOOH (b) Description of corner-shared Mn(III) octahedral in δ-MnO ₂ . Structureal rearrangement forms active species (corner-sharing Mn(III) octahedra) on the surface	

of δ -MnO ₂	46
Figure 1.16. Calculated electronic structure of disordered δ -MnO ₂ . (a) Crystal structures of Mn ₃ O ₄ and d-MnO ₂ . (b) Band structure of the activated disordered δ -MnO ₂ and δ -MnO ₂ . (d) Calculated average valence state of Mn and O	51
Figure 1.17. (a) pH dependences of the onset potential for oxidation current ($U_{on,j}$, red squares) and optical absorption at 510 nm ($U_{on,A510}$, blue circles). The solid line represents the standard potential for water oxidation (b) Schematic representation of electronic structure change for charge disproportionation and Jahn-Teller distortion (c) Schematic representation for oxidation states of Mn ions involved in the water oxidation on δ -MnO ₂ at pH 4-8 and pH > 9	54
Figure 1.18. Transmission electron microscope (TEM) images for Mn oxide nanoparticles.....	56
Figure 1.19. Transmission electron microscope (TEM) images for Mn oxide nanoparticles with various sizes and polarized cyclic voltammetry curves	57
Figure 1.20. Parallel and perpendicular (inset) mode X-band CW-EPR spectra of Mn oxide NPs (a) in resting state, (c) at 1.3 V vs. NHE and bulk MnO (b) in resting state, (d) at 1.3 V vs. NHE.	58
Figure 1.21. Electro-kinetic analysis for the Mn oxide NPs (a) Tafel plots near the onset potential (b) pH dependency over a neutral pH range (c) a summary table for the estimated proton reaction orders for the Mn oxide NPs with various thicknesses	61
Figure 1.22. In situ electrochemical cell for mechanistic studies on the Mn oxide	

nanoparticles (a) X-ray adsorbtion spectroscopy (XAS) (b) Raman spectroscopy (c) UV-vis spectroscopy.....	63
Figure 1.23. <i>In situ</i> XAS spectra for the Mn oxide nanoparticles during catalysis. (a) XANES analysis (b) EXAFS analysis.. ..	65
Figure 1.24. (a) <i>In situ</i> Raman data and (b) <i>in situ</i> UV-vis spectroscopic data, difference spectra based on the applied potential on the Mn oxide NPs during OER. (c) <i>In situ</i> UV-vis difference spectra of bulk MnO (d) potential dependence of the current density and differential absorabance of 600 nm for the Mn oxide NPs	66
Figure 1.25. Reaction mechanism for electrochemical water oxidation on the conventional Mn-based catalyst (top) and the Mn oxide NPs (bottom)	68
Figure 1.26. (a-c) Electrochemical impedance spectra recorded in 1.0 M NaOH at a series of potentials associated with active oxygen evolution for transition metal hydroxide electrode (d) Equivalent circuit model for fitting analysis (e) Tafel plots generated from EIS and steady-sate polarization data	71
Figure 1.27. Schematic representation for the scope of thesis.....	74

Figure 2.1. Transmission electron microscopy (TEM) image of synthesized Mn ₃ O ₄ NPs	89
Figure 2.2. X-ray diffraction data for synthesized Mn ₃ O ₄ NPs.....	90

Figure 2.3.	Plane sectional scanning electron microscopy (SEM) images of Mn ₃ O ₄ NPs electrode.....	91
Figure 2.4.	Cross sectional scanning electron microscopy (SEM) images of (a) 20 nm- (b) 70 nm- (c) 150 nm- (d) 300 nm- (e) 500 nm-thickness Mn ₃ O ₄ NPs electrode.....	92
Figure 2.5.	Polarization-corrected cyclic voltammetry (CV) curves for the 20, 70, 150, 300 and 500 nm thicknesses	94
Figure 2.6.	Nyquist plot of impedance data for Mn ₃ O ₄ NPs film with the 20, 70, 150, 300 and 500 nm thicknesses at 1.35 V vs. NHE, where OER catalysis occurs briskly	96
Figure 2.7.	Bode plot for phase angle of Mn ₃ O ₄ NPs film with the 20, 70, 150, 300 and 500 nm thicknesses at 1.35 V vs. NHE, where OER catalysis occurs briskly.....	97
Figure 2.8.	Previous circuit model for fitting analysis (a) simple circuit model; (b) the circuit model reported by Cahan and Chen group; (c) the circuit model reported by Lyon group	101
Figure 2.9.	Nyquist plot of the fitting results for the 70, 150, 300 and 500 nm-thickness Mn ₃ O ₄ NPs using the circuit model A.....	102
Figure 2.10.	Nyquist plot of the fitting results for the 70, 150, 300 and 500 nm-thickness Mn ₃ O ₄ NPs using the circuit model B and C	103
Figure 2.11.	The fitting results of dispersion parameters (α_{film} , α_{Φ} , and α_{dl}) for each thickness from the previous circuit model C.....	104
Figure 2.12.	Our proposed circuit model for the impedance analysis of Mn ₃ O ₄	

NPs film. R_{tr} indicates resistance to electron transport in the Mn_3O_4 NPs. R_{int} and C_{int} in the RC loops, which describe surface catalysis, mean the interface resistance and capacitance, respectively. 108

Figure 2.13. Nyquist plots for several thicknesses (70, 150, 300, and 500 nm) of Mn_3O_4 NP films at (a) 1.2 V, (b) 1.25 V, (c) 1.3 V, and (d) 1.35 V vs NHE. Square points indicate the experimental spectra for Mn_3O_4 NPs, and lines represent the fitting results obtained by our proposed circuit model. The black, red, blue, and dark cyan spectra indicate data for 70, 150, 300, and 500 nm thicknesses, respectively 110

Figure 2.14. Interface resistance (R_{int}) for Mn_3O_4 NPs film with various thicknesses (70 nm, 150 nm, 300 nm and 500 nm) at various applying potential (1.2, 1.25, 1.3 and 1.35 V vs. NHE) from fitting analysis with our proposed circuit model 114

Figure 2.15. Transport resistance (R_{tr}) for Mn_3O_4 NPs film with various thicknesses (70 nm, 150 nm, 300 nm and 500 nm) at various applying potential (1.2, 1.25, 1.3 and 1.35 V vs. NHE) from fitting analysis with our proposed circuit model 115

Figure 2.16. Interface capacitance (C_{int}) for Mn_3O_4 NPs film with various thicknesses (70 nm, 150 nm, 300 nm and 500 nm) at various applying potential (1.2, 1.25, 1.3 and 1.35 V vs. NHE) from fitting analysis with our proposed circuit model 117

Figure 2.17. Summary for reported capacitance for several Mn-oxide electrodes 118

Figure 2.18. (a) Planar two electrode configuration with gold electrodes for DC measurement; and (b) I-V curves of Mn_3O_4 NPs in ambient

conditions on planar gold electrodes.....	120
Figure 2.19. (a) Nyquist plot for 150 nm-thickness Mn-oxide NPs film on Au/FTO substrates at 1.25 V vs. NHE in 0.5 M phosphate buffer solution. The black dots and red line indicated experimental data and fitting result using our proposed circuit model. (b) The values for physical parameters (R_{tr} , R_{int} and C_{int}) from fitting with our circuit model.....	121
Figure 2.20. Polarization-corrected cyclic voltammetry curves from 0.7 V to 1.4 V vs. NHE for Mn_3O_4 NPs film of various thicknesses (70, 150, 300 and 500 nm) at 0.5 M phosphate buffer solution under pH 7. (a) H_2O electrolyte (b) D_2O electrolyte	124
Figure 2.21. Nyquist plots for several thickness (70, 150, 300 and 500 nm) of Mn_3O_4 NPs film at 1.35 V vs. NHE in D_2O electrolyte. The black, red, blue and dark cyan spectra were for 70, 150, 300 and 500 nm-thickness, respectively.....	125
Figure 2.22. Comparison between transport resistance (R_{tr}) for Mn_3O_4 NPs in H_2O and D_2O electrolyte.....	126
Figure 2.23. Relaxation time constant for the OER kinetics of Mn_3O_4 NPs catalyst film	128
Figure 2.24. Reaction rate constant (k) for the OER kinetics of Mn_3O_4 NPs catalyst film	131
Figure 2.25. Scheme of reaction mechanism for OER on the Mn_3O_4 NPs and reaction-determining step for O-O bond formation.....	132
Figure 2.26. Double-layer capacitance measurements for determining	

electrochemically active surface area for 300 nm-thickness Mn_3O_4 NPs film. (a) Cyclic voltammetry was measured in a non-Faradaic region at the following scan rates: 0.5 (purple line), 1 (magenta line), 2.5 (dark cyan line), 5 (blue line), 7.5 (red line), and 10 (black line) mV/s. (b) The cathodic (■) and anodic (●) charging current density measured at 0.645 V (open-circuit potential) are plotted as a function of scan rates..... 138

Figure 2.27. Schematic illustration for scanning electrochemical microscopy (SI-SECM) for Co-Pi catalysts..... 139

Figure 2.28. Nyquist plot for Co-Pi at various applying potential (1.2 V, 1.25 V, 1.3 V and 1.35 V vs. NHE) during OER catalysis..... 140

Figure 2.29. Reaction rate constant (k) for Co-Pi catalyst and Mn_3O_4 NPs at various applying potential (1.2, 1.25, 1.3 and 1.35 V)..... 141

Figure 3.1. The schematic illustration of proposed oxygen evolving reaction mechanism on Mn_3O_4 NPs 151

Figure 3.2. Cyclic voltammetry curve for 70 nm-thickness Mn_3O_4 NPs electrodes under 0.5 M phosphate buffer solution (pH 7) ... 152

Figure 3.3. Cyclic voltammetry curves for Mn_3O_4 NPs on FTO substrates with (a) 20 nm- (b) 150 nm- and (c) 300 nm-thickness in 0.5 M phosphate buffer solution (pH 7). 153

Figure 3.4. Nyquist plots (Z' vs Z'') for 70 nm-thickness Mn_3O_4 nanoparticles film at open circuit potential, 0.8, 1.0, 1.2, 1.25, 1.3 and 1.35 V vs.

NHE	157	
Figure 3.5.	Complex capacitance (C' vs C'') plots for 70 nm-thickness Mn_3O_4 nanoparticles film at open circuit potential, 0.8, 1.0, 1.2, 1.25, 1.3 and 1.35 V vs. NHE.....	158
Figure 3.6.	Nyquist plots (Z' vs Z'') for (a) 20 nm- (b) 150 nm- (c) 300 nm-thickness Mn_3O_4 NPs film at open circuit potential, 0.8, 1.0, 1.2, 1.25, 1.3 and 1.35 V vs. NHE.....	159
Figure 3.7.	Complex capacitance plots (C' vs C'') for (a) 20 nm- (b) 150 nm- (c) 300 nm-thickness Mn_3O_4 NPs film at open circuit potential, 0.8, 1.0, 1.2, 1.25, 1.3 and 1.35 V vs. NHE	160
Figure 3.8.	(a) Real part (C') and (b) Imaginary part (C'') for complex capacitance as a function of log (Freq / Hz) at open circuit potential (OCP), 0.8, 1.0, 1.2, 1.25, 1.3 and 1.35 V vs. NHE	162
Figure 3.9.	(a) Real part (C') and (b) Imaginary part (C'') for complex capacitance as a function of log (Freq / Hz) under OER onset potential (≤ 1.0 V vs. NHE) (c) Scheme for OER mechanism on the Mn_3O_4 NPs	163
Figure 3.10.	(a) Real part (C') and (b) Imaginary part (C'') for complex capacitance as a function of log (Frequency / Hz) under OER onset potential (≥ 1.2 V vs. NHE) (c) Scheme for OER mechanism on the Mn_3O_4 NPs	166
Figure 3.11.	Dissipation ratio (C'/C'') as a function of frequency for 70 nm-thickness film at open circuit potential (OCP), 0.8, 1.0, 1.2, 1.25, 1.3 and 1.35 V vs. NHE	169

Figure 3.12. Dissipation ratio (C'/C'') as a function of frequency with 20 nm-, 70 nm-, 150 nm- and 300 nm-thickness..... 170

Figure 3.13. (a) D_{\max} and (b) $\log(f_{\max}/\text{Hz})$ at open circuit potential (OCP), 0.8, 1.0, 1.2, 1.25, 1.3 and 1.35 V vs. NHE with 20 nm-, 70 nm-, 150 nm- and 300 nm-thickness..... 171

Chapter 1. Introduction

1.1 The alternative energy source for sustainable energy future

Development of alternative energy source is challenging issue for sustainable future due to the significant increase in energy consumption. The global energy consumption reached 18 TW in 2013 and is expected to 26 TW in 2040, 43 TW in 2100 with world population growth and expansion of industrialization.^[1] Presently, enormous amount of fossil fuels is depleted and emitted greenhouse gases, such as carbon dioxide, which causes climate change problem. Carbon dioxide emission reached 32Gt year⁻¹ in 2013 and is expected to 37~44 Gt year⁻¹ in 2040.^[2] Reducing carbon dioxide emissions is challenging issue to solve the global warming problem. From the Paris Climate Convention held in December 2015, the number of countries subject to carbon dioxide reduction has been expanded and Korea. Korea was the eighth largest emitter of carbon dioxide among the G20 countries, but decided to reduce carbon dioxide emissions by 37% by 2030. In light of this, sustainable and clean energy source have to be developed to reduce our reliance on fossil fuels.

1.2 Hydrogen energy as future alternative energy source

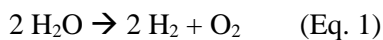
Hydrogen energy has been regarded as attractive alternative energy source for future sustainable energy technology. When hydrogen energy is used, byproducts are water, heat and electricity without CO₂ emission. Hydrogen shows environmentally friendly and non-toxic characteristic while nuclear energy, coal, and gasoline are toxic or hazardous for environment. Also, hydrogen energy is very efficient fuel source than traditional sources of energy. It has high energy density of 142 kJ/g while gasoline has energy density of 46 kJ/g and natural gas has energy density of 47.2 kJ/g.^[3] To apply hydrogen energy in industry, Korean government established hydrogen-energy development roadmap in January 2019. In this roadmap, Hydrogen production is projected to increase to 1.94 million tons in 2030 and 5.26 million tons in 2040.

1.3 Electrochemical water splitting reaction

1.3.1. Water electrolysis technique for hydrogen production

Hydrogen can be produced various energy sources, such as oils, natural gas, coal and biomass (Table 1). Currently, most of hydrogen production has been obtained by gas reforming process. Specifically, above 90 % of total hydrogen is produced by gas reforming process which emits carbon dioxide with high temperature and high pressure. About 4% of total hydrogen is produced by water electrolysis without harmful byproducts.

Water electrolysis is regarded as the most sustainable way to produce hydrogen energy, because it requires electricity and water and the only byproduct is pure oxygen. (Eq. 1) In detail, hydrogen is evolved from two protons as the cathodic half reaction and oxygen is generated with charge transfer of four electrons and protons as the anodic half reaction.



Water electrolysis technologies are classified into three broad types depending electrolytes, operating temperature. There are alkaline electrolysis, proton exchange membrane electrolysis and solid oxide electrolysis.

Firstly, alkaline electrolysis cell is composed of two separate electrodes operating in an alkaline electrolyte. The operating temperature for alkaline electrolysis is 40~90°C.^[4] The advantages of alkaline electrolysis technique are using less expensive catalysts, long-term stability and low-cost of overall system, compared to

other water electrolysis techniques. Thus, it has been already developed technology and used for industrial application. The operating efficiency is reported to about 50~82%. However, alkaline electrolysis still have several limitations for industrial expansion. Its current density and partial load range are low. Liquid electrolyte causes corrosion of system. Additionally, crossover of produced gas can reduce efficiency of overall system.

Secondly, proton exchange membrane (PEM) electrolysis utilized polymer membrane for proton conduction.^[5] The PEM electrolyzer is composed of membrane electrode assembly, gas diffusion layers and bipolar plates. The membrane electrode assembly (MEA) includes acidic polymeric membrane, anode and cathode electrodes. Specifically, the structure of polymeric membrane includes cross-linked structure and functional group of the sulfonic acid, which is stable in acidic condition. Protons are exchanged through the membrane by an ion exchange mechanism. The Nafion is well-known membrane for PEM electrolyzer. The operating temperature is generally about 20~100°C.^[4] The advantages for PEM electrolysis are high current density, voltage efficiency and gas purity.

Lastly, solid oxide electrolysis generally operates at higher temperature, 500 ~ 1000°C.^[4] It utilized ceramic membrane than can mobilize oxygen anion. The technology for solid oxide electrolysis cell (SOEC) is still immature and further research is needed, compared to other water electrolysis techniques (alkaline electrolysis, proton exchange membrane electrolysis). However, solid oxide electrolysis is regarded as promising technology which can be applied on a

commercial scale.

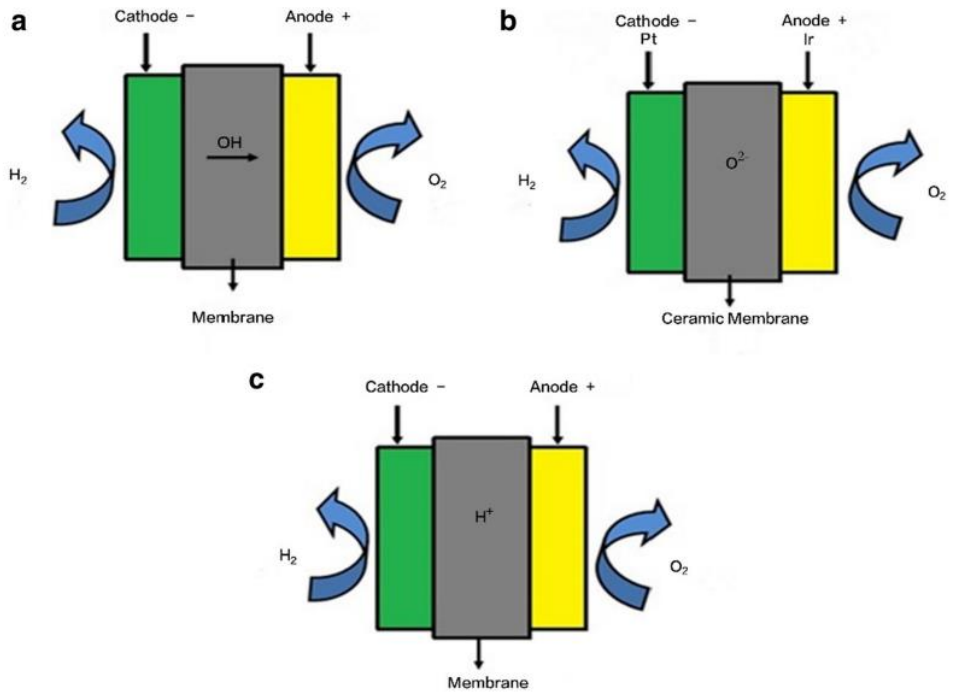


Figure 1.1. Schematic illustration of three main types of water electrolysis (a) Alkaline electrolysis cell, (b) Solid oxide cell, (c) Proton exchange membrane cell.^[6]

1.3.2 General description for electrochemical water splitting

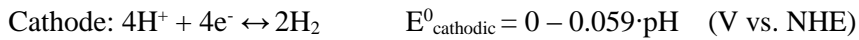
The overall electrochemical water splitting reaction is expressed as follows.



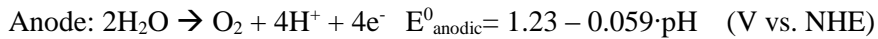
It occurs spatially separated by anode and cathode of water electrolyzer systems.

Hydrogen evolution reaction (HER) and oxygen evolution reaction (OER) proceed on the cathode and anode, respectively.

i) Hydrogen evolution reaction (HER)



ii) Oxygen evolution reaction (OER)



The water splitting reaction can thermodynamically proceed above 1.23 V vs. RHE. For realistic water electrolyzer or experiment, kinetic issue should be considered, which is due to activation energies for electrocatalysts, mass transfer limitation and conductivity in the circuit. Thus, certain amount of overpotential is virtually required for operating water electrolysis system. Total applied potential (E_{appl}) can be expressed by the following equation where η_{cathodic} and η_{anodic} are overpotentials for cathode and anode, respectively. In the Figure 2, η_{cathodic} and η_{anodic} can be calculated as $E_{\text{eq}}^{\text{c}} - E^{\text{c}}$ and $E_{\text{eq}}^{\text{a}} - E^{\text{a}}$.

$$E_{\text{appl}} = 1.23 + \eta_{\text{cathodic}} + \eta_{\text{anodic}}$$

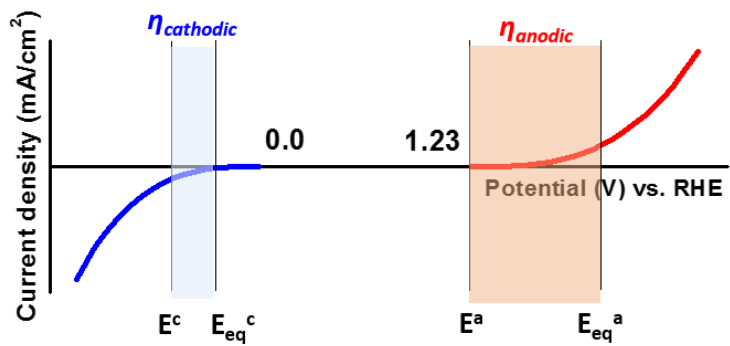


Figure 1.2. Schematic of the current to potential curve of overall water splitting reaction

1.3.3. The hydrogen evolution reaction (HER)

The cathodic half reaction of overall water electrolysis is expressed as follows.



Two protons (H^+) combine to form hydrogen molecule (H_2) by two-electron transfer reaction. Due to involving protons as reactants, thermodynamical potential is dependent on pH ($E = 0 - 0.059 \cdot \text{pH} \text{ V}$ vs. NHE). The representative reaction mechanism for hydrogen evolution reaction can be expressed as follows.



In the reaction mechanism for HER, H_{ads} indicated adsorbed hydrogen atom on the electrode surface. In the Vomer step, protons are discharged and adsorbed on the electrode surface. Then, the adsorbed hydrogen atom and protons formed hydrogen molecule (the Heyrovsky step), or two adsorbed hydrogen atoms are recombined to form hydrogen molecules (Tafel step).^[7]

The kinetic for HER can be estimated by the hydrogen adsorption free energy on the catalyst surface. When hydrogen atoms bind to the surface too strong, the desorption steps, Heyrovsky and Tafel steps, restrict the overall rate for HER. When, the hydrogen binding is too weak, the adsorption step (Volmer step) limits the rate.

Thus, intermediate binding energy between hydrogen and the electrode surface could be optimal for catalytic activity. Specifically, the volcano-shape trend is constructed by the relation between experimentally measured exchange current densities and hydrogen adsorption energies. The exchange current density is defined as the values for current density at zero overpotential. The higher exchange current density reflects that adsorption/desorption process or electron transfer proceed with lower kinetic barrier. The hydrogen adsorption energies are calculated from density functional theory (DFT), which can be explained by Sabatier's principle.

In the Figure 1.3 and 1.4, noble metals generally have optimal hydrogen adsorption energies and high exchange current densities.^[8] Platinum exhibits the best activity with negligible overpotentials in acidic condition. However, its scarcity and high cost are restriction for industrial application. Thus, earth-abundant element-based catalysts have been extensively developed for the HER. For instance, MoS₂ has been regarded as promising catalyst materials for HER, because its hydrogen adsorption energy is measured as the optimal value. However, its exchange current density is lower than noble metal-based catalysts (Figure 1.4 a). The discrepancy between volcano-plot and experimental values for MoS₂ is attributed that the volcano-shaped trend based on Sabatier's principle focused on the bond rearrangement of hydrogen atoms on the electrode surface.^[9] The discrepancy between volcano-plot and experimental values for MoS₂ is caused by various activity-controlling factors.

As previously reported, the basal plane of MoS₂ exhibits hydrogen adsorption

energy of 1.92 eV, which indicated poor catalytic performance of bulk MoS₂. However, inspired by hydrogenases in nature, the hydrogen adsorption energy at the Mo(10̄10) edge of MoS₂ was measured as 0.08 eV, near the optimal values in the volcano plots. Substantioal research efforts were devoted to the synthesis of nanostructures of MoS₂ expose the edge sits.

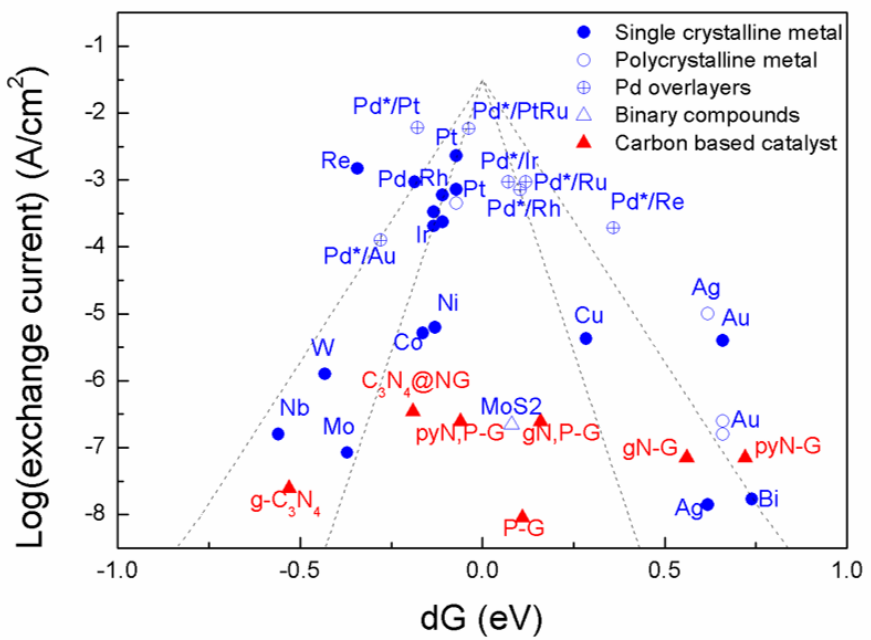


Figure 1.3. Experimentally measured exchange current, $\log(J_0)$, for hydrogen evolution over different catalyst plotted as a function of the calculated the free energy for hydrogen adsorption.^[8]

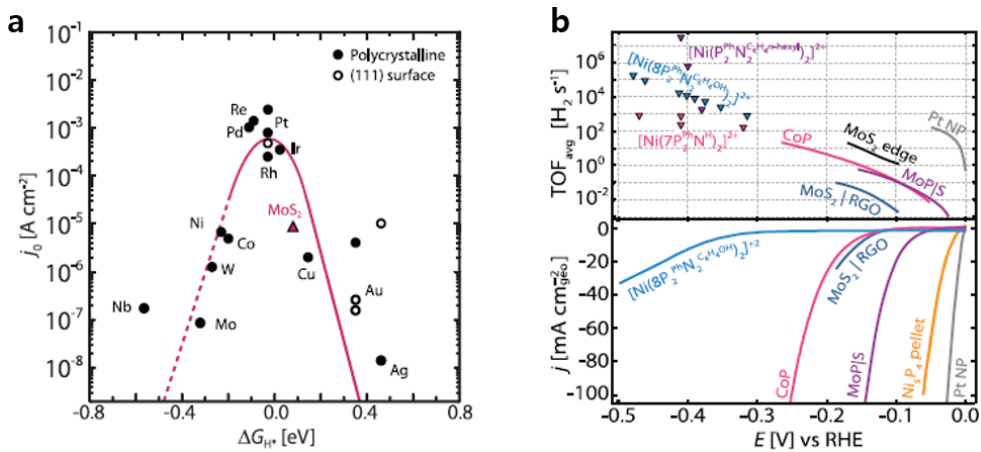
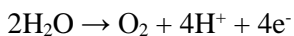


Figure 1.4. (a) HER volcano trend for metals and MoS₂ (b) TOF_{avg} plots with linear sweep voltammetry curves for previously reported HER electrocatalysts.^[9]

1.3.4. The oxygen evolution reaction (OER)

The oxygen evolution reaction (OER) proceeds as anodic half reaction for overall electrochemical water splitting reaction



The OER is regarded as major bottleneck for overall water electrolysis technique due to its slow kinetics. The slow kinetics are attributed to involvement of four electrons and four protons in multi-step processes and the high activation energy for single O-O bond formation step. In this regard, substantial efforts have been devoted to the discovery of efficient OER catalysts. Generally, precious metal-based catalysts, such IrO_x and RuO₂, have been reported for their superior activity. However, the scarcity and high price of these materials remain as critical barriers for industrial application. In this regard, earth abundant transition metal-based materials are promising materials for OER electrocatalysts.

1.4. Electrocatalysts for oxygen evolution reaction

1.4.1. The necessity for the development of OER electrocatalysts

The large overpotential for OER electrocatalysts is regarded as major bottleneck for overall water electrolysis technique due to its sluggish kinetics. The OER proceeds with complex four electron redox reaction with considerable activation energy. Highly efficient and low-cost electrocatalysts need to be developed to reduce the large overpotential of the OER in water electrolysis. Noble-metal-based compounds, such as IrO_x and RuO_2 , have been reported to be highly active OER electrocatalysts. However, their high price and scarcity are obstacles to their practical application. To solve these unavoidable difficulties, earth abundant first-row transition metal-based electrocatalysts have been actively studied to achieve good catalytic performance for decades.^{[9],[10]} Furthermore, not only activity, but also stability and selectivity are important issue for practical application.

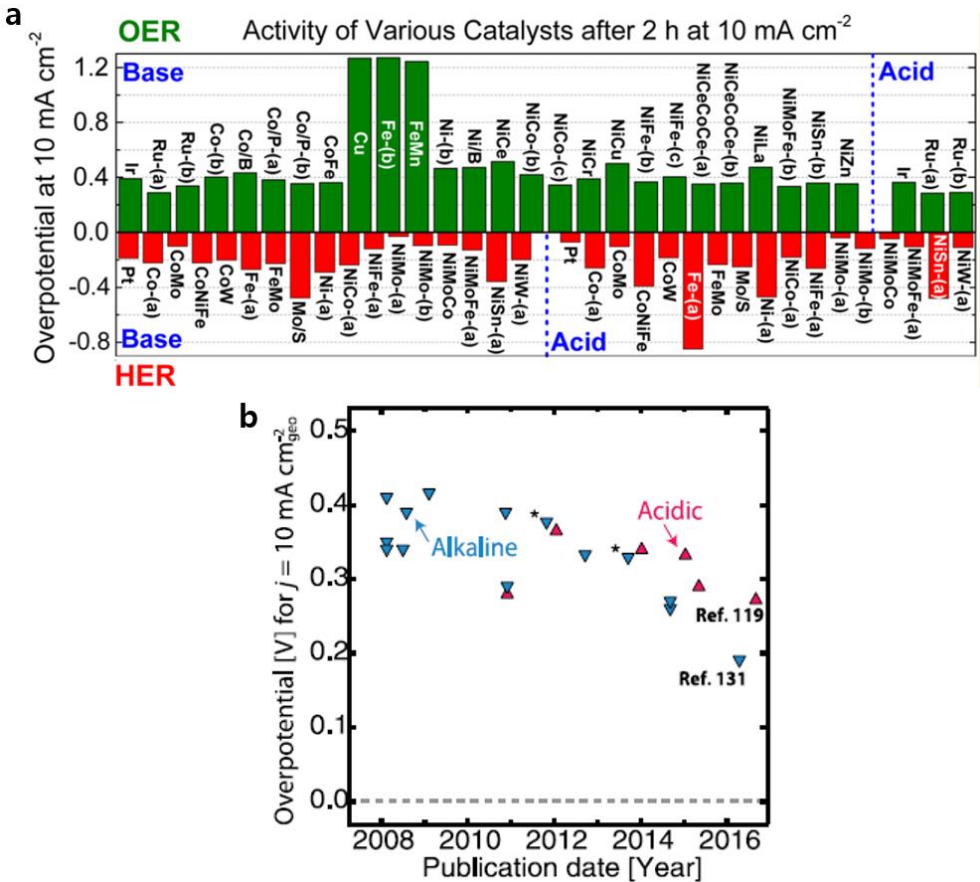


Figure 1.5. (a) Overpotential values of reported electrocatalysts for hydrogen evolution reaction and oxygen evolution reaction.^[10] (b) The chronological trend in overpotential of various OER electrocatalysts in acidic and alkaline condition^[9]

1.4.2 Design rule for OER electrocatalysts

To improve catalytic performance essentially, it is important to establish the design rule for OER electrocatalysts. The general methodologies to improve catalytic activity are increasing the number of active sites and enhancing intrinsic activity. Controlling morphology for electrocatalyst film and utilizing porous bottom electrodes such as carbon paper or nickel foam are well-known strategies to increase the number of active sites on the film-type electrocatalysts. Whereas, to improve intrinsic catalytic activity, it is crucial to understand key descriptor for OER catalysis on the active sites of the catalyst surface.

Like the hydrogen evolution reaction, volcano-type relationship have been constructed for general metal oxide surface. The adsorption energy for oxygen related species is used as key descriptors for OER activity of metal-oxide-based catalysts. Rossmeisl group discovered that universal scaling relation between adsorption energies of HOO^* vs. HO^* can be analysed the reaction free energy diagrams of representative metal oxides.^[11] It showed volcano-type trend for and the differences of adsorption energies can serve as a universal descriptor for OER activity (Figure 1.6).^[11]

Futhermore, for the case of the perovskite-type catalysts, a volcano-type trend was established between the catalytic activity and the filling of e_g orbitals in the metal cations.^[12] The filling of e_g orbital can be another descriptor for OER activity of perovskite-type catlayssts. The optimal activity was showed in the case of e_g

occupancy close to unity, which reflects that high covalency of the transition metal-oxygen bond. (Figure 1.7)^[12]

Recently, Jaramillo plotted experimental values for overpotential at 1 mA/cm² of numerous metal oxide-based electrocatalysts against the adsorption energy difference between O and OH species. These values are seen to overlay well on the theoretical values based on previous computation studies. (Figure 1.8)^[9]

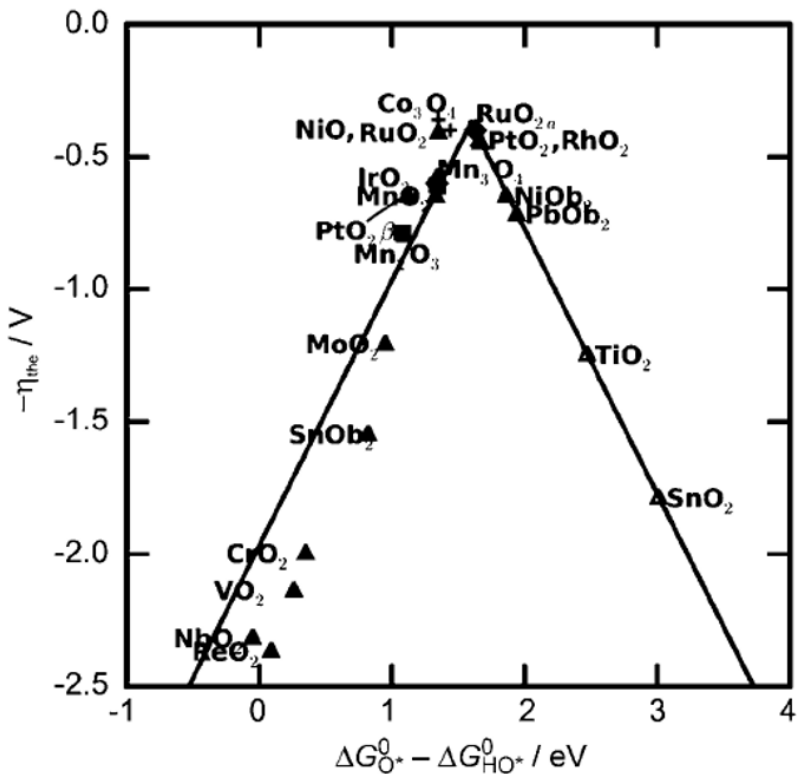


Figure 1.6. Activity trends towards oxygen evolution reaction for various oxides including rutile, anatase, Co_3O_4 , Mn_xO_y oxides.^[11]

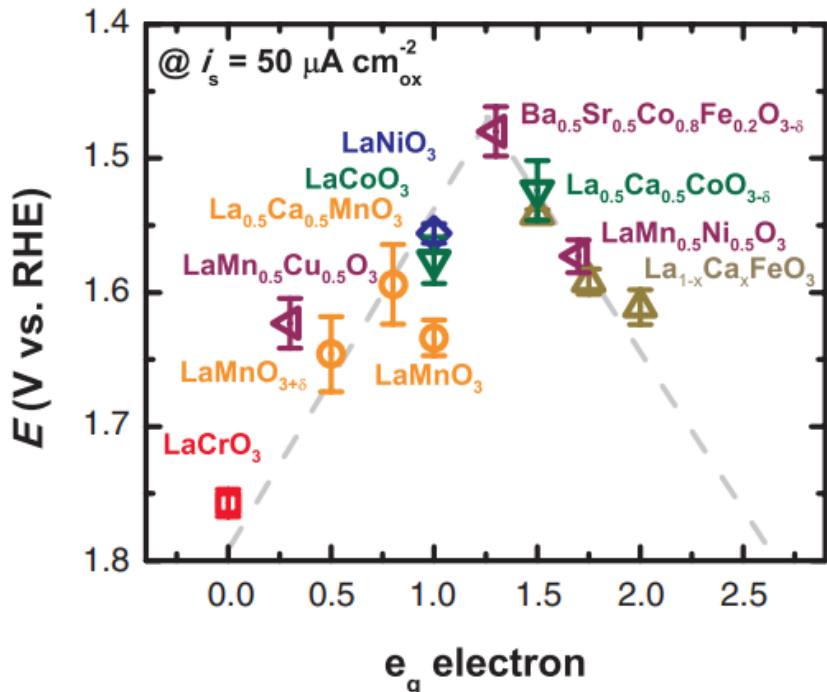


Figure 1.7. Activity trends towards oxygen evolution reaction for perovskite-type catalysts. The OER activity is defined by the overpotential at $50\mu\text{A cm}^{-2}$.^[12]

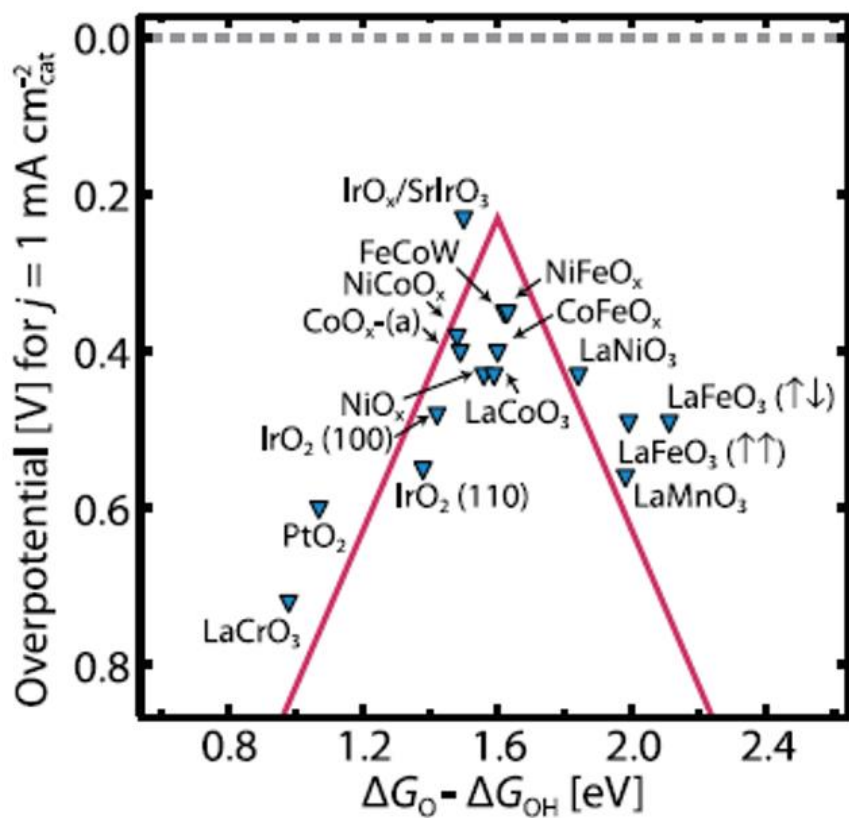


Figure 1.8. The volcano plot for experimental overpotential values of metal-oxide based electrocatalysts. The OER activity is defined by the overpotential at 1 mA cm^{-2} .^[9]

1.4.3. Reaction mechanism for electrochemical water oxidation

The water oxidation reaction is a 4-electron, 4-proton process; O-O bond formation is known to be the key chemical step that determines the rate of the whole water oxidation reaction. To develop a catalyst for the water oxidation reaction based on earth-abundant 3d transition metal oxides, many material factors were controlled such as the composition, phase, morphology and surface structure. However, the precise roles of each component and factor influencing the performance are still not clear. As a result, understanding the reaction mechanism is very important and necessary to rationally design catalysts having superior activity, stability and selectivity.

Investigation of the rate-determining step (RDS) and of the reaction intermediates is thus important to understand the reaction mechanism. Two mechanisms are proposed for O-O bond formation, which is the RDS in the water oxidation reaction. The acid (electrophilic)-base (nucleophilic) (AB) mechanism, proposed by the Shannon and Frei groups, indicates that octahedral metal-oxo sites act as mononuclear active sites.^{[13], [14]} Because these metal-oxo sites are considered to be electrophilic, a nucleophilic attack of water molecules naturally occurs to generate peroxyo intermediates. On the other hand, the radical coupling (RC) mechanism was proposed by the Voorhis groups.^[15] They predicted that the di-nuclear O-O bond formation by adjacent metal-oxo species was the energetically favorable reaction route. Here, we introduce and summarize recent studies on the reaction mechanism

for water oxidation catalyzed by 3d transition metal oxides.

i) Acid-Base mechanism

For earth-abundant metal-oxide catalysts, Shannon's group proposed a mechanism of cobalt-catalyzed water oxidation in aqueous buffering electrolytes in a pH range of 0-14. Through combined electrokinetic, cyclic voltammetry and electron paramagnetic resonance (EPR) spectroscopic studies, they concluded that Co(IV)-oxo species are crucial intermediates for O-O bond formation. Cobalt metal has mixed valency, with +3/+4 states present in the resting state; Co(IV)-oxo species were generated before RDS. Water molecules react with this Co(IV)-oxo intermediate to generate the O-O bond. The researchers excluded the possibility of a reaction with lattice oxygen atoms because no oxygen gas evolved in the absence of water.^{[16], [17]}

The AB mechanism was used to explain O-O bond formation, because the thermodynamic energy barrier for surface oxygen coupling is almost always larger than associative reaction. Mechanisms of the other 3d transition metal based catalysts are also reported. For example, Nocera's group studied the water oxidation mechanism of electrodeposited manganese oxide (MnO_x).^[18] Through electrokinetic study over a wide pH range, they suggested two competing mechanisms. A one-electron one-proton pair is removed from the surface of manganese oxide via proton coupled electron transfer (PCET), which is dominant under alkaline conditions; Mn^{3+} disproportionation mainly occurs under acidic conditions.

Indeed, the AB mechanism from high-valent metal-oxo species has been commonly suggested, especially as the water oxidation mechanism of heterogeneous 3d transition metal oxide catalysts. Recently, important reaction intermediates were characterized by Frei's group.^[13] They performed time-resolved Fourier-transform infrared (FT-IR) spectroscopy to identify stepwise cobalt intermediate structures in the catalysis. Two surface intermediates of Co₃O₄ were observed by rapid-scan FT-IR spectroscopy with ¹⁸O isotope labeling experiment. A surface superoxide intermediate and Co(IV)=O were detected for the fast catalytic site and slow catalytic site, respectively. Observation of a surface superoxide intermediate (three-electron oxidation intermediate) would be another important piece of evidence of the proposed mechanism of cobalt oxide. One structural difference between the two intermediates is the nature of the coupling among adjacent Co(III)-OH groups via oxygen bridges, which results in a huge catalytic activity difference.

ii) Radical-Coupling mechanism

The RC mechanism is also a feasible pathway to generate O-O bonds during water oxidation. In the RC mechanism, O-O bonding is constructed by coupling of two adjacent M=O species because M=O species are isoelectric structures of radical species (M-O.). Generally, based on spectroscopic evidence, the RC pathway has been proposed for O-O bond formation in molecular complex catalysts. However, it was recently reported that the generation of O-O bonding in inorganic catalysts can also be attributed to coupling of two metal-oxo species.

The Sun group reported Ru-based molecular catalysts that exhibited an unprecedentedly high turnover frequency (TOF) of $> 300 \text{ s}^{-1}$.^[19] For the molecular catalyst Ru(II)-OH₂, the resting state of the active sites was oxidized to Ru(III)-OH₂ and two consecutive oxidation processes generated a reaction intermediate, Ru(V)=O, via proton coupled electron transfer (PCET). Interestingly, the Ru(V)=O species were dimerized to Ru(IV) peroxy dimer, Ru(IV)-OO-Ru(IV), which was detected by UV-vis spectroscopy. Based on the spectroscopic data, it was concluded that the O-O bond formation had progressed by direct coupling of two Ru(V)=O species. Furthermore, the group suggested that organic ligands facilitated the radical dimerization of the Ru(V)=O active species.^[19]

The RC pathway was also proposed for the formation of OO bonds in 3d transition metal oxide catalysts. Najafpour group investigated the O-O bond formation mechanism using nano-layered MnO_x catalysts.^[20] They estimated the exchange rate of H₂¹⁸O for μ-O species (Mn-O-Mn) in MnO_x during catalysis. Spectra from diffuse reflectance infrared Fourier transform spectroscopy (DRIFTS) analysis of the μ-O species did not change during catalysis in H₂¹⁸O. These results indicate that the oxygen atoms of the μ-O species are not involved in the O-O bond formation. The group suggested that not only the AB mechanism but also the RC mechanism was feasible in the nano-layered MnO_x.^[20]

The Voorhis group theoretically investigated the water oxidizing mechanism of Co-Pi.^[15] Two adjacent Co(III)-OH species were oxidized to Co(IV) = O via a proton-coupled oxidation process. Through electrokinetic study, Nocera's group

corroborated the proton-coupled oxidation step.^[21] The free energy barrier to O-O single bond formation was computed using DFT study. Based on the computation results, direct coupling of Co(IV)=O in the cubane structure was suggested as a more favorable reaction pathway. Additionally, the free energy profile as a function of the O-O bond distance additionally supported the idea that direct coupling occurs spontaneously in cobalt catalysts.

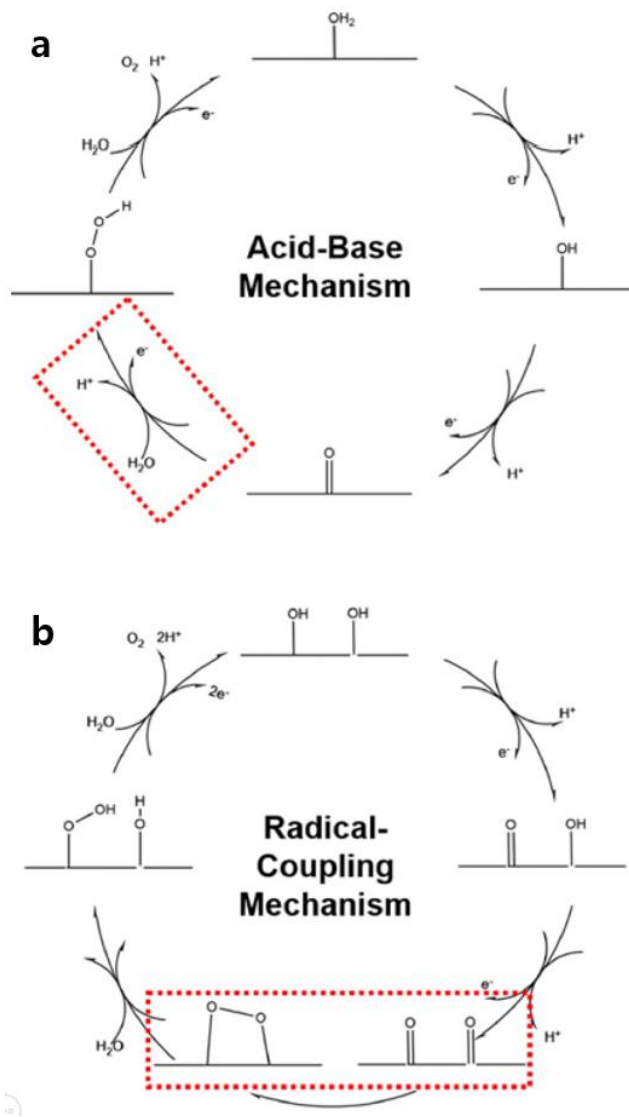


Figure 1.9. Schematic representation of water oxidation mechanism (a) Acid-Base (AB) mechanism and (b) Radical-Coupling (RC) mechanism for O-O bond formation^[22]

1.5. Lessons in biological system: Mn₄Ca cluster in Photosystem II

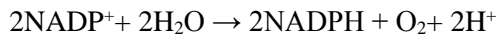
1.5.1. Introduction to photosystem process

In the photosynthesis process, carbon dioxide and water molecules are converted to glucose by the two sequential reactions, light reaction and dark reaction. The light reaction in the photosynthesis is a well-known process for light-to-electron energy conversion systems. Photosynthetic system generally captures the light with an efficiency of ~30% in nature.

Light reaction enables to progress oxygenic photosynthesis and interactions between photosynthetic proteins in the living organism. The photosynthetic proteins involved in light reaction are located in the thylakoid membrane of chloroplasts. Also, they are participated in various electrochemical reactions with a specific direction. The flexible membrane platform serves as key strategy for the reactive proteins to be aligned in a specific direction.

The protein complexes in the thylakoid membrane play central role as the important functional photosynthetic proteins for light-to-electron energy conversion. The light reaction induces the stepwise electron excitations for both photosystem I (PS I) and II (PS II). The overall electron transfer pathway for photosynthesis is called the Z-scheme. In the Z-scheme, electrons are moved through the inner lipid layer of the thylakoid membrane. In the PS II, the electron transfer is initiated by the water oxidation via the Mn₄Ca clusters. The Mn₄Ca cluster showed the outstanding efficiency for water oxidation. The electrons, generated during water oxidation,

excite reaction center of PS II (P680^{*}), and immediately drop down to PS I (P700) using various mediators, quinones and cytochromes. Then, electrons are excited to the final excited state (P700^{*}) in the PS I and consumed by the reduction reaction from NADP⁺ to NADPH by the following chemical reaction.



In the Z-scheme process, protons also flow with electron movements. Water oxidation in the Mn₄Ca cluster serves as an electron source, and generates protons. In detail, plastoquinone delivers protons with electron transfer during the redox reactions. During this process, protons are transported through the exterior thylakoid membrane into the stroma, thereby inducing a proton gradient across the membrane. Protons are accumulated in the stroma and consumed for ATP synthesis. The electron flow produced proton transfer, NADPH and ATP, which are directly utilized as reductants in the dark reaction

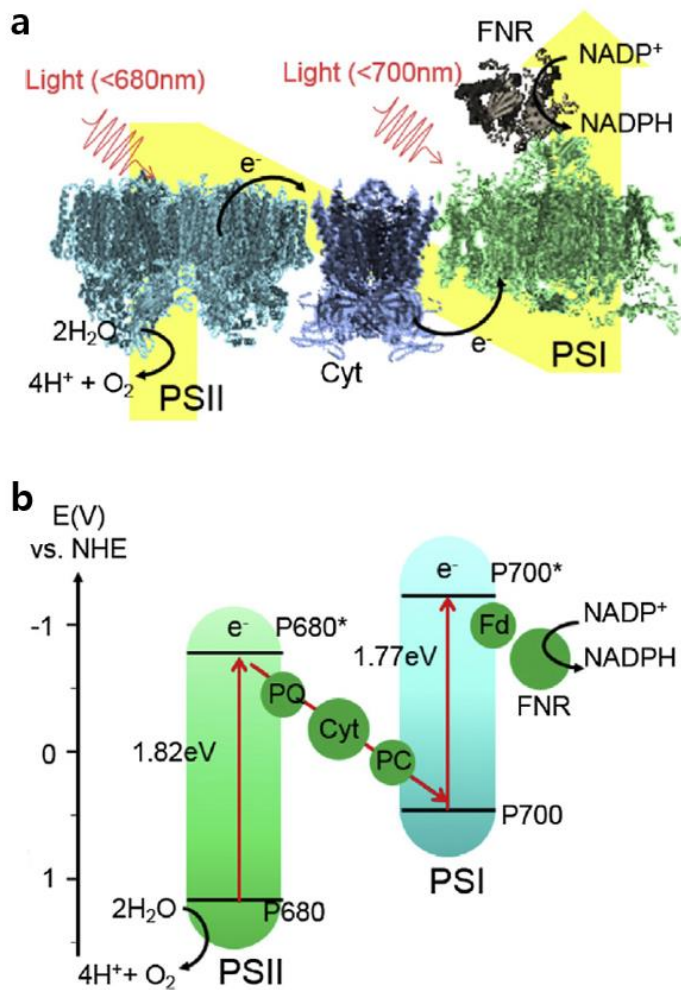
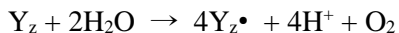


Figure 1.10. Schematic representation of Photosynthetic process in photosystem. (a) Scheme of Z-schematic electron flow in light reaction (b) energy diagram of Z-schematic electron flow^[23]

1.5.2. Water oxidizing catalysis for Mn₄Ca cluster

Water oxidation by the WOC of PS II involves a redox-active tyrosine residue (Tyr161, Y_z), which is oxidized by light absorption from the P680 reaction center.^[24]

The net reaction equation for the oxygen evolving reaction is as follows:



The four electrons generated during water oxidation are transferred from the Mn cluster to Y_z and are accompanied by four deprotonation reactions in the thylakoid lumen.^[25] In 1970, the Kok group suggested that a linear four step mechanism of natural water oxidation, which has been termed the Kok cycle, is comprised of five intermediate S_i states, where subscript i denotes the number of oxidizing equivalents stored for oxygen evolution and ranges from 0 to 4.^[26] After four oxidizing equivalents are accumulated, the S₄ state releases a dioxygen molecule and spontaneously decays to the most reduced S₀ state. Under dark conditions, the S₀ state is gradually oxidized to the dark stable S₁ state.

To realize the efficiency of natural WOC in a synthetic system, it is critical to understand the structural changes that occur in the active site of the Mn₄Ca cluster during catalysis. In the following sections, recently acquired information for each S_i state is summarized, with particular focus on electronic/geometric structure analyses.

1.5.3. Structural characteristic for Mn₄Ca cluster

The dark-stable S₁ state provides a profitable starting point for structural analysis by X-ray crystallographic methods. Although the crystallization of the Mn₄Ca cluster in the S₁ state has been well studied since 2001, structural information on the S₁ state could not be obtained due to the resolution limits of available analytical instruments.^[27] Not until 2011 did the Umena group succeed in resolving the detailed atomic structure of the S₁ state using an X-ray diffraction technique at a resolution of 1.9 Å.^[28] At this resolution, the structure of the Mn cluster can be clearly determined because the electron density of each atom in the cluster is distinct. Using this approach, the Mn cluster was found to have a distorted cubane structure consisting of three distinct Mn atoms and one Ca atom with oxo-bridges, with a fourth dangling Mn atom. In addition, four water ligands are bound to the Ca atom and dangling Mn atom, and the surrounding environment of the Mn cluster was also identified. Notably, O5 has a relatively long Mn-O distance and therefore weaker bonding strength compared to the other bonds in the cluster, suggesting that O5 has high mobility than other oxygen atoms in the cluster and thus plays an important role in natural water oxidation.

After the crystal structure of the Mn cluster was obtained at 1.9 Å resolution by XRD analysis, the position of the O5 atom has been debated. Although the XRD results suggested that O5 is positioned at the midpoint of Mn1 and Mn4, EXAFS analysis and DFT calculations indicated that the O5 atom is closer to Mn4 than

Mn1.^{[29], [30]} This discrepancy likely resulted from X-ray radiation damage to the Mn cluster, which caused the partial reduction of Mn, elongation of the atomic distance, and ultimately, destruction of the Mn cluster. At 1.9 Å resolution in the XRD analysis, approximately 25% of Mn atoms were reduced and the S₁ state could also be reduced to the S₀ state and even the pre-S₀ states like S₋₁, S₋₂, and S₋₃ states. In 2015, the Suga group resolved the ‘radiation-damage-free’ S₁ structure of the Mn cluster at 1.95 Å resolution using a femtosecond X-ray free electron laser (XFEL) technique, which permitted the collection of diffraction patterns before the occurrence of radiation damage.^[31] In contrast to the previous XRD-based structural determination, the XFEL position of O5 was found to be closer to Mn4 than Mn1, a finding that is well matched with the results of previous EXAFS and DFT analyses.

The S₂ state, which is the one-electron oxidized state from S₁, has been investigated using electron paramagnetic resonance (EPR), EXAFS, and DFT analyses.^[32] Two distinctive species with a multiline EPR signal at $g = 2$ at room temperature and a multiline EPR signal at $g \geq 4.1$ have been detected under lower temperature conditions. Furthermore, the two EPR signals reversibly interconvert when the temperature or illumination condition is altered, indicating that the S₂ state has two interconvertible spin states with total spin numbers of $S = 1/2$ for the multiline EPR signal at $g = 2$ and $S = 5/2$ for the EPR signal at $g \geq 4.1$. The structural uniqueness of the S₂ state was also confirmed from the results of EXAFS studies and DFT calculations. These analyses revealed that as Mn4(III) is oxidized to Mn4(IV) under light illumination, an open cubane structure with $S = 1/2$ is constructed as O5 moves

toward the Mn4 site. In contrast, when Mn1(III) is oxi-dized to Mn1(IV), a closed cubane structure with $S = 5/2$ is expected as O5 moves toward Mn1. This unique interconvertibility of the S₂ state complicates understanding of the Kok cycle.

The kinetic state of the Kok cycle is dramatically varied by the S₂ state that participates in the S₂-S₃ transition, in which a water molecule is additionally inserted. Two representative researches examined the S₂-S₃ transition mechanism: a quantum mechanics/molecular mechanics (QM/MM) study by the Guidoni group and a DFT-study by the Siegbahn group.^[32] The Guidoni group revealed that the closed cubane structure participates in the S₂-S₃ transition and that W3 bound to the Ca atom shifts to occupy the uncoordinated site of Mn4 following the oxidation of Mn(III) to Mn(IV). Contrastly, the Siegbahn group reported that the open cubane S2 structure is involved in the S₂-S₃ transition and that a new water molecule outside of the Mn cluster enters the empty coordination site of Mn1 following the oxidation Mn1(III) to Mn1(IV). As it remains unclear which S₂ structure is formed prior to transition to next state, the subsequent O-O bond formation and structure of the S₃ and S₄ states remain controversial. Nevertheless, the S₃ state was recently shown by EPR to be comprised of six-coordinated Mn(IV) with a total spin number of $S = 3$.^[33]

1.5.4. Electronic structure change during catalysis

Generally, electronic structure is closely related with the spinstate of metal components originating from intermagnetic coupling. Resolution of the electronic structure in the Mn₄Ca cluster, specifically the Mn valency change in the Kok cycle, is therefore complicated. To this end, EPR spectroscopy has been adopted to investigate the spin state of the Mn₄Ca cluster. In terms of total spin number, the S_i states can be classified into either “resting-like states” (S₀, S₁, and open cubane S₂), which have low total spin numbers, or “active-like states” (closed cubane S₂, S₃, and S₄), which have high total spin numbers. The properties of these states indicate that a strong correlation exists between catalytic reactivity and the spin state of the Mn cluster.^[34]

In a pioneering study, the Pantazis group examined the electronic structure of the Mn₄Ca cluster by performing EPR analysis and DFT calculations. The analyses indicated that a closed structure in the active-like states would adopt a high spin state because the ferromagnetic coupling of metal-oxo-metal bonding is normally preferred when the bonding angle approaches 90°.^[34] Thus, it is expected that the active-like states of the Mn₄Ca cluster, which are associated with water insertion and O-O bond formation, favor high spin states. These findings suggested that the interconvertible S₂ state, which is necessary for the dramatic change from the low spin to high spin state, is involved in the formation of the closed cubane structure. Additional substrate substitution experiments using ammonia and methanol

supported this hypothesis and implied the existence of a water-insertion pathway that includes Mn4 and the Asp61 residue.^[35] Based on these findings, the Pantazis group proposed a new S₂-S₃ transition model with the following features: i) deprotonation of W1, ii) hydrogen bond formation between W2 and O5, iii) nucleophilic attack of another water molecule to Mn4, and iv) successive rearrangement of the atomic structure.^[34] Regarding the S₃ state, two possible intermediates with a total spin number of S = 6 and 3 were suggested based on DFT calculations.^[34]

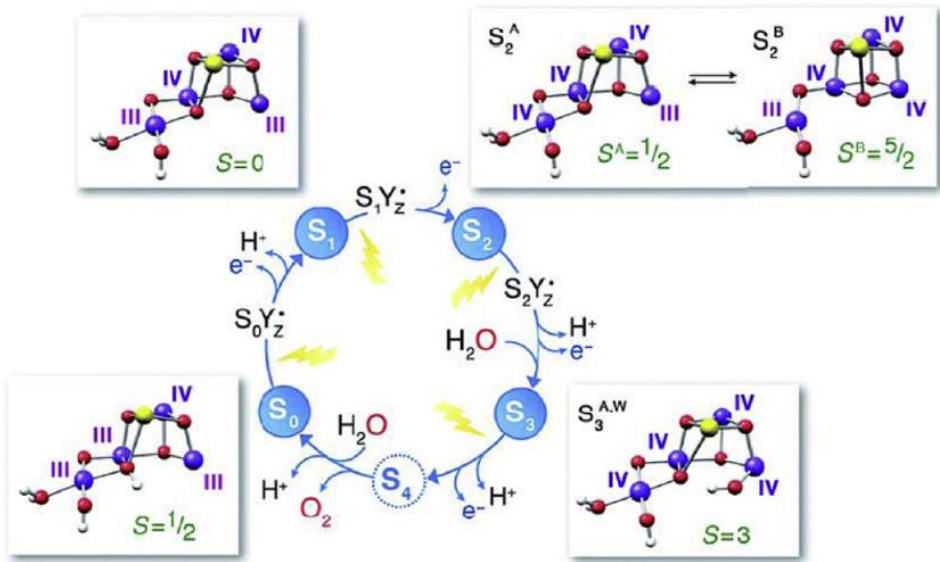


Figure 1.11. The Kok cycle with spectroscopically consistent structures of the Mn cluster and their spin states.^[29]

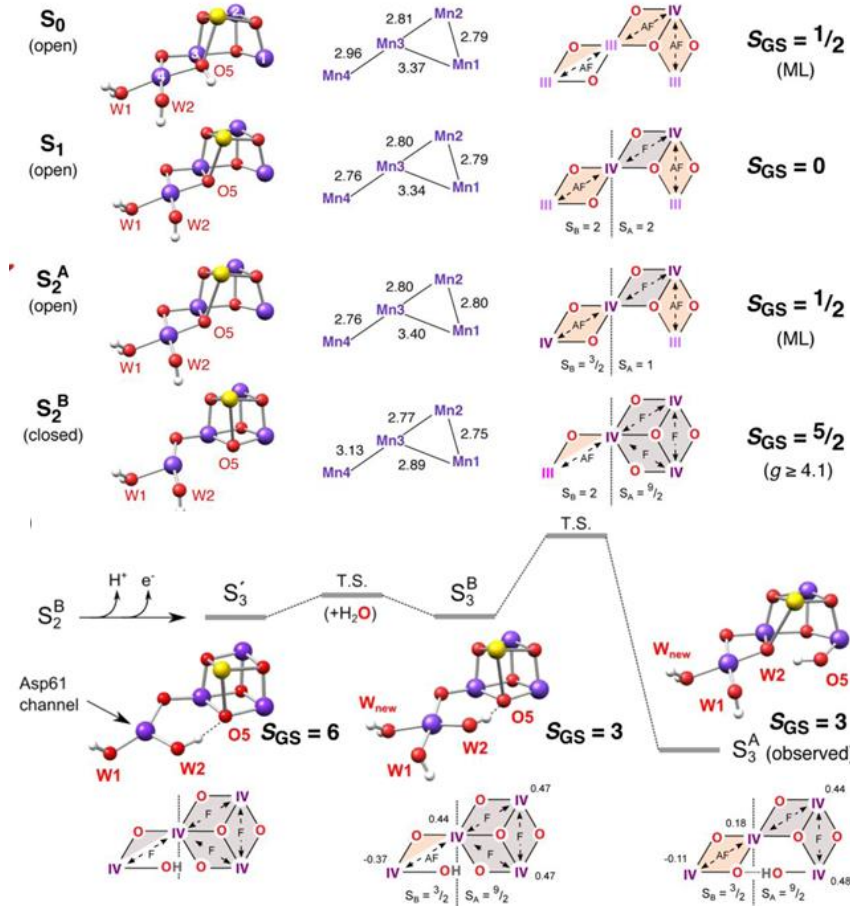


Figure 1.12. Structural model for all S_i states of the Mn cluster: atomic structure of the Mn cluster, Mn-Mn distances(Å) of optimized geometries, the nature of magnetic couplings(AF for antiferromagnetic coupling and F for ferromagnetic coupling), and total spin numbers respectively. (c) Proposed S_3 intermediate states upon S_2 - S_3 transition. The loss of the Asp61/W1 hydrogen bond with subsequent low-barrier water insertion *via* the Asp61 channel and rearrangement is involved.^[34]

1.6. Artificial Mn-based electrocatalysts for water oxidation

Manganese is promising element for developing OER electrocatalysts due to its abundance in nature. Mn is the third most abundant transition metal element in the Earth's crust. Also, Mn exists in a variety of oxidation state from Mn(II) to Mn(VII), which is related to redox-active characteristic during catalysis. Furthermore, inspired by Mn₄Ca clusters in photosystem II, manganese oxide can be promising materials for developing water oxidizing electrocatalysts.

Manganese oxides exhibits diverse Mn-O moieties with more than 30 crystalline structure phases. MnO, Mn₃O₄, Mn₂O₃, Mn₅O₈ and MnO₂ are the stoichiometric chemical formulas for manganese oxides with various Mn valency from Mn(II) to Mn(IV). Additionally, MnO₂ has various polymorphs in which the basic building unit is the MnO₆ octahedron, and each MnO₆ octahedron is connected to others in a cornerand or edge-sharing manner. From their different connections, MnO₂ polymorphs can be divided into three categories: tunnel structures surrounded by a one-dimensional MnO₆ octahedra chain (e.g. α -, β -, γ -, and R-MnO₂), layered structures of laminated two-dimensional sheets of MnO₆ octahedra (e.g. δ -MnO₂), and three-dimensional structures (e.g., λ -MnO₂).

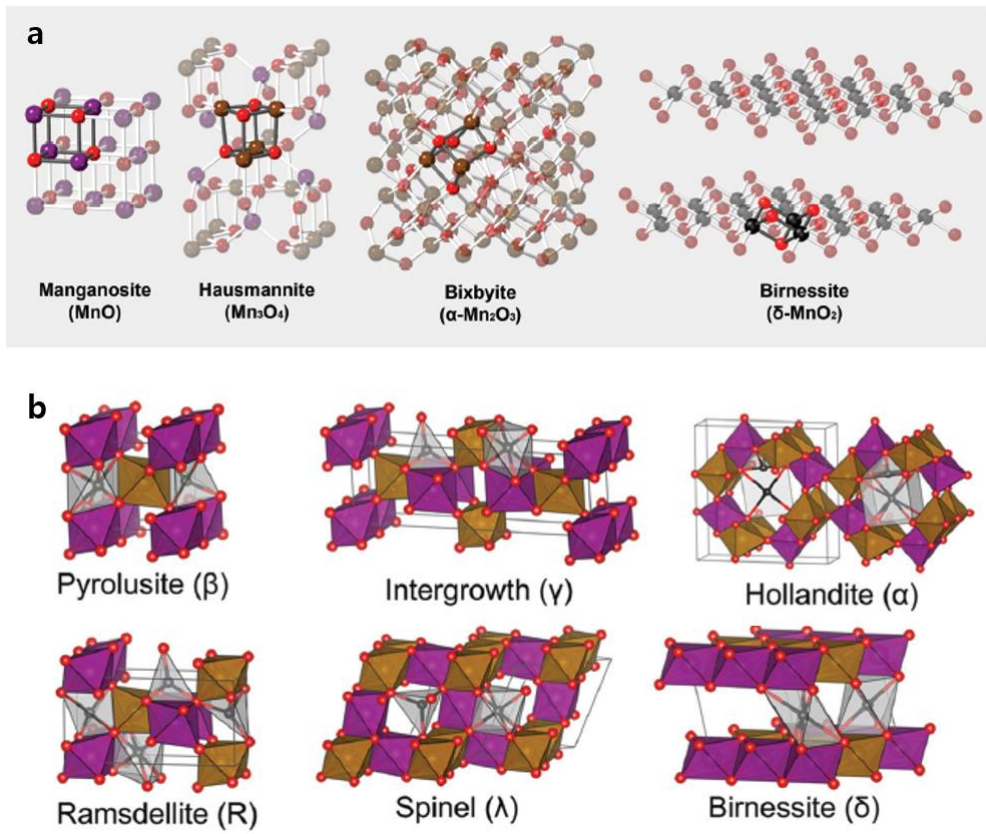


Figure 1.13. (a) Crystal structure of the various manganese oxides, MnO, Mn₃O₄, Mn₂O₃ and MnO₂^[36] (b) Crystal tstructure of various MnO₂ plomorphs.^[37]

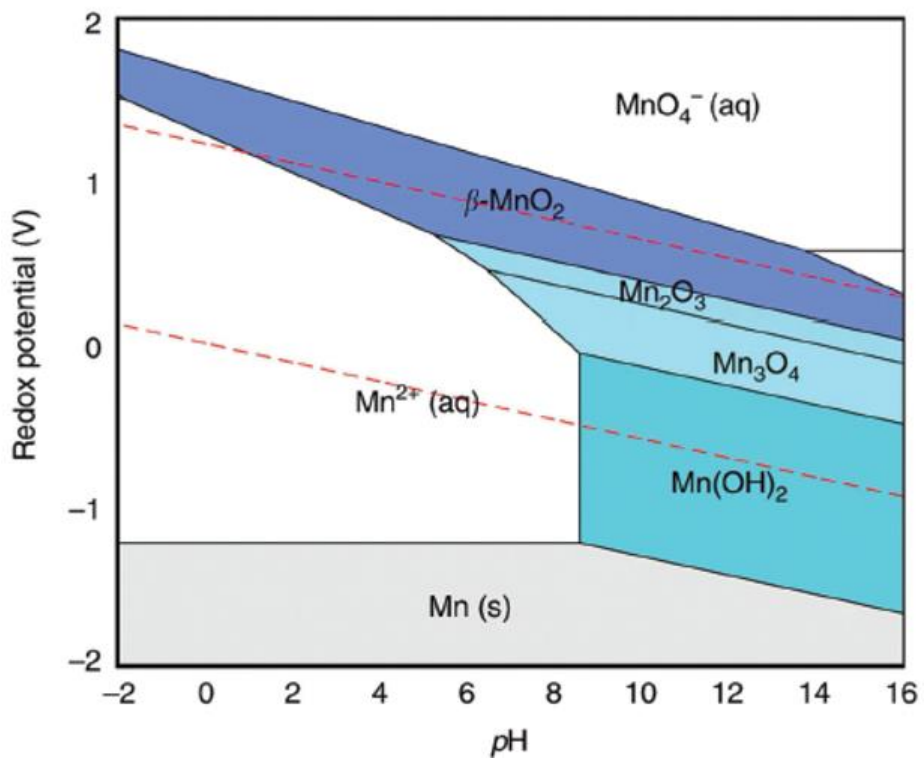


Figure 1.14. Calculated Pourbaix diagram of Mn-O-H phases^[38]

1.6.1. Mn-based electrocatalysts with crystalline structure

To clearly examine the active structural motif, various crystalline manganese oxides were also synthesized and compared as a model system. For instance, Suib's group synthesized manganese oxides with various structures (α -, β -, δ - MnO_2 , and amorphous manganese oxides) and systematically studied their manganese oxides to identify the origin of OER activity under alkaline conditions.^[39] Importantly, the measured electrocatalytic activities depended on the crystallographic structures in basic media and exhibited the following order: $\alpha\text{-MnO}_2 >$ amorphous manganese oxides $> \beta\text{-MnO}_2 > \delta\text{-MnO}_2$. The $\alpha\text{-MnO}_2$, with a well-ordered pore structure and mixed valence state (Mn(III) and Mn(IV)), showed better activity (490 mV overpotential at 10 mA/cm², 0.1 M KOH) than that of amorphous manganese oxides. They suggested that the higher activity of $\alpha\text{-MnO}_2$ was caused by the mixed Mn valency (average oxidation state: 3.7) and the well-ordered tunnel structure and abundant di- μ -O(H) bridges, which served as protonation sites. These reflect that the pore structure could be a crucial factor for the catalytic activity because ion transport becomes more important at higher current density.

Furthermore, they synthesized mesoporous Mn_2O_3 to investigate the effect of Mn(III) species for the catalytic activity.^[40] They made the catalysts through a sol-gel process involving a nonionic surfactant and calcination. As the calcination temperature increased, the amount of Mn(III) species (Mn_2O_3 crystal phase) in the manganese oxide also increased. The samples with a larger amount of Mn(III)

species, which were annealed at higher temperatures, show higher electrocatalytic activity for the water oxidation reaction. The best performing catalyst has a $150\text{ m}^2\text{ g}^{-1}$ specific surface area consisting of a nanocrystalline Mn_2O_3 crystal and showed a 507 mV overpotential for 10 mA/cm^2 in 0.1 M KOH electrolyte. Therefore, they suggested that manganese oxides containing rich Mn(III) species and possessing high surface area would be an important design guideline for highly active manganese oxide electrocatalysts for the water oxidation reaction under alkaline conditions.

Additionally, Dismukes' group studied the geometrical effects of $\text{Mn(III)}\text{O}_6$ octahedra on the electrocatalytic water oxidizing activity by comparing binary manganese oxides with various phases.^[41] Crystalline manganese oxides containing Mn(III) ($\gamma\text{-MnOOH}$ and Mn_2O_3), Mn(IV) ($\beta\text{-MnO}_2$ and $\delta\text{-MnO}_2$), and mixed-valence manganese oxide (Mn_3O_4) were analyzed. While pure $\beta\text{-MnO}_2$ exhibited poor catalytic activity, $\gamma\text{-MnOOH}$ (tetragonally distorted $\text{Mn(III)}\text{O}_6$ with D_{4h} symmetry) showed moderate activity, and Mn_2O_3 (trigonal antiprismatic $\text{Mn(III)}\text{O}_6$ with D_{3d} symmetry) had high activity for the electrocatalytic water oxidation. The HexBir, The hexagonal polymorph of $\delta\text{-MnO}_2$ with containing few out-of-layer corner-sharing $\text{Mn(III)}\text{O}_6$, showed catalytic activity over ten times higher than that of TriBir, the triclinic polymorph of $\delta\text{-MnO}_2$ containing in-plane edge-sharing $\text{Mn(III)}\text{O}_6$. They further understood the importance of the corner-sharing Mn(III) content in $\delta\text{-MnO}_2$, instead of the total content of Mn(III), through correlation with the high catalytic activity of $\gamma\text{-MnOOH}$. Corner-sharing $\text{Mn(III)}\text{O}_6$ on the catalyst surface could

activate Mn(III) species by interconverting nearby Mn(II) and MnO₂ to form γ -MnOOH. Also, the similarity between the corner-sharing Mn(III) species in synthetic catalysts and dangling Mn(III) of the biological WOC was explored. In the overall catalytic cycle for the WOC, the Mn(III) species only includes Mn-bound water and this unique ligand environment was predicted to favor Mn(III) and Mn(V) species instead of Mn(IV) species. In other words, oxidation is centered on the oxido ligands rather than Mn in the catalytic cycle. They suggested that the similar active site and electronic structure to those of the WOC are the origins of the high catalytic efficiency of these two synthetic manganese oxide catalysts.^[41]

The geometry of Mn(III) octahedra was researched by comparing γ -MnOOH and Mn₂O₃, which include only Mn(III) species. The γ -MnOOH contains only the Mn(III)O₆-type structure of Mn(III) in its unit structural motif, which is the tetragonally elongated (D_{4h}-type) octahedron influenced by Jahn–Teller distortion. This distortion is contributed to four short and two long Mn–O bonds per D_{4h}-type octahedron, and individual D_{4h} units are linked to three other Mn(III)O₆ octahedra by corner-sharing bridges, which are located above a rhombohedral vacancy. In contrast, Mn₂O₃ contains five symmetry-inequivalent Mn(III)O₆ sites in its unit cell. In three of the five sites, all Mn–O bond lengths are different because of the distortion of the D_{4h} symmetry with two long and four shorter bonds. In the other two sites, all bond lengths are very similar, which indicates trigonal antiprismatic D_{3d} symmetry. The sites are connected to two or three other Mn(III)O₆ by corner-sharing bridges, and thus these sites can be compared with the typical γ -MnOOH. The surface of

Mn(III)O₆ lies above a three-fold axis and maintains the D_{3d} symmetry formed by the three oxo bridges, resulting in an e¹_g electronic configuration. Because the trigonal ligand field of the fixed oxo bridges restrains the tetragonal Jahn–Teller distortion, the lengths of Mn–O bonds are anticipated to be nearly equivalent. The three surface waterbinding oxo sites are expected to be relatively flexible, which could be beneficial for catalytic activity if O₂ release from this site is rate-limiting.

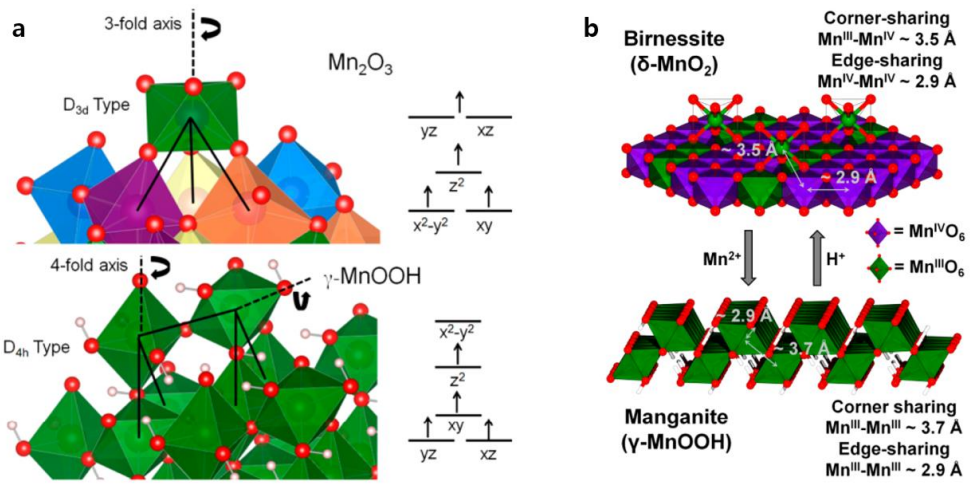


Figure 1.15. (a) Demonstration of the crystal structure and d-orbital electronic configuration of Mn_2O_3 and $\gamma\text{-MnOOH}$ (b) Description of corner-shared Mn(III) octahedral in $\delta\text{-MnO}_2$. Structural rearrangement forms active species (corner-sharing Mn(III) octahedra) on the surface of $\delta\text{-MnO}_2$.^[41]

1.6.2. Mn-based electrocatalysts with disordered structure

Disordering the crystal structure of manganese oxides has been regarded as one of the effective strategies to improve the electrocatalytic water oxidation activity. Interestingly, several reported amorphous catalysts with high catalytic activity under neutral condition possessed a common structure consisting of layers of edge-sharing Mn(IV)O_6 octahedra with Mn(III) species. The Dau and Zaharieva group synthesized an amorphous manganese oxide catalyst by the potential cycling treatment of electrodeposited $\delta\text{-MnO}_2$.^[42] This catalyst showed high electrocatalytic activity even at neutral condition. Almost no catalytic current was observed from a regular $\delta\text{-MnO}_2$ sample above 1.4 V vs. NHE in neutral phosphate buffer. In contrast, the active amorphous sample exhibited a clear anodic current from the water oxidation reaction, 1 mA/cm² at an overpotential of 590 mV. Thus, the cubane-like structural motif of $\delta\text{-MnO}_2$ with di- μ -oxo bridged Mn ions could not correlate to the electrochemical water oxidation activity under neutral pH. The average oxidation states of active and inactive samples were elucidated from XANES analysis. Interestingly, the active sample showed a lower oxidation state (3.8) than that of the inactive sample (4.0) with regular $\delta\text{-MnO}_2$ structure. EXAFS analysis indicated that the structure of the active sample consisted of comparable proportions of di- μ -oxo bridged Mn ions and mono- μ -oxo bridged Mn ions, cornersharing MnO_6 octahedra with an Mn–Mn distance of about 3.4 Å. They also supported that the abundant (de)protonatable $\mu_2\text{-O(H)}$ groups and terminal water molecules coordination sites in

the disordered structure contributed to its OER activity. As a result, the mixed valence of Mn(III) and Mn(IV) with a large number of mono-m-oxo bridged structures and plenty of proton exchange sites was suggested as a crucial characteristic for the high catalytic activity of amorphous manganese oxides under neutral conditions.

Similar atomic-level structural characteristics were suggested by comparing two different nanostructured Mn oxide catalysts that were synthesized by chemical symproportionation (s-MnO_x) and impregnation (i-MnO_x) methodologies.^[43] The i-MnO_x showed higher catalytic activity (lower Tafel slope) and smaller electrochemical active surface area under pH 7.0 than was the case for s-MnO_x, which possessed a similar structure to that of regular δ-MnO₂. For both catalysts, the average oxidation states increased from 3 (i-MnO_x) and 3.5 (s-MnO_x) to 4 after catalysis. The crystal structure of i-MnO_x contained a mixture of β-MnO₂ and γ-MnO₂ phases, which also contained dangling out-of-layer Mn ions linked via mono-m-oxo bridges (corner-sharing MnO_x octahedra with coordinatively unsaturated sites). In addition, the defective structure implied that the electrode contained a high number of Mn vacancy sites, which prevented the formation of di-μ₃-oxo moieties and resulted in more di-μ₂-O(H) bridges between Mn ions as well as terminal water coordination sites. Thus, they suggested that the coordinatively unsaturated out-of-layer Mn species might behave as an adsorption site and nearby (de)protonatable sites facilitated the water oxidation reaction. Additionally, Driess, Dau, and co-workers prepared amorphous MnO_x containing mixed valence states by oxidizing

inactive MnO nanoparticles with a chemical oxidant. The prepared amorphous MnO_x showed high catalytic activity towards photochemical as well as electrochemical water oxidation under neutral conditions.^[44] The structure model derived from EXAFS analysis showed that the sample contained layers of di- μ -oxo bridged Mn⁴⁺ ions, similar to those of the δ -MnO₂ parent structure, along with Mn(II)/Mn(III) species occupying the interlayer oxide space. These findings indicate that a structure consisting of out-of-layer Mn(II)/Mn(III) species with layered δ -MnO₂ would be an important structural feature for the enhanced electrocatalytic activity of amorphous MnO_x.

Nocera group performed extensive studies on a disordered δ -MnO₂ catalyst system.^{[45], [46]} They first elucidated the optimum electrodeposition conditions to enhance the catalytic activity of disordered δ -MnO₂ and then performed detailed spectroscopic studies on disordered δ -MnO₂.^[46] The catalytic activity of the δ -MnO₂ electrode was dramatically enhanced after potential cycling. The Tafel slope decreased from 120 to 70 mV/dec under neutral conditions and 650 to 90 mV/dec under acidic conditions. They found that the catalytic activity enhancement began with a structural phase transformation through the charge comproportionation of the original δ -MnO₂ film with cathodically generated Mn(OH)₂ to produce a Mn₃O₄-like intermediate structure (δ -Mn(IV)O₂ + 2Mn(II)(OH)₂ → Mn₃O₄ + 2H₂O). A consecutive anodic potential further oxidized the Mn₃O₄-like intermediate structure to disordered δ -MnO₂. Chemically introduced Mn(III) species in disordered δ -MnO₂ contributed to the enhanced catalytic activity without charge disproportionation.

Furthermore, *in situ* XAS analyses showed that the Mn(III) species still existed during the water oxidation catalysis with a lower coordination number. The decrease of the Mn–O coordination number to four and the relatively constant bond length suggested that the Mn(III) species might be coordinated with a tetrahedral ligand field. The tetrahedral ligand field of the Mn(III) species constricted further oxidation and the valence state was trapped at 3 at a high anodic applied potential. The researchers suggested a unique structural motif of Mn(III) intermediate species consisting of tetrahedral Mn(III) species located next to the Mn(IV) O_6 octahedra in disordered δ -MnO₂. An electronic structure calculation of this unique local coordination structure motif indicated the reconstruction of Mn d and O 2p states in a manner that facilitated oxygen hole formation. That is, trapped Mn(III) species in the tetrahedral ligand field induced local strain and distorted nearby Mn–O coordination bonds, resulting in a narrower gap between the highest occupied and lowest unoccupied molecular orbitals and an oxygen-based highest occupied molecular orbital. As a result, they indicated this unique local structure in disordered MnO₂ enabled the facile generation of highly reactive Mn-oxy radical species, resulting in the enhanced electrochemical OER activity.

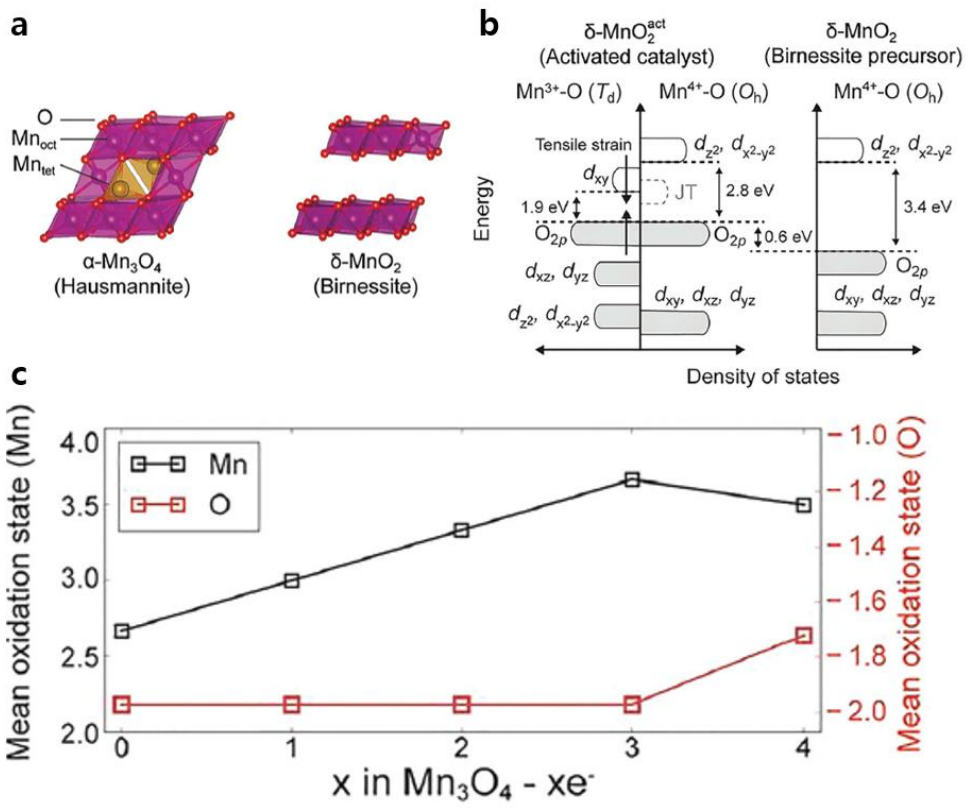


Figure 1.16. Calculated electronic structure of disordered $\delta\text{-MnO}_2$. (a) Crystal structures of Mn_3O_4 and $\delta\text{-MnO}_2$. (b) Band structure of the activated disordered $\delta\text{-MnO}_2$ and $\delta\text{-MnO}_2$. (d) Calculated average valence state of Mn and O.^[46]

1.6.3. Key factors for OER activity in Mn based electrocatalysts

Despite the development of several promising Mn-based catalytic materials, severe activity discrepancies exist between synthetic catalysts and the WOC under neutral conditions. Synthetic Mn catalysts typically require an overpotential of 500–700 mV for the OER to proceed at neutral pH. To overcome these issues, a better understanding of the mechanisms underlying the activity of Mn-based catalysts for the OER is required.

Manganese based electrocatalysts have inherent hindrance for water oxidation under neutral condition. This undesired phenomena has relevance with Mn redox process during catalysis. As shown in Figure 1.17, when Mn^{3+} species which adopt $t_{2g}^3 e_g^1 d$ orbital configuration is generated under catalytic reaction, there exist two possible reaction pathways; i) J-T distortion and ii) Charge disproportionation.^{[47], [48]} In case of conventional Mn oxide compounds, unfortunately, rigid and highly symmetric MnO_6 octahedrons hamper Jahn-Teller (J-T) distortion of Mn enters. Instead, charge disproportionation reaction, which makes Mn^{3+} split into Mn^{2+} and Mn^{4+} is proceeded. The suppressed redox kinetics sequentially leads to inferior catalytic performance. Theoretically, instability of Mn^{3+} intermediates in conventional manganese oxide were demonstrated via computation analysis. Figure 4 displays pair distribution function of MnO_2 , and MnO compounds when manganese atoms were intentionally oxidized to Mn^{3+} state. As expected, J-T distortion is barely observed in reduced MnO_2 case. Moreover, although J-T

distortion is proceeded to some extent in oxidized MnO structure, high inner pressure makes Mn(III) in MnO unstable. In addition, in case of Mn³⁺ containing Mn oxide compounds, such as Mn₂O₃, it was verified that facile valency change is difficult to occur due to the high reorganizational energy associated with Mn³⁺ oxidation. The Nocera group interrogated mechanism for electrodeposited manganese oxide (MnO_x) through electrokinetic analysis.^[18] Combined Tafel analysis and proton dependence in the electrokinetic rate law, two competing mechanisms were revealed. In basic condition, one-proton and one-electron PCET prior to rate determining step dominates. But, in acidic condition, CD of Mn(III) predominates.

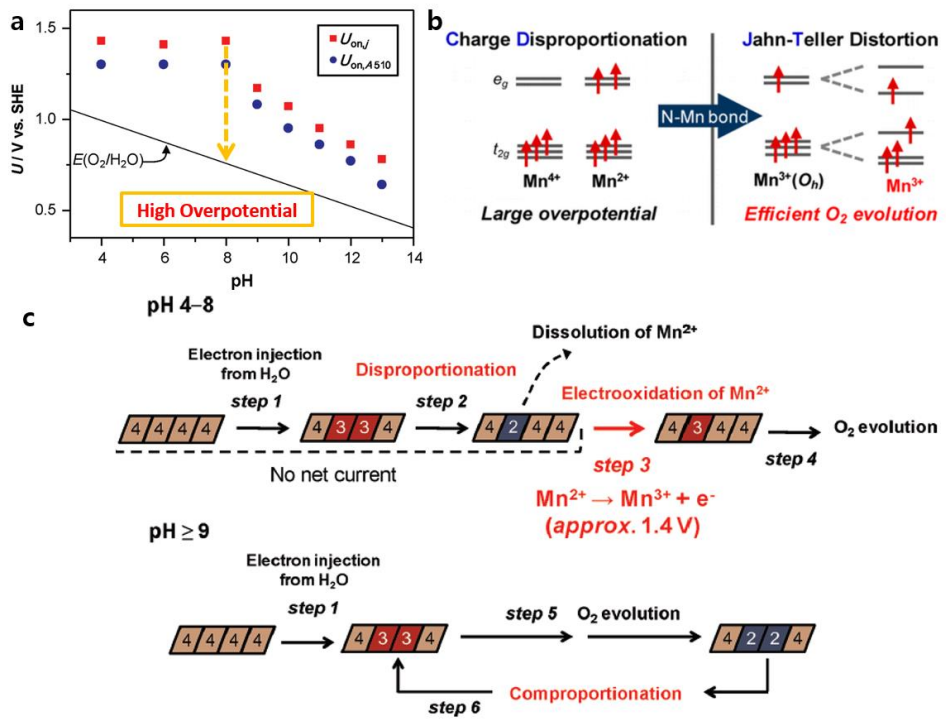


Figure 1.17. (a) pH dependences of the onset potential for oxidation current ($U_{\text{on,j}}$, red squares) and optical absorption at 510 nm ($U_{\text{on,A510}}$, blue circles). The solid line represents the standard potential for water oxidation^[47] (b) Schematic representation of electronic structure change for charge disproportionation and Jahn-Teller distortion^[48] (c) Schematic representation for oxidation states of Mn ions involved in the water oxidation on $\delta\text{-MnO}_2$ at pH 4-8 and pH > 9.^[47]

1.7. The 10 nm-sized Mn oxide nano-catalysts in neutral pH

1.7.1. OER activity and structural analysis for Mn oxide nanoparticles

Our group previously reported sub 10 nm-sized Mn oxide nanoparticles (NPs) as OER electrocatalysts in neutral pH.^[49] The nanoparticles were uniformly synthesized as spherical shape by hot injection methods, well-known thermal decomposition methods. After synthesizing the nanoparticles, the Mn oxide NPs were uniformly spin-coated on the conductive bottom electrodes to fabricate nano-catalyst film with hundreds of nanometers-thickness. Then, the electrodes were annealed above 150°C to form assembled nanoparticles film with removing organic ligands.

The Mn-oxide NPs exhibited superior catalytic activity for OER in neutral pH compared to their bulk counterparts. The OER activity was dramatically enhanced with decreasing the size of NPs under 20 nm. As previously mentioned, OER activity in neutral pH is closely correlated with the stability of Mn(III) species on the catalyst surface. The EPR analysis supported that Mn(III) species were stabilized on the surface of Mn oxide NPs during catalysis, which was different characteristic from bulk MnO.

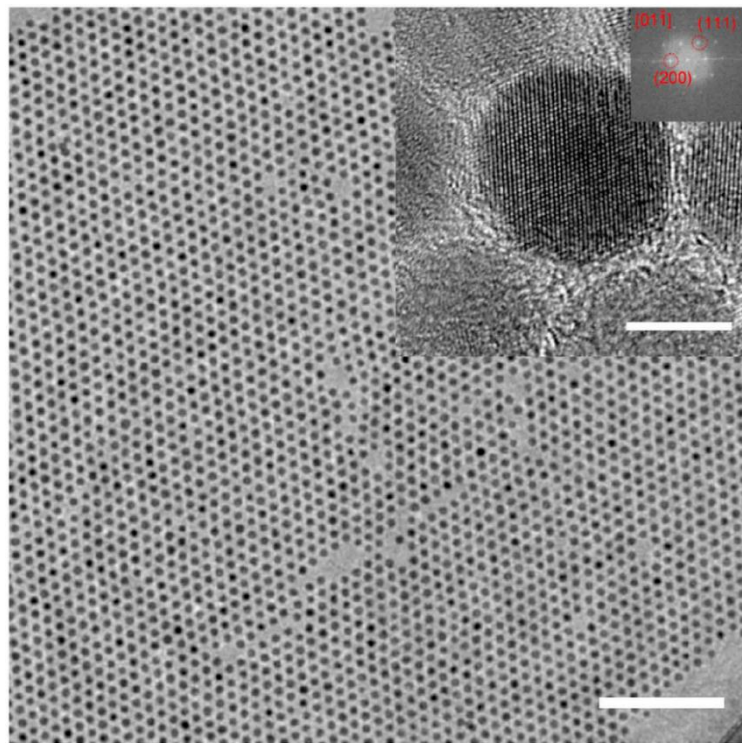


Figure 1.18. Transmission electron microscope (TEM) images for Mn oxide nanoparticles.^[49]

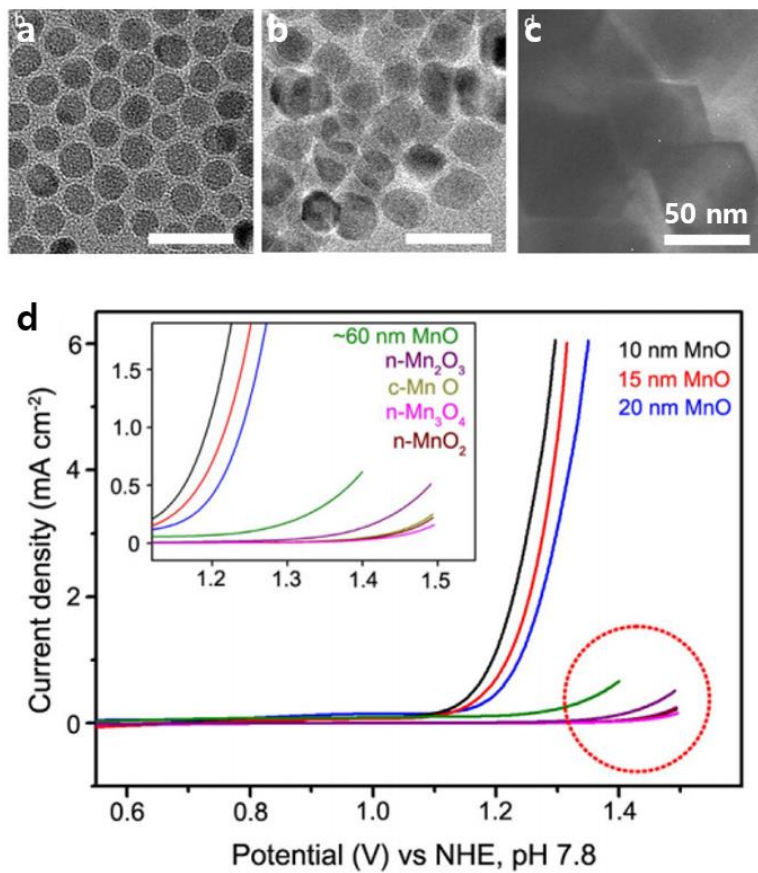


Figure 1.19. Transmission electron microscope (TEM) images for Mn oxide nanoparticles.^[49]

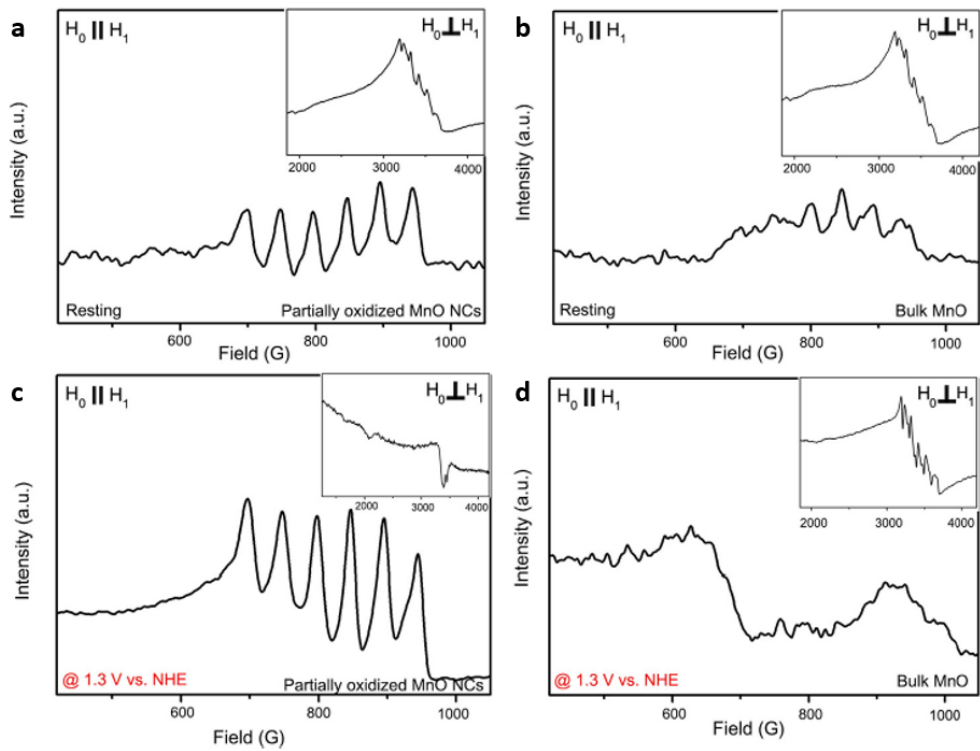


Figure 1.20. Parallel and perpendicular (inset) mode X-band CW-EPR spectra of Mn oxide NPs (a) in resting state, (c) at 1.3 V vs. NHE and bulk MnO (b) in resting state, (d) at 1.3 V vs. NHE^[49]

1.7.2. Reaction mechanism on the Mn oxide nanoparticles

1.7.2.1 Electrokinetic studies

Our group investigated reaction mechanism on the Mn oxide NPs combined with electro-kinetic studies and in situ spectroscopic analyses.^[50] From electro-kinetic studies, we estimated transfer coefficient (α) and proton reaction order, which gave information about involvement of electron and protons during catalysis.

Tafel plots for the Mn oxide NPs with various thicknesses were obtained from the polarization-corrected cyclic voltammetry curves. The Tafel slopes were measured as 82.6, 75.5, 70.1, and 78.2 mV/dec for 70, 150, 300 and 600 nm-thickness, respectively (Figure 1.19 a). The relationship between current density and applied potential was described by the following equation, where i_0 , α , F , E^0 and b are the exchange current density, transfer coefficient, Faraday constant, thermodynamic equilibrium potential and Tafel slope.

$$i = i_0 \exp\left(-\frac{\alpha(E - E^0)F}{RT}\right)$$

$$b = \left(\frac{\partial E}{\partial \log i}\right) = \frac{2.3 RT}{\alpha F}$$

The Tafel slope for 70~80 mV/dec, corresponded to 2.3 RT/F, indicated that transfer coefficient was calculated as unity for OER on the Mn oxide NPs. The unity of transfer coefficient represented that a reversible one-electron transfer step existed prior to rate determining step (RDS). The pH dependence of the OER activity was estimated near netural pH. The applied potential at the current density of 1 mA/cm²

were measured from pH 6.5 to pH 8.0. As shown in Figure 1.19 b, linear relationship was observed between the applied potential and pH. The slopes were measured as -84.1, -73.8, -71.8 and -76.8 mV/dec for 70, 150, 300 and 600 nm-thickness, respectively. In the electrochemical reaction rate law, the proton reaction order was calculated from the values of the Tafel slopes and pH-dependent potential changes.

$$\left(\frac{\partial E}{\partial \text{pH}}\right) = -\left(\frac{\partial E}{\partial \log j}\right) \left(\frac{\partial \log j}{\partial \text{pH}}\right)$$

The values of proton reaction order for each film-thicknesses was measured as -1, which indicated the inverse first-order dependence of the reaction rate on the proton activity. Based on the results of electrokinetic studies, the overall electrochemical reaction rate law for OER on the Mn oxide NPs was derived as the following equation.

$$j = k_0 (a_{H+})^{-1} \exp\left(\frac{FE}{RT}\right)$$

It indicated that one proton (1 H^+)-one electron (1 e^-) coupled transfer step existed prior to rate determining step in electrochemical OER on the Mn oxide NPs. The electrochemical characteristic for the nano-catalyst under neutral pH was clearly distinct from the conventional Mn-based catalysts. The conventional Mn-based catalysts typically showed Tafel slopes of 100~120 mV/dec and did not exhibit pH dependency near neutral pH. It indicated one electron transfer process prior to rate determining step.

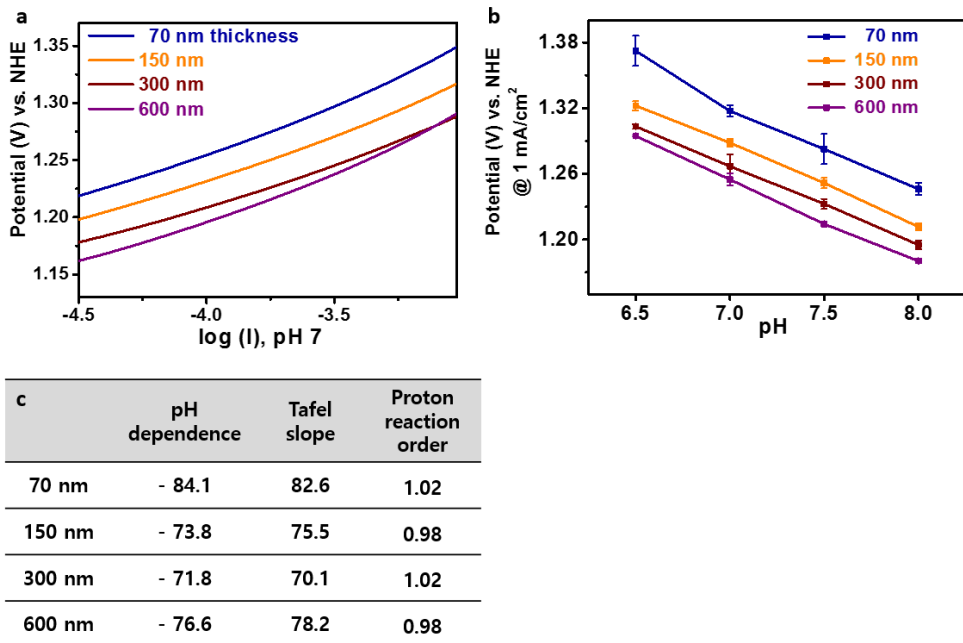


Figure 1.21. Electro-kinetic analysis for the Mn oxide NPs (a) Tafel plots near the onset potential (b) pH dependency over a neutral pH range (c) a summary table for the estimated proton reaction orders for the Mn oxide NPs with various thicknesses^[50]

1.7.2.2 *In situ* spectroscopic analyses

Various *in situ* spectroscopic analyses were performed for the Mn oxide NPs to demonstrate detailed reaction mechanism.^[50] Detecting metal valency change on the active sites and capturing reaction intermediates were regarded as key issues for mechanistic investigation for electrochemical water oxidation.

In situ X-ray absorption spectroscopy (XAS) analysis, which was separated into X-ray absorption near edge structure (XANES) and extended X-ray absorption fine structure (EXAFS) by energy range. *In-situ* XANES spectroscopy monitored the change of metal valency during catalysis, and *in-situ* EXAFS spectroscopy studied the bonding characteristic of the catalyst surface. Additionally, *in situ* Raman spectroscopy analyzed the phase and bonding nature on the catalyst surface during electrolysis. Furthermore, *in-situ* Uv-vis spectroscopic analysis supported the structure of reaction intermediates during OER.

Design of in-situ electrochemical cells for several spectroscopic analyses (XAS, Raman, UV-vis) is crucial to *in-situ* spectroscopic analyses. The ratio of active sites on the catalyst surface and electrolyte depth on the catalyst film need to be considered to obtain clear spectroscopic data. Our group established in situ electrochemical cell to reveal water oxidizing reaction mechanism on the Mn oxide NPs. The generation of oxygen bubbles was limitation for the *in situ* experiments for OER electrolysis at high potential.

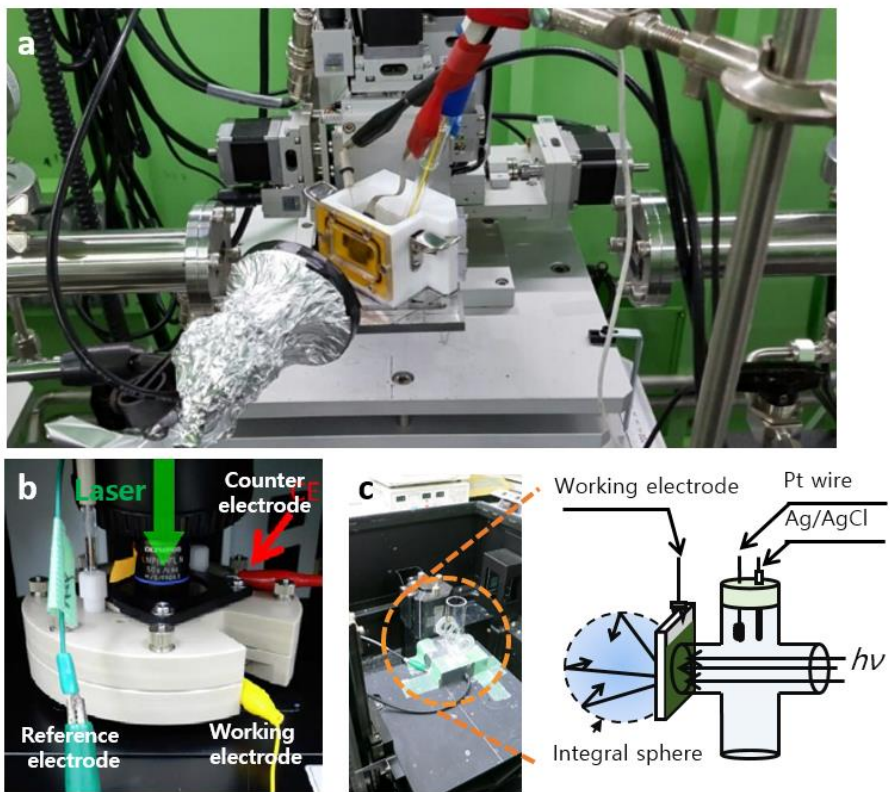


Figure 1.22. *In situ* electrochemical cell for mechanistic studies on the Mn oxide nanoparticles (a) X-ray adsorption spectroscopy (XAS) (b) Raman spectroscopy (c) UV-vis spectroscopy.

In situ XANES analysis was performed to monitor Mn valency during OER catalysis. As the applied potential increased, the surface of Mn oxide NPs film was gradually oxidized. The Mn valency was measured as 2.7, 3.2, 3.5 and 3.6 at 0.4, 1.1, 1.3 and 1.4 V vs. NHE, respectively. It indicated that high valent (>3) Mn species are generated on the surface of nanoparticles during OER. Furthermore, *in-situ* EXAFS studies reflected that Mn-O bonding length slightly decreased at high potential (1.4 V vs. NHE).

In situ Raman and UV-vis spectroscopic analyses were conducted to understand structural change for the surface of the Mn oxide NPs. We observed the potential-dependent spectra change in the *in situ* Raman spectra on the Mn oxide NPs. Additionally, for the *in situ* UV-vis spectroscopic analysis, spectral changes were also monitored as the applied potential increased. We observed broad peak and shoulder at the wavelength of 400 nm and 600 nm, respectively. The spectra change also showed reversibility with the applied potential.

Based on the *in situ* spectroscopic results, high valent (> 3) manganese oxo species were generated as reaction intermediates on the Mn oxide NPs for electrochemical water oxidation.

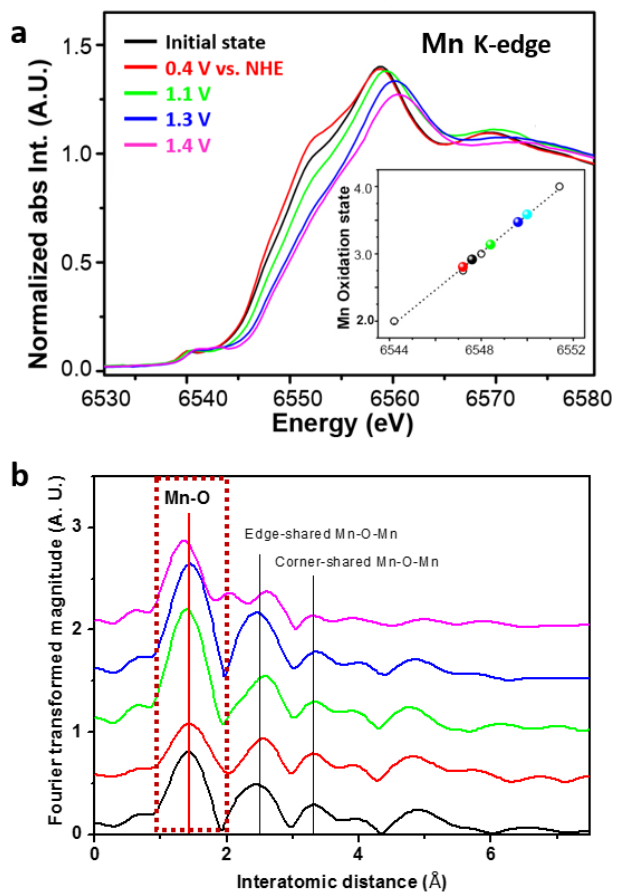


Figure 1.23. *In situ* electrochemical cell for mechanistic studies on the Mn oxide nanoparticles (a) X-ray adsorption spectroscopy (XAS) (b) Raman spectroscopy (c) UV-vis spectroscopy.^[50]

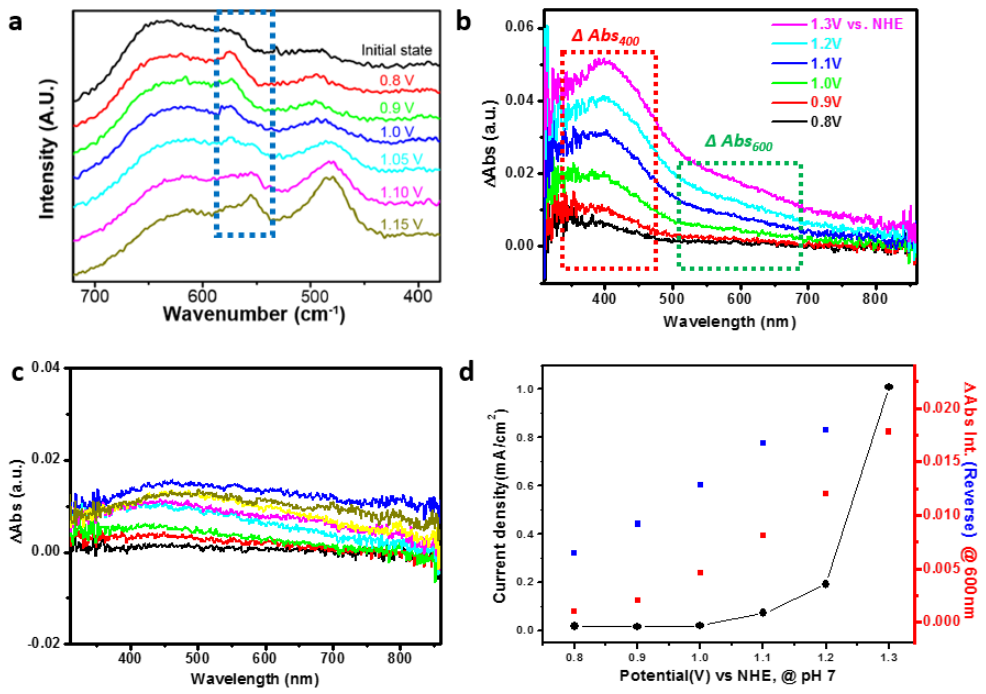


Figure 1.24. (a) *In situ* Raman spectroscopic data and (b) *in situ* UV-vis spectroscopic data, difference spectra based on the applied potential on the Mn oxide NPs during OER. (c) *In situ* UV-vis difference spectra of bulk MnO (d) potential dependence of the current density and differential absorabance of 600 nm for the Mn oxide NPs^[50]

1.7.3. Reaction mechanism on the Mn oxide nanoparticles

Combined with electrokinetic studies and *in situ* spectroscopic analyses, our group investigated distinct reaction mechanism for OER on the Mn oxide NPs.^[50] As previously reported, the rate-determining step for conventional Mn-based catalysts is one-electron transfer step, $\text{Mn(II)} \rightarrow \text{Mn(III)} + \text{e}^-$. In contrast, for the Mn oxide NPs, a concerted one proton (1 H^+)-one electron (1 e^-) transfer proceeds as quasi-equilibrium step prior rate-determining step (RDS). Various *in situ* spectroscopic results supported that Mn(IV)=O intermediates could be captured before RDS on the Mn oxide NPs during electrolysis. The rate-determining step for the Mn oxide NPs was O-O bond formation step by nucleophilic attack of Mn(IV)=O species. Therefore, our group revealed the distinct water oxidizing reaction mechanism on the Mn oxide NPs from conventional Mn-based electrocatalysts.

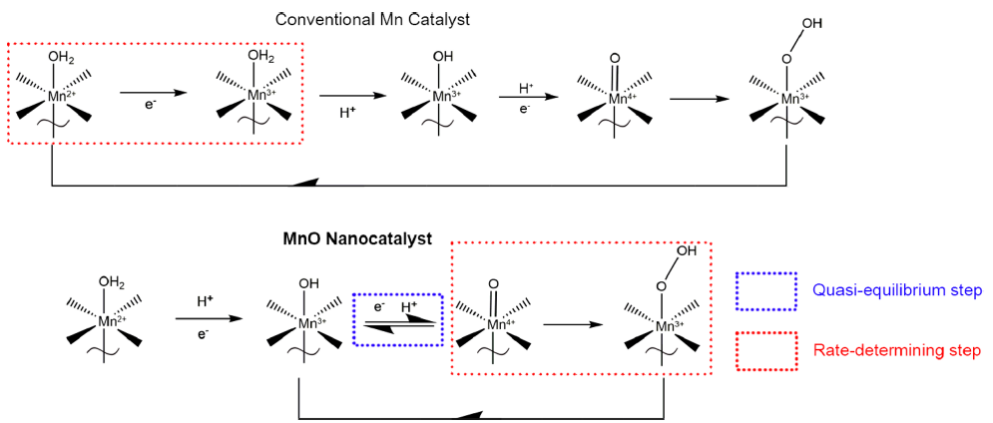


Figure 1.25. Reaction mechanism for electrochemical water oxidation on the conventional Mn-based catalyst (top) and the Mn oxide NPs (bottom)^[50]

1.8 Electrochemical impedance spectroscopic analysis on film-type electrocatalysts

Electrochemical impedance spectroscopy (EIS) is an effective tool to separate and analyze various electrochemical processes in energy materials. Impedance is defined as the complex form of resistance. Electrochemical impedance is measured from the potential-current relationship with sinusoidal function ($E = i \cdot Z$). The EIS spectra is generally fitted with the proper circuit model and physical parameters explained by circuit elements are extracted.

For instance, dye-synthesized solar cells (DSSCs) have been well-known system to be analyzed by EIS. The TiO_2 nanoparticles layer in DSSCs, charge recombination and electron transports proceeds concomitantly. Utilizing transmission line model, charge transport and charge transfer processes were decoupled.

For OER electrocatalysts, EIS analyses focused on understanding only surface catalysis kinetics on the interface between catalyst-film and electrolyte. Suib group previously reported that charge transfer resistance, estimated by EIS analysis with simple circuit model, reflected OER activity trend for various manganese oxides.^[39] Additionally, Lyon group conducted EIS analysis for transition metal hydroxide-based catalyst film.^[51] The faradaic resistance (R_{far}) was estimated by fitting analysis with the circuit models. The Tafel slopes were calculated by the values for faradaic resistance. It indicated that EIS studies for OER electrocatalysts was conducted for investigation of surface catalysis process. However, the advanced EIS analysis is

required to decouple various electrochemical processes in the OER electrocatalyst film during catalysis, such as electron transport process and charging behavior. .

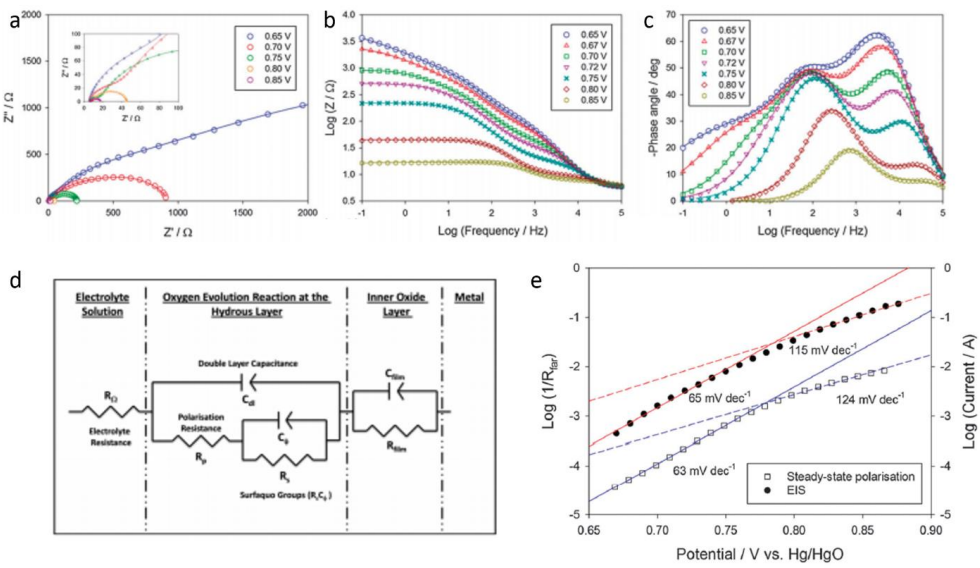


Figure 1.26. (a-c) Electrochemical impedance spectra recorded in 1.0 M NaOH at a series of potentials associated with active oxygen evolution for transition metal hydroxide electrode (d) Equivalent circuit model for fitting analysis (e) Tafel plots generated from EIS and steady-state polarization data

1.9 Scope of thesis

The Mn oxide NPs exhibited superior catalytic activity and distinct reaction mechanism for OER. To understand detailed reaction mechanism, we focused on investigation for various electrochemical processes on the Mn oxide NPs film-type electrocatalysts. The catalytic performance of Mn oxide NPs film is determined by not only surface catalysis but also electron transport process. We investigated various electrochemical processes for the film-type Mn oxide NPs catalyst by electrochemical impedance spectroscopy (EIS).

Chapter 2 investigated kinetic parameters extracted by fitting analysis with our proposed transmission line models. In our proposed circuit model, capacitive elements were Havriliak-Negami capacitors to explain polarization-delay by charged intermediates on the Mn oxide NPs. From fitting analysis, electron transport process and surface catalysis were clearly decoupled by obtaining transport resistance and interface resistance. We found that protons are involved that not only surface catalysis but also electron transport by H/D istope experiments. Furthermore, reaction rate constant (k) was calculated from fitting analysis by our proposed circuit model.

Chapter 3 investigated charging process on the Mn oxide NPs during OER catalysis by complex capacitance analysis. Complex capacitance analysis has been conducted for capacitive materials to understand kinetics for charging process. For the Mn oxide NPs, Mn valence changed from Mn(II) to Mn(IV) during OER

catalysis. Real capacitance indicated the charring process on the interface between electrolyte and the catalyst surface. Imaginary capacitance reflected energy dissipation process, such as OER catalysis. Potential dependent change for real and imaginary capacitance demonstrate We newly the proposed dissipation ratio as the ratio of the real capacitance with respect to the imaginary capacitance for analysing the energy balance between the charge-accumulation process and charge dissipation for a catalytic reaction. The potential-dependence of the dissipation ratio indicated that the charge-dissipation process was superior to charge accumulation at higher potential.

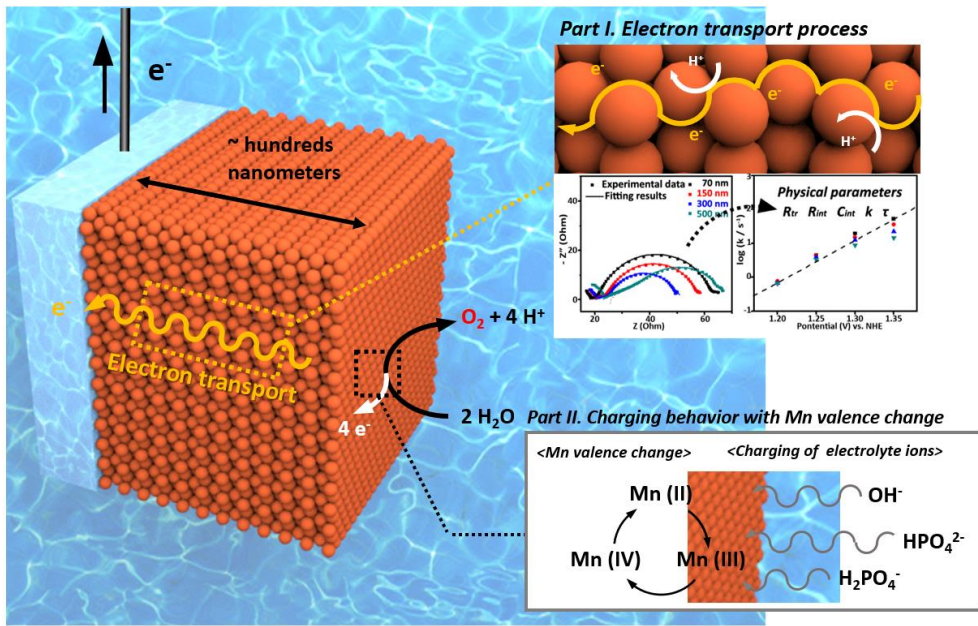


Figure 1.27. Schematic representation for the scope of thesis

1.10 Concluding remarks

Hydrogen energy has been an attractive alternative energy source due to its environment-friendly characteristic and high energy density. Water electrolysis is promising methodology to produce hydrogen energy without harmful byproducts. However, the anodic half reaction, oxygen evolution reaction (OER), is regarded as major bottleneck for the overall efficiency of water electrolysis system.

The noble-metal based catalysts, such as RuO₂ and IrO_x, were previously reported for OER electrocatalysts. To solve these scarcity and high cost, substantial research effort has been devoted to develop transition metal-based electrocatalysts. Inspired by Mn₄CaO₅ cluster in Photosystem II, our group developed sub 10 nm-sized Mn oxide nanoparticles as water oxidizing electrocatalysts in neutral pH. It showed superior catalytic activity and distinct reaction mechanism compared to conventional Mn-based electrocatalysts.

In this thesis, we conducted electrochemical impedance spectroscopy analysis for the film-type Mn-oxide NPs catalysts. Kinetic parameters were extracted by fitting analysis with our proposed circuit model. It decoupled electron transport process and surface catalysis. It explained proton involvement in electron transport process. Furthermore, we performed complex capacitance analysis to understand charging behavior on the Mn oxide NPs during catalysis. We believe that these EIS analysis can be generalized to various electrochemical reactions.

Chapter 2. Parametric studies on Mn oxide nanocatalysts using equivalent circuit model

2.1 Introduction

Transition metal (TM)-based electrocatalysts are generally fabricated as film-like structures on bottom electrodes. In contrast to sparsely decorated noble-metal-based catalysts, most film-type TM electrocatalysts exhibit an optimal OER catalytic efficiency at a considerable thickness. Electrodeposited amorphous Co oxide (Co-Pi), a well-known film-type OER catalyst without a conducting carbon support, showed saturation for OER activity at thicknesses greater than 3 μm .^[52] Inside Co-Pi films, the electrolyte and reactants are freely permeable due to the moderate porosity of the film. Thus, protons and electrolyte molecules are involved in electron transport processes in Co-Pi films. The OER activity for most film-type catalysts is explained by the competition between an increased number of active sites and increased resistance to electron transport through the catalyst film. The number of active sites increases with thickness because the surface of TM catalyst films is porous and rough. The increase in the number of active sites enhances the OER activity as the catalyst film thickens. However, the increase in electron transport resistance with thickness decreases the catalytic activity. Thus, the optimal thickness

for TM electrocatalysts is determined by the competition between these two conflicting factors. Furthermore, charge transport properties for electrocatalysts could be strongly correlated to their electronic and structural factors from the comparative study between Co–Pi and Co–Bi.^[53]

With the same catalyst material, the performance can be changed significantly, even by a few orders of magnitude, depending on the thickness of the deposited film. Therefore, in designing a TM-based electrode to maximize performance, the transport-related electrokinetic parameters should be analyzed exactly in addition to the intrinsic catalytic properties. Furthermore, it is still interesting to investigate how electron transport occurs over a substantial distance (~a few hundred nanometers) across the film to the bottom electrode during catalysis.

Various analytical approaches have been attempted to investigate the oxygen evolution mechanism on film-type TM catalysts. Electrokinetic studies are fundamentally conducted to evaluate the numbers of electrons and protons involved in each charge transfer step.^[21] The transfer coefficient and proton reaction order are calculated from Tafel analysis and the measured pH dependence of catalytic activity, respectively. Combined with electrokinetic studies, the valence change of metal sites offers decisive clues for understanding redox behavior in the overall OER mechanism. Thus, various in-situ spectroscopic analysis, including X-ray absorption near-edge structure (XANES) analysis, electron paramagnetic resonance (EPR) and X-ray photoelectron spectroscopy (XPS), have been performed to observe the valence change of transition metal sites during catalysis.^{[14], [54], [55]} Furthermore, to

obtain direct evidence for the OER mechanism, reaction intermediate species have been captured by in-situ FT-IR and Raman analysis.^{[13],[56]} Additionally, computational studies have been widely performed to apprehend the energetically favorable pathways or structurally stable structures of reaction intermediates during the OER. Until now, most approaches have been focused on a mechanistic investigation of surface catalysis to determine and control the rate-determining step. However, near the optimum film thickness, the transport parameters start to significantly contribute to the overall reaction kinetics. Thus, an additional analytical approach is necessary to obtain and decouple transport-related parameters, which have been disregarded in most previous OER studies.

Electrochemical impedance spectroscopy (EIS) is an effective technique to decouple multiple electrochemical processes in various energy materials, such as dye-synthesized solar cells (DSSCs),^[57-60] photoelectrochemical cells (PECs),^[60-61] solid-oxide fuel cells (SOFCs)^[62-63] and hydrogen-evolution reaction (HER) electrocatalysts.^[64] A successful example of EIS is the kinetic analysis of DSSCs, where photoexcited electrons from the dye move to TiO₂ nanoparticle (NP) electrodes and subsequently transport through micrometer-thick TiO₂ films. EIS analysis can be used to decouple simultaneous resistance to electron transport and charge transport to understand the detailed kinetics. Furthermore, various physical parameters such as the electron lifetime and diffusivity have been obtained to demonstrate electrochemical phenomena in the whole system and to improve the overall electron extraction efficiency.

However, in the case of OER catalysts, EIS has mostly been utilized to measure only the charge transfer resistance (R_{CT}), which is characteristic of surface reactions.^[39] The measured R_{CT} can be correlated with the Tafel slope and exchange current density, which are obtained in Tafel analysis by the following equation (Eq. 1). In the equation, R_{CT} , b , i_0 , and E indicate the charge transfer resistance, Tafel slope, exchange current density and potential, respectively.

$$\log\left(\frac{1}{R_{CT}}\right) = \log\left(\frac{2.303 i_0}{b}\right) + \frac{E}{b} \quad (\text{Eq. 1})$$

Therefore, a comparison of R_{CT} values can directly reveal the OER activity trend. Experimentally, R_{CT} can be easily extracted from a well-known simple circuit model by fitting spectra in the low-frequency range. In most cases, the high-frequency region has not been carefully interpreted by previous circuit models, although this region should have meaningful information about transport processes through catalyst films.

The capacitive behavior of OER electrocatalysts was not perfectly explained by a pure capacitor, because not only simple charging but also faradaic processes simultaneously occur on the surface of catalyst films. Because of non-ideal capacitive behavior, the experimental data in Nyquist plots are not displayed as straight lines or perfect semicircles, which would describe a pure resistor or capacitor, respectively. To fit general spectra perfectly, a frequency-dependent capacitive element called a constant phase element (CPE) is utilized as the capacitive element in circuit modeling, although Cole and Cole originally introduced the substitution of CPEs for resistive elements to describe the deviation from the Debye response of

real dielectrics.^[65] The impedance (Z) of the CPE is expressed as $Z = 1 / (Q(j\omega))^\alpha$, where ω and α are the angular frequency and dispersion parameter ($0 \leq \alpha \leq 1$), respectively. When α is 0 or 1, the CPE is regarded as a pure resistor or pure capacitor, respectively. Values of α between zero and unity indicate a phase angle of $(\pi/2)\alpha$ for the line response in the impedance plane, hence the “constant phase” in CPE. CPEs are widely used in state-of-the-art impedance analysis, where arbitrary α parameters often result in apparent descriptions of the spectra.

However, the dispersion parameter (α) for CPEs is randomly varied in the fitting process, and a small change in α is strongly correlated with the other physical parameters in the fitting results. Thus, new capacitive elements with physical insight are needed to replace CPEs in impedance analysis. It has previously been reported that dielectric relaxation models such as the Debye, Cole-Cole, Cole-Davidson and Havriliak-Negami (H-N) functions describe capacitive behaviors for polymers and polycrystalline solid electrolytes.^[66-67] We thought that the dielectric relaxation model could also explain the capacitive behavior of the complicated electrochemical process of OER catalyst films.

Furthermore, transmission line models are typically used in EIS analysis for porous electrodes where catalytic reactions occur throughout the depth of the catalyst film. The transmission line is composed of ion-transport resistance elements distributed along the film thickness, i.e., in series, and the charge transfer resistance and double-layer capacitance at the interfaces along the thickness. The latter

components are thus connected in parallel. This model has been applied to DSSCs and SOFCs where the respective components represent other rate-controlling mechanisms, such as electron drift, diffusion and recombination in semiconducting oxides; and surface diffusion and adsorption in gas electrodes. Parallel-connected RC loops and serial resistive elements indicate catalytic reactions and charge transport, respectively. It has previously been reported that the transmission line model was utilized to obtain kinetic information for the OER catalyzed by transition metal (oxy)hydroxide films in alkaline conditions.^[68] Using the transmission line model, kinetic information for film-type TM catalysts was decoupled into the components of electron transport along the film and catalytic reaction on the active sites.

Specifically, in TM-assembled film-type electrocatalysts, the electron transport process significantly contributes to determining the overall catalytic performance, unlike in noble-metal-based catalysts. Furthermore, on the surface of TM catalyst films, metal-oxo species are generated during oxygen evolution catalysis. To initiate O-O bond formation efficiently, oxo species hopped on the surface of the catalyst. Based on density functional theory (DFT) analysis, the hopping of Co(IV)=O species energetically favors the generation of O-O bond formation in Co₃O₄ catalysts.^[69] For the EIS analysis of TM catalyst films, a more advanced circuit model should be established to decouple and investigate these various processes during the OER.

Recently, inspired by the asymmetric structure of the CaMn₄O₅ cluster in photosystem II, which shows an extremely high OER efficiency, we synthesized

monodisperse 10-nm Mn oxide nanoparticles (NPs) via thermal decomposition.^[49]

Then, partially oxidized Mn oxide NPs were developed through the application of surface NH₄OH and heat treatment. We previously developed a hydrated manganese phosphate compound ($Mn_3(PO_4)_2 \cdot 3H_2O$) and lithium manganese pyrophosphate ($Li_{2-x}MnP_2O_7$), which exhibited high OER activity under neutral pH.^[70-71] It was also revealed that the high efficiency caused by the asymmetric Mn geometry and stabilizing Mn(III) species. We also examined stabilizing Mn(III) species on the surface of Mn oxide NPs.

Furthermore, we investigated the OER mechanism on the surface of the Mn oxide NPs films with an electrokinetic study and in-situ spectroscopic analysis.^[50] The Mn valence change on the Mn oxide NPs surface was detected via EPR and in-situ XANES analysis. Additionally, OER intermediates, Mn(IV)=O species, were detected via in-situ UV-vis and Raman spectroscopic analysis during catalysis. Based on these analyses, the unique OER mechanism mediated by the the Mn oxide NPs differed from that observed for their bulk counterparts.

Here, we conducted EIS analysis to extract various kinetic parameters to describe the complicated electrochemical processes in hundred-nanometer-thick Mn₃O₄ NPs films.^[72] For fitting analysis, a new transmission line model was established where the H-N function was applied as generalized capacitive elements that provide well-defined capacitance components and dispersive characteristics previously addressed by CPEs.^[72] As a result, the analysis using a modified transmission line model provided meaningful parameters to describe the catalytic behavior of Mn₃O₄ NPs.

films. Furthermore, the proposed impedance analysis model is generally applicable to film-type electrocatalysts to reveal specific mechanisms according to the behavior of kinetic parameters.

2.2 Experimental Methods

2.2.1. Materials

Mn(CH₃COO)₃·4H₂O (99 %), 1-octadecene (90%), myristic acid (CH₃(CH₂)₁₂COOH) (99%), decanol (CH₃(CH₂)₉OH), Na₂HPO₄·7H₂O (ACS reagent, 98.0-102.0 %), and NaH₂PO₄·2H₂O (99.0 %) were purchased from Sigma Aldrich and used as received without further purification. Fluorine-doped-tin-oxide-coated glass (FTO, TEC-8) with the surface resistivity of 15 Ω sq⁻¹ was manufactured by Pilkington Company.

2.2.2. Synthesis of the Mn₃O₄ NPs

The Mn₃O₄ NPs were synthesized by slightly modifying a previously reported method called the hot injection method.^[49] To synthesize monodisperse sub-10-nm-sized nanoparticles, 1 mmol of manganese acetate and 2 mmol of myristic acid were dissolved in 20 mL of octadecene and the mixture of 1.83 ml of decanol and 3 mL of octadecene were prepared. These two separate solution were degassed at 110 °C for 2 hours with stirring. After 2 hours of degassing, the solution of manganese acetate and myristic acid was slowly heated up to 290 °C under argon atmosphere. When the temperature reached above 285 °C, the 1.2 ml mixture of decanol and octadecene was injected rapidly into the solution of Mn(ac)₃ and myristic acid. The mixture was maintained at 290 °C for 1 hour.

2.2.3. Electrode fabrication

After the synthesis of Mn₃O₄ NPs in octadecene, the solution of Mn₃O₄ NPs, toluene and acetone were mixed in the volume ratio of 1:1:2 and centrifuged to precipitate of the Mn₃O₄ NPs. This step was repeated three times. Then, the precipitate of Mn₃O₄ NPs was dispersed in hexane. Then the 40µl of MnO NPs solution was spin-coated onto the FTO substrates at the spin rate of 2000 rpm and the holding time of 10 sec. The thickness of the MnO NP film spin-coated on the FTO substrates was controlled by the volume ratio of the initial dark brown Mn₃O₄ NP solution to hexane. To eliminate the surfactant on the surface of the MnO NPs, the spin-coated film on the FTO substrates were dipped in a diluted NH₄OH solution for 1 hour and annealed at 250 °C for 1 hour.

2.2.4. Scanning electron microscopy (SEM)

The morphology of the Mn₃O₄ NPs films on the FTO substrates was characterized with a high resolution scanning electron microscope (Supra 55VP, Carl Zeiss, Germany). After deposition of the MnO NPs, the substrate was gently rinsed in deionized water at least 3 times and dried with nitrogen gas. Images were taken with an acceleration voltage of 2 kV, and EDX spectra with a 15 kV.

2.2.5. Transmission electron microscopy (TEM)

TEM images and selected area electron diffraction (SAED) patterns were obtained using a high resolution transmission electron microscope (JEM-3000F, JEOL, Japan) with the acceleration voltage of 300 kV. To prepare TEM samples, the MnO NPs dispersed in hexane were dropped on the TEM grid and dried in air.

2.2.6. Electrochemical measurement

All electrochemical experiments were conducted in a three-electrode system. Ag/AgCl/3M NaCl and Pt plate were used as a reference electrode and a counter electrode, respectively. Electrochemical tests were carried out at room temperature using a potentiostat. The electrode potential vs Ag/AgCl was converted to the NHE scale, using the following equation: $E(\text{NHE}) = E(\text{Ag/AgCl}) + 0.197 \text{ V}$. Additionally, overpotential values were calculated by the difference between the iR -corrected potential ($V = V_{\text{applied}} - iR$) and the thermodynamic potential of water oxidation at a specified pH. 500 mM phosphate buffer (pH 7) was used as the electrolyte.

2.2.6.1. Cyclic Voltammetry (CV)

Prior to every cyclic voltammetry measurement, the solution resistance was measured and all the data were iR -compensated. The CV curves were polarized-

corrected to remove non-faradaic contribution. Scan rate for all CV curves was 0.01 V/s.

2.2.6.2. Electrochemical Impedance Spectroscopy (EIS)

The electrochemical impedance spectroscopy was measured in the frequency range from 10^{-1} to 10^5 Hz with 5 mV amplitude. During analysis, electrolyte was stirred by magnetic bar to remove the oxygen bubbles on the surface of electrodes.

2.2.6.3. Electrochemically Active Surface Area (ECSA) measurement

The potential range for measuring electrochemically active surface area (ECSA) was 0.2 V window centered at the open-circuit potential. The CV measurement were conducted by sweeping potential across the non-faradaic region at 8 different scan rates : 0.5, 1, 2.5, 5, 7.5, 10 mV/s

2.3 Results and Discussions

2.3.1. Synthesis of monodisperse 10 nm-sized Mn₃O₄ nanoparticles and the fabrication of film-type nano-catalyst electrode

The 10 nm-sized Mn₃O₄ NPs were successfully synthesized as a monodisperse spherical shape. The Mn₃O₄ nanoparticles were synthesized with small amount of surfactant which was 2 mmol of myristic acid. According to the previous study, the nuclei of nanoparticles were generated by injection process of alcohol surfactant, decanol. The TEM imgases showed the uniformity of size of nanoparticles. (Figure 2.1)

The XRD patterns for the Mn₃O₄ NPs electrode were well matched with tetragonal hausmannite (JCPDS no. 00-024-0734) (Figure 2.2). It indicated that two Mn(III) octahedral sites and one Mn(II) tetrahedral site were in unit cell of the crystalline Mn₃O₄ NPs.^[73]

Subsequently, the Mn₃O₄ NPs were uniformly coated on fluorine-doped tin oxide (FTO) substrates by spin coating. Then, the spin-coated electrodes were dipped in a diluted NH₄OH solution for 1 hour and annealed at 250 °C for 1 hour. As shown in Figure 2.3, plane-sectional scanning electron microscopy (SEM) image showed that spin-coating methodology fabricated uniform nano-catalyst layer. Furthermore, the thickness for Mn₃O₄ NPs film was precisely controlled from 20 nm to 500 nm (Figure 2.4).

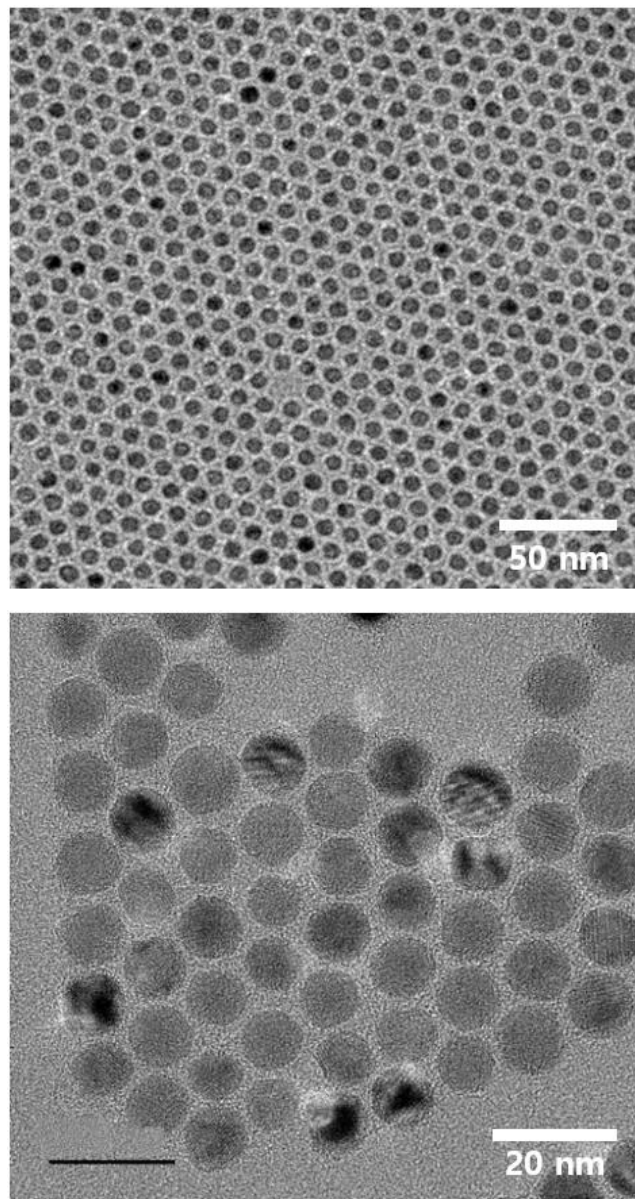


Figure 2.1. Transmission electron microscopy (TEM) image of synthesized Mn_3O_4 NPs.^[72]

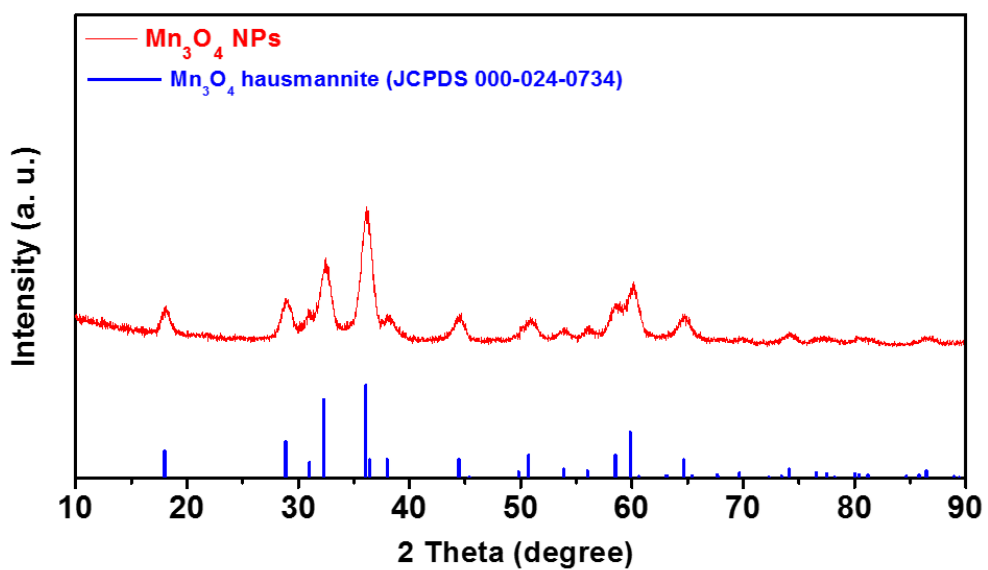


Figure 2.2. X-ray diffraction data for synthesized Mn_3O_4 NPs.^[73]

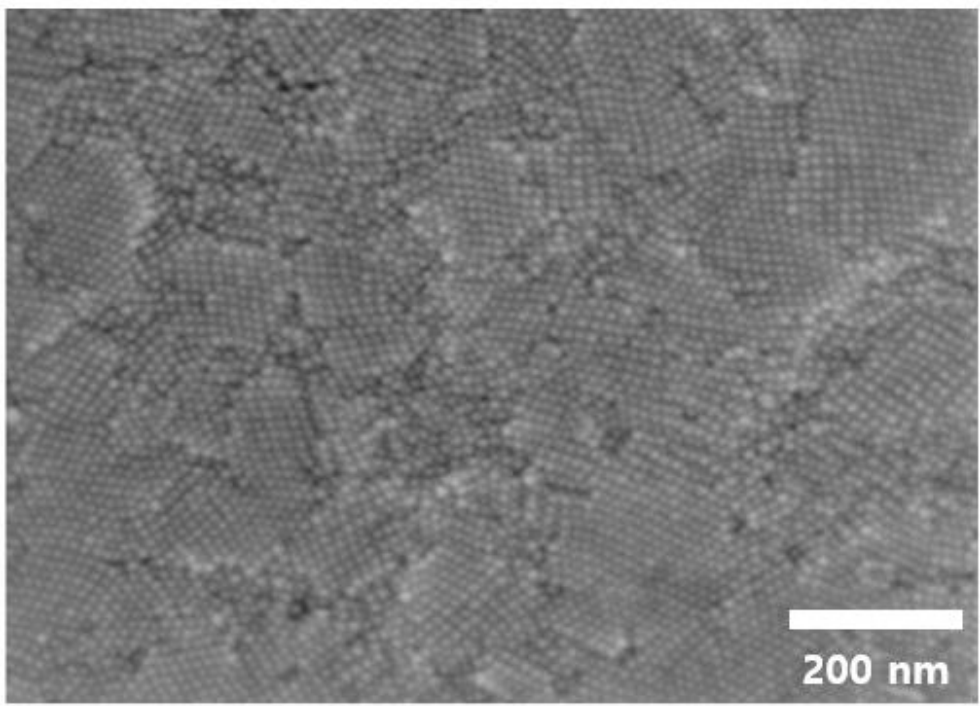


Figure 2.3. Plane sectional scanning electron microscopy (SEM) images of Mn₃O₄ NPs electrode

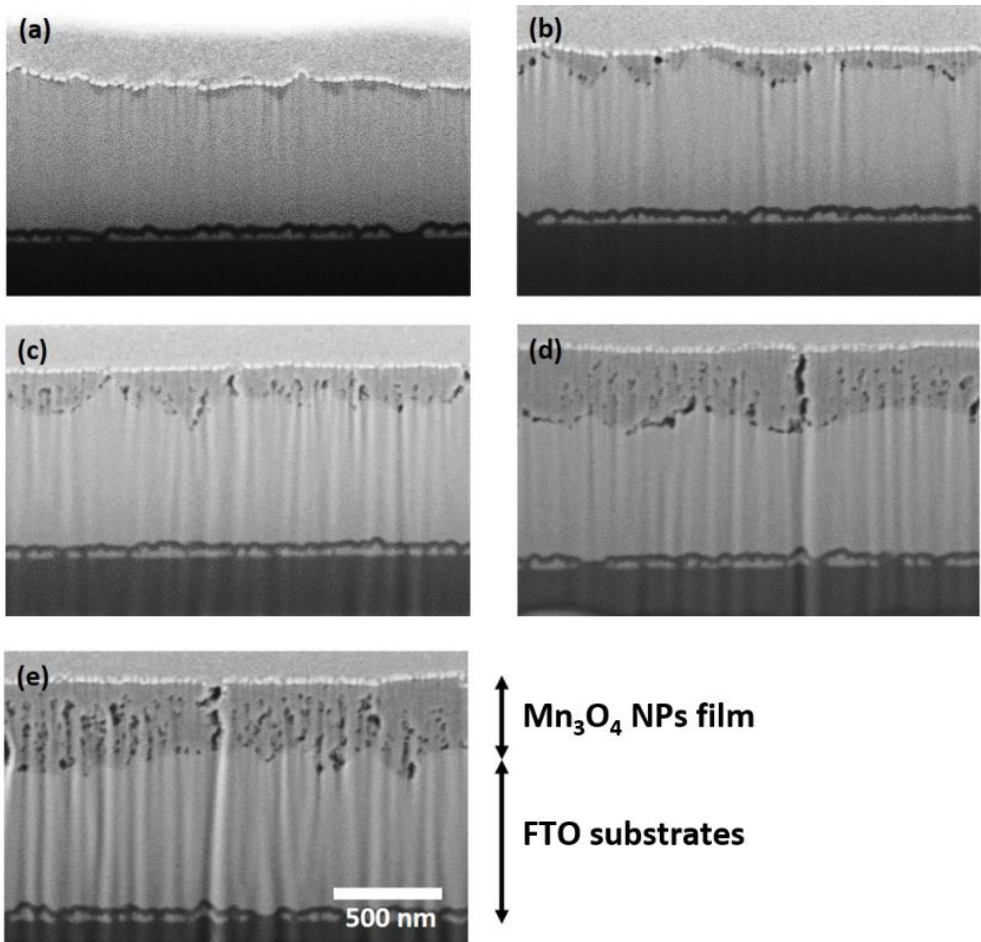


Figure 2.4. Cross sectional scanning electron microscopy (SEM) images of (a) 20 nm-thickness, (b) 70 nm-thickness (c) 150 nm-thickness (d) 300 nm-thickness (e) 500 nm-thickness Mn₃O₄ NPs NPs electrode

2.3.2. OER activity for the Mn₃O₄ NPs catalyst film with various thickness

The OER activity for various thicknesses of Mn₃O₄ NPs film was evaluated by cyclic voltammetry (CV) in 0.5 M phosphate at pH 7. All CV curves were polarization-corrected to remove the contribution of nonfaradaic currents. The overpotential at a current density of 5 mA/cm² was 607, 576, 553, 535, and 544 mV for the 20, 70, 150, 300, and 500 nm-thick films, respectively. The slope of the 300 nm curve was steeper than that for the 500 nm film, and above 1.32 V vs NHE, the 300 nm film exhibited the highest catalytic current density among the several film thicknesses. The current density at 1.35 V vs NHE was 1.23, 2.34, 3.68, 4.96, and 4.45 mA/cm² for the 20, 70, 150, 300, and 500 nm-thick films, respectively. Below 300 nm, the current density gradually increased with thickness because the number of active sites increased as the porous catalyst film thickened. Over the 300 nm, the significant distance from the catalyst surface to the bottom electrode caused the restriction of electron transport. This restriction contributed to the decline in current density at a 500 nm thickness. The thickness dependent trend in catalytic activity can be explained by the competition of two factors: the number of active sites and the electron transport distance.

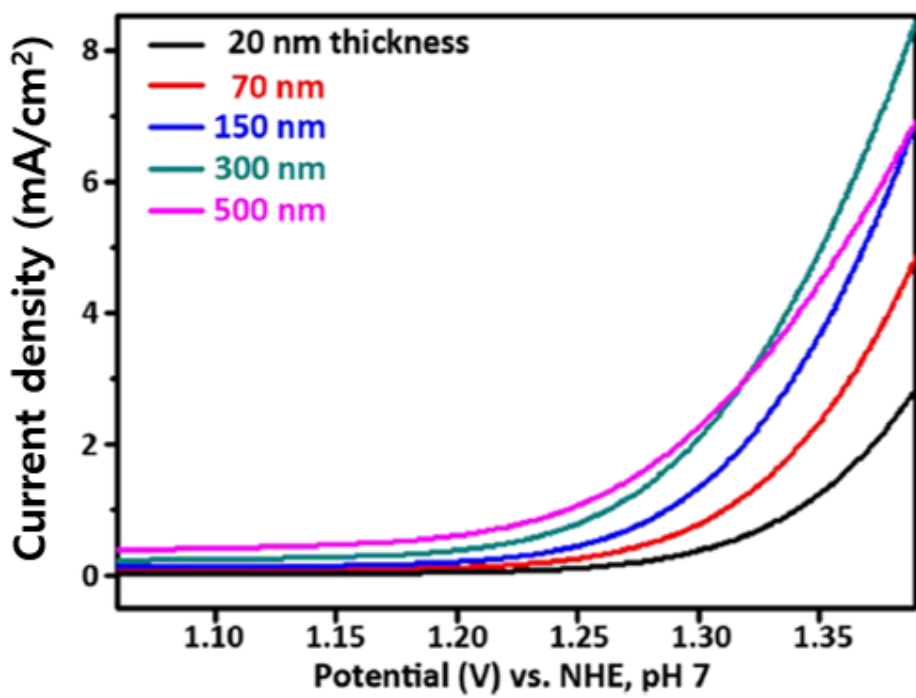


Figure 2.5. Polarization-corrected cyclic voltammetry (CV) curves for the 20, 70, 150, 300 and 500 nm thicknesses

2.3.3. Impedance analysis for the Mn₃O₄ NPs catalyst film with various thickness

We performed EIS analysis for each thickness of the Mn₃O₄ NPs film during oxygen evolution catalysis. From the Nyquist plot (Figure 2.6), we found that a new semicircle emerged in the high-frequency region at approximately 10³–10⁵ Hz. The semicircle became larger as the thickness increased. These thickness-dependent spectra in the high-frequency region were closely related to the resistance to electron transport processes. To obtain meaningful parameters related to electrochemical processes, including electron transport, we first conducted a fitting analysis for the impedance spectra using simple circuit models previously applied to film-type OER catalysts.

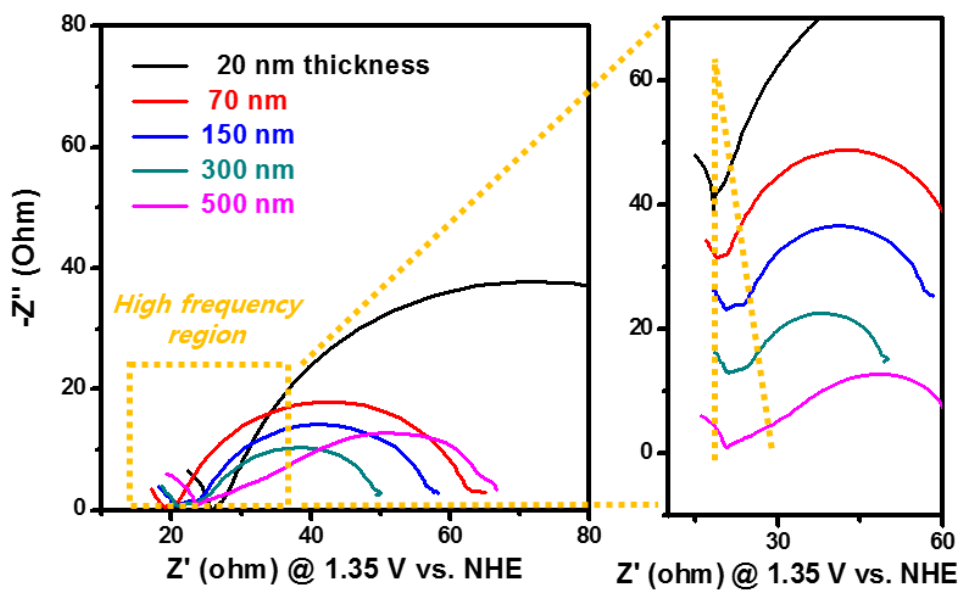


Figure 2.6. Nyquist plot of impedance data for Mn_3O_4 NPs film with the 20, 70, 150, 300 and 500 nm thicknesses at 1.35 V vs. NHE, where OER catalysis occurs briskly.

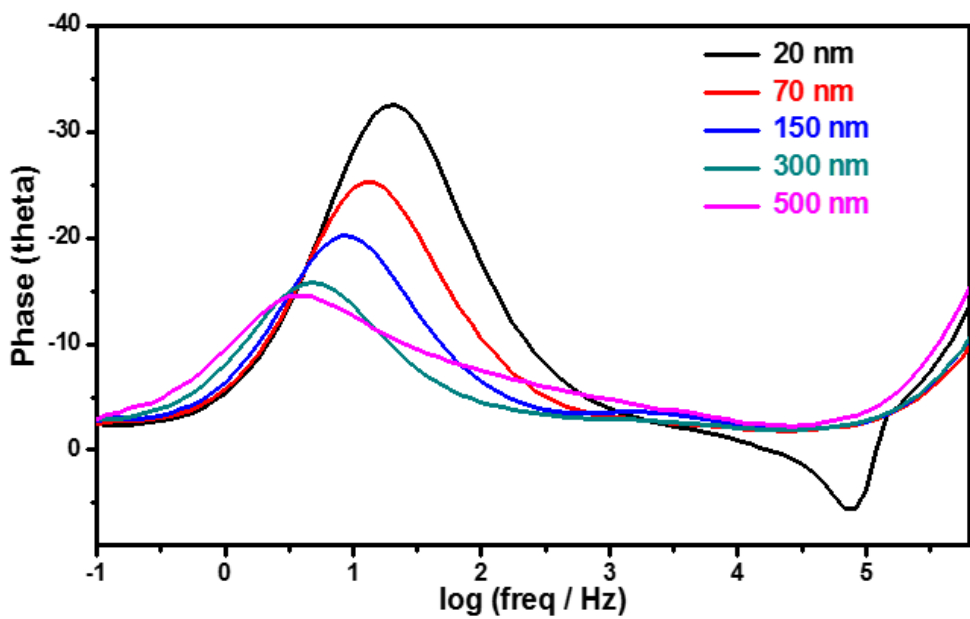


Figure 2.7. Bode plot for phase angle of Mn₃O₄ NPs film with the 20, 70, 150, 300 and 500 nm thicknesses at 1.35 V vs. NHE, where OER catalysis occurs briskly.

2.3.3. Fitting analysis with previous circuit model

Circuit model A is widely utilized for the qualitative comparison of overall catalytic efficiency (Figure 2.8a).^[39] The circuit model A is composed of three resistive elements and two capacitive elements. In the circuit model A, R_{Ω} represents the electrolyte resistance; R_f and C_f are the resistance and dielectric capacitance of the catalyst film, respectively; and R_{CT} and C_{dl} indicate the charge transfer resistance and double-layer capacitance which describe surface catalysis, respectively.

As shown in the Figure 2.9, the black lines with points represent the experimental data, and the red line represents the fitting results for the model A. The fitting results for model A are displayed by two semicircles in the Nyquist plots (Figure 2.9). The smaller semicircle in the high-frequency region originated from the R_f-C_f loop, and the other semicircle in the low-frequency region corresponded to the $R_{CT}-C_{dl}$ loop. We found that fitting results of model A deviated from the experimental data as the thickness increased (Figure 2.9). This deviation in fitting results was attributed to the oversimplification of the reaction kinetics. In the model A, the values of R_{CT} are estimated with the assumption that the current response is totally originated only from surface catalysis. Furthermore, the $R_{CT}-C_{dl}$ loop is applicable only to a one-step charge transfer reaction. Thus, the circuit model cannot fully analyze the circumstances of the OER, where four electrons are involved in a multiple charge transfer process. Therefore, we further adopted other previous models that can

incorporate the effect of multiple charge transfer kinetic.

The models B & C were reported by the Cahan & Chen group and Lyon group, respectively.^[51, 74] In models B & C, the R_{CT} -CPE_{dl} loop of model A is separated into two RC loops, R_P -CPE_{dl} and R_S -CPE_Φ, which indicate the interfacial charge transfer reaction. For multiple-step electrochemical reactions such as the OER, R_P and R_S correspond to two or more charge transfer steps in the overall reaction. R_P and CPE_{dl} represent the total charge transfer resistance for the overall OER steps and the double-layer capacitance on the electrolyte-catalyst interface, respectively. The R_S -CPE_Φ loop is interpreted as the charge relaxation process related to surface intermediates. These circuit models have previously been utilized to analyze OER kinetics for the hydrous oxide layer in alkaline conditions. The total R_{CT} for hydrous oxide catalysts was expressed as the sum of R_P and R_S . The values for the Tafel slope were determined on the basis of the equation where b , i_0 and E are Tafel slope, exchange current and applied potential, respectively.

$$\log\left(\frac{1}{R_{CT}}\right) = \log\left(\frac{2.303 i_0}{b}\right) + \frac{E}{b}$$

Based on Tafel analysis through EIS, the rate-determining step was a one-electron transfer step that generated peroxy intermediate species on the hydrous oxide layer in alkaline conditions. However, circuit models B & C are limited to physical interpretations originating from CPEs.

As shown in Figure 2.8 b and c, CPEs, instead of pure capacitors, were applied as capacitive elements in circuit models B and C. CPEs are utilized as the frequency-

dependent capacitive elements in circuit modelling to fit experimental spectra perfectly. The impedance (Z) of the CPE is expressed as $Z = 1 / (Q(jw))^\alpha$, where w and α are the angular frequency and dispersion parameter ($0 \leq \alpha \leq 1$), respectively. When α is 0 or 1, the CPE is regarded as a pure resistor or pure capacitor, respectively. Values of α between zero and unity indicate a phase angle of $(\pi/2)\alpha$ for the line response in the impedance plane, hence the “constant phase” in CPE. CPEs are widely used in state-of-the-art impedance analysis, where arbitrary α parameters often result in apparent descriptions of the spectra. However, the dispersion parameter (α) for CPEs is randomly varied in the fitting process and the random change in α is strongly correlated with the other physical parameters obtained from fitting results. Thus, new capacitive elements with physical insight are needed to replace CPEs to extract well-defined kinetic parameters.

As shown in Figure 2.10, the fitting results for models B and C, the blue lines, almost perfectly described the experimental data. As shown in Figure 2.11, three values of the dispersion parameters for each CPE were determined for several thicknesses. As the thickness increased, the values of α were incoherently changed. Additionally, the values of α_{dl} for 300- and 500-nm thick films, 1.035 and 1.023, were larger than 1, although α is theoretically between 0 and 1. In this regard, the physical parameters obtained using CPEs did not universally explain the reaction kinetics for the OER in the catalyst films. Therefore, the weakness of models B and C is the ambiguous description in the fitting analysis caused by the arbitrary adjustment of frequency dispersion by CPEs.

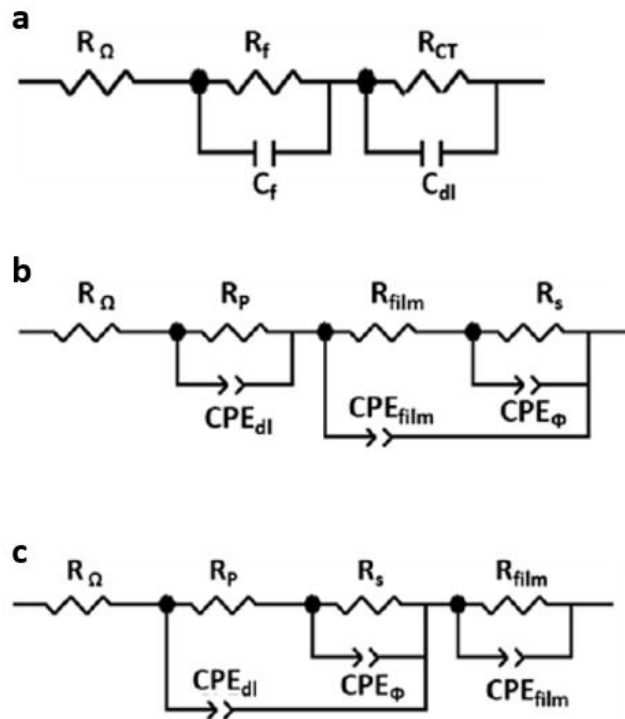


Figure 2.8. Previous circuit model for fitting analysis (a) simple circuit model; (b) the circuit model reported by Cahan and Chen group; (c) the circuit model reported by Lyon group

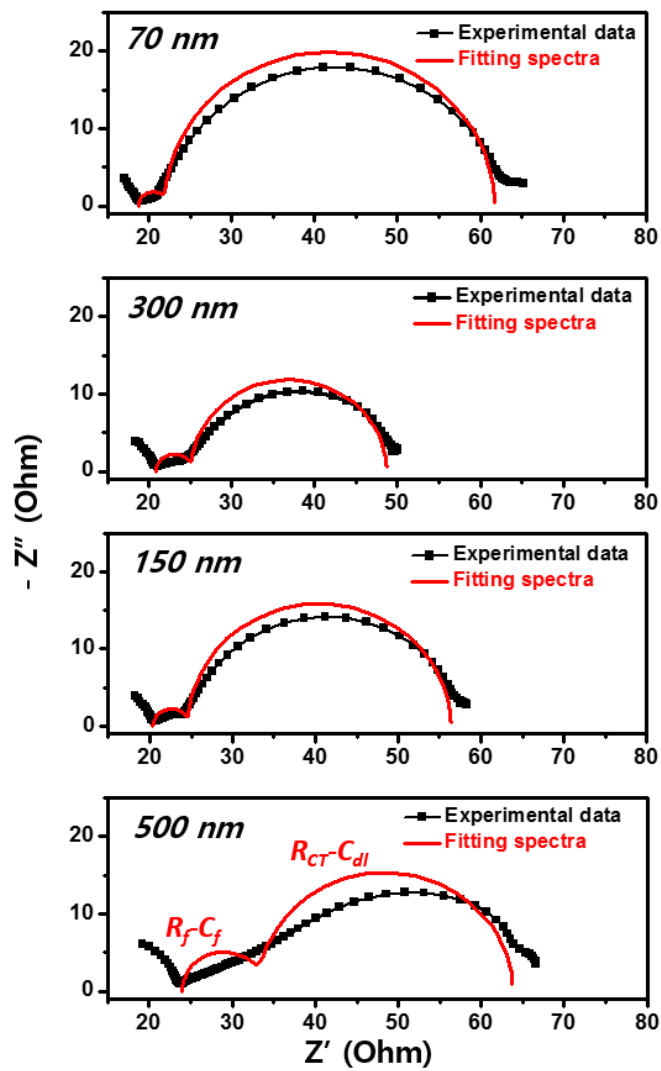


Figure 2.9. Nyquist plot of the fitting results for the 70, 150, 300 and 500 nm-thickness Mn_3O_4 NPs using the circuit model A.

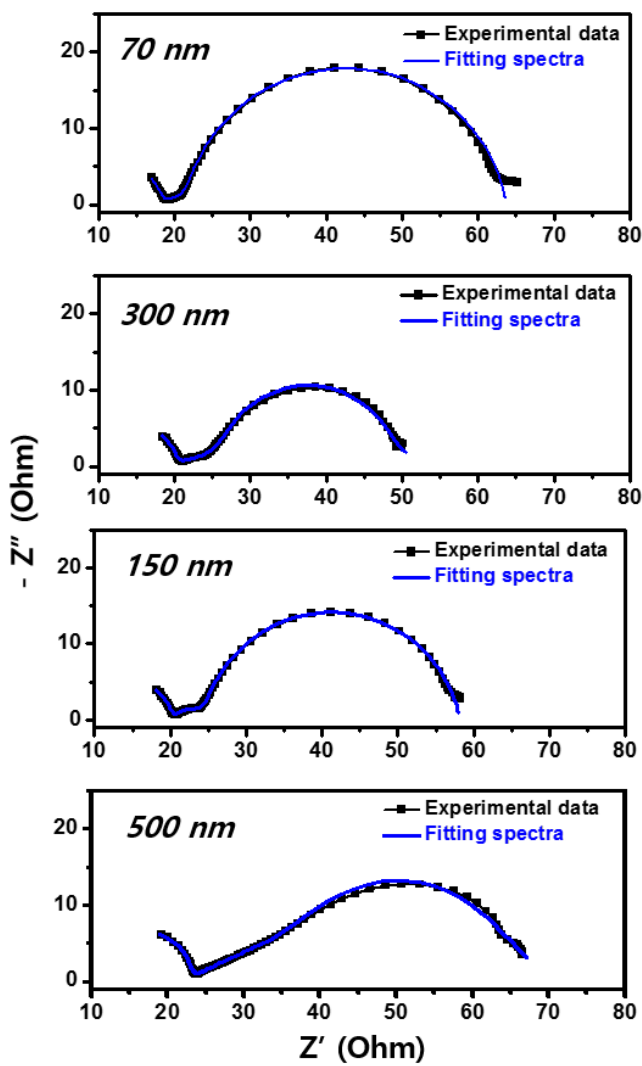


Figure 2.10. Nyquist plot of the fitting results for the 70, 150, 300 and 500 nm-thickness Mn_3O_4 NPs using the circuit model B and C.

Thickness	α_{film}	α_{Φ}	α_{dl}
20 nm	0.988	0.574	0.984
70 nm	0.568	0.891	0.826
150 nm	0.668	0.888	0.867
300 nm	0.976	0.240	1.035
500 nm	0.988	0.376	1.023

Figure 2.11. The fitting results of dispersion parameters (α_{film} , α_{Φ} , and α_{dl}) for each thickness from the previous circuit model C.

2.3.4. Our proposed circuit model to analyze Mn₃O₄ NPs films

A new circuit model was needed to extract kinetic parameters for various electrochemical processes, such as electron transport and surface catalysis, occurred concurrently in the Mn₃O₄ NPs film. The Mn₃O₄ NPs film was composed of an assembly of sub-10 nm sized spherical NPs. Thus, water molecules, electrolyte ions and protons, which participate in surface catalysis, permeated through the Mn₃O₄ NPs film. The NPs served as both active sites for OER catalysis and a path for electron transport from the active sites to the bottom FTO electrode. This situation is similar to porous TiO₂ NP layers in DSSCs, where electron transport is accompanied by a charge recombination reaction ($\text{h}^+ + \text{e}^-$). To separate the components of electron transport and charge recombination, transmission line models have previously been utilized in fitting analysis to extract various physical parameters for DSSCs.^[57-58] In transmission line models, parallel RC loops and serial resistive elements generally represent charge recombination reactions on the surface of the TiO₂ NP layer and electron transport processes, respectively.

We adopted the transmission line model to parameterize kinetic information for Mn₃O₄ NPs films (Figure 2.12). The parallel R_{int} and C_{int} loops indicated the active sites on the surface of Mn₃O₄ NPs. The resistive elements (R_{tr}) with serial connections between R_{int}-C_{int} loops described the electron transport process through assembled Mn₃O₄ NPs. Additionally, the Warburg element, depicted in the electrolyte region of our proposed circuit model, represented the diffusion of

electrolyte species, such as water molecules and phosphate ions. Thus, the circuit model clearly decoupled electron transport factors and surface catalysis from overall kinetic information, unlike other previous circuit models. As electrolyte molecules can be freely access the surface of NPs inside the film in high buffer concentration (0.5 M PBS), the diffusion-limitation for electrolyte molecules was not reflected in our circuit model. Thus, the resistive elements for diffusion were not included in our circuit model.

Furthermore, all capacitive elements in our circuit models were H-N capacitors instead of CPEs to extract physical parameters with accurate fitting analysis. Unlike ideal capacitors, H-N capacitance has frequency-dependent characteristics, as shown in the following equation where ω , τ , $C_{HN,\infty}$ and $C_{HN,0}$ are the frequency, relaxation time, capacitance at infinite frequency and capacity at steady state, respectively. Additionally, β and γ are dispersion parameters with values between 0 and 1.

$$C_{HN} = C_{HN,\infty} + \frac{C_{HN,0}-C_{HN,\infty}}{(1+(i\omega t)^\beta)^\gamma} \quad (0 \leq \beta, \gamma \leq 1)$$

The H-N function was originally devised to describe dielectric relaxation in organic materials. Subsequently, the H-N function was also applied to understand various dispersive phenomena in electrochemical processes in semiconductors, such as the Mott-Schottky response in TiO₂ photoanodes and current-constriction effects in the grain boundaries of polycrystalline Na₃Sc₂(PO₄)₂.^[75-76] The H-N function is also appropriate to demonstrate complicated electrochemical circumstances at the interface between the Mn₃O₄ NPs film and the electrolyte. At applying a potential,

the interface was polarized by electrolyte ions and surface-charged intermediates. A polarization delay was induced by the mobility of electrolyte ions and the formation rate of surface-charged intermediates. The frequency-dependent H-N function reflected this situation on the surface of Mn₃O₄ NPs during electrolysis. Thus, we designed our circuit model to incorporate H-N capacitors into the transmission line model.

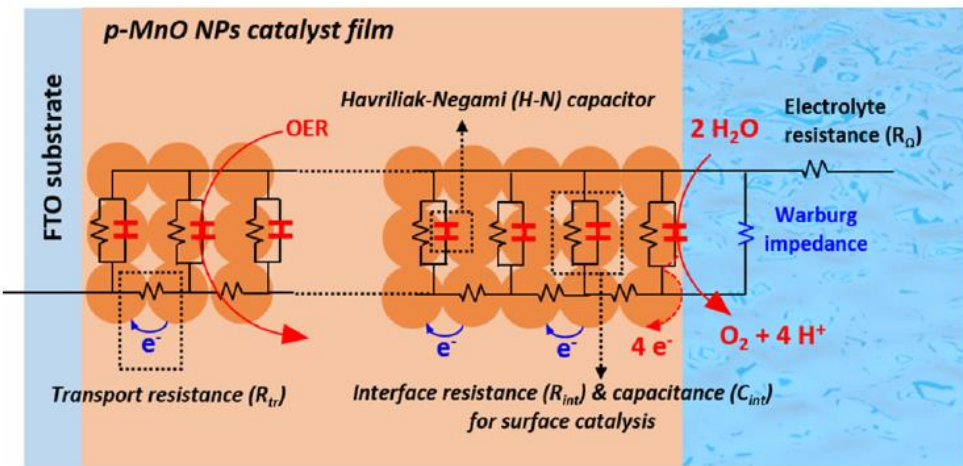


Figure 2.12. Our proposed circuit model for the impedance analysis of Mn_3O_4 NPs film. R_{tr} indicates resistance to electron transport in the Mn_3O_4 NPs. R_{int} and C_{int} in the RC loops, which describe surface catalysis, mean the interface resistance and capacitance, respectively. The red and blue capacitive elements in the circuit models are Havriliak–Negami capacitors and Warburg impedance elements, respectively.

We found that impedance spectra were successfully fitted with our proposed circuit model. At various thicknesses (70, 150, 300 and 500 nm) and applied potentials (1.2, 1.25, 1.3 and 1.35 V vs. NHE), the fixed beta (=0.7) and gamma (=1) exponents reasonably described all the experimental spectra (Figure 2.13). While the limitation of fitting with CPEs is the arbitrary change in α , which is strongly correlated with other physical parameters, the dispersion parameters (β and γ) of H-N capacitors are fixed at constant values, which support the validity of physical parameters obtained from the fitting procedure. By fitting, the interface resistance (R_{int}), electron transport resistance (R_{tr}) and interface capacitance (C_{int}) can be directly extracted, and with these values, several kinetic parameters, such as the reaction rate constant (k) and relaxation time constant (τ), can be further obtained. A detailed description of each parameter can be found in Table 1. R_{int} means the charge transfer resistance of oxygen evolving catalysis on the Mn_3O_4 NPs surface, which reflects faradaic process in overall reaction (Figure 2.14). R_{tr} indicates the resistance of electron transport from the surface of the catalyst film to the bottom FTO electrodes (Figure 2.15). Additionally, C_{int} means the capacitance induced by electrolyte ions and surface-charged intermediates (Figure 2.16). The R_{tr} and C_{int} are related to non-faradaic process. τ means the relaxation time required to generate a charged intermediate on the Mn_3O_4 NPs. Furthermore, k is the reaction rate constant for oxygen evolving catalysis on the catalyst surface and can be regarded as an indicator of intrinsic efficiency, which is related to the turnover frequency (TOF).

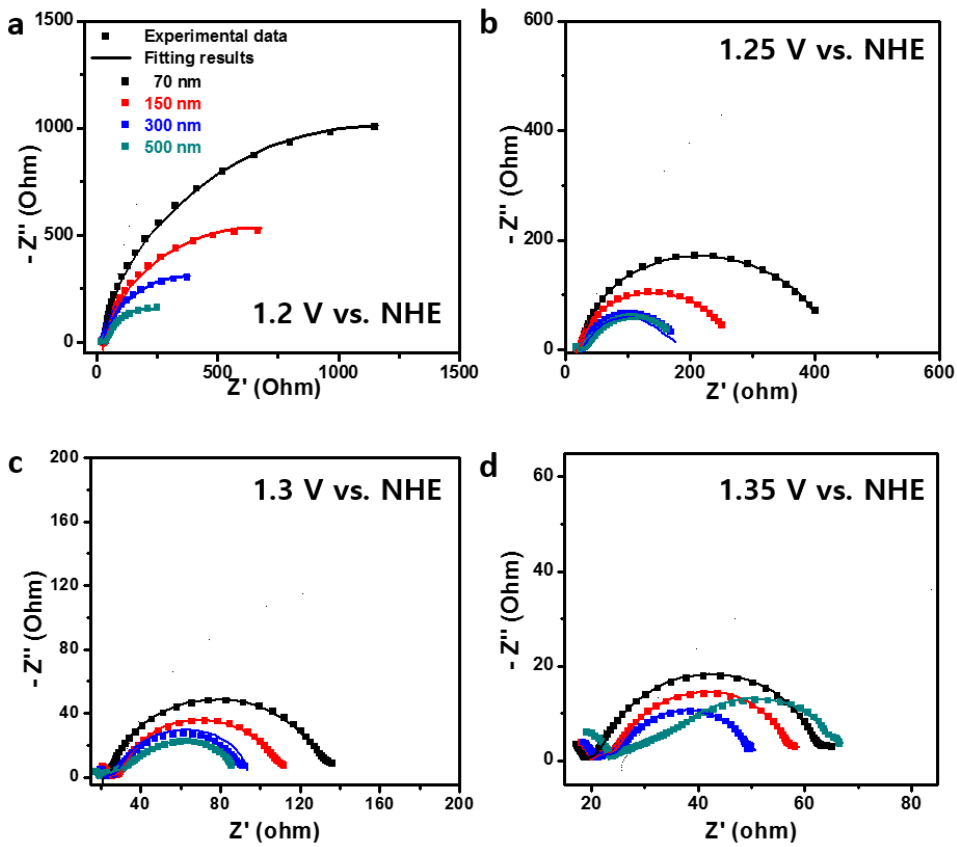


Figure 2.13. Nyquist plots for several thicknesses (70, 150, 300, and 500 nm) of Mn_3O_4 NP films at (a) 1.2 V, (b) 1.25 V, (c) 1.3 V, and (d) 1.35 V vs NHE. Square points indicate the experimental spectra for Mn_3O_4 NPs, and lines represent the fitting results obtained by our proposed circuit model. The black, red, blue, and dark cyan spectra indicate data for 70, 150, 300, and 500 nm thicknesses, respectively.

2.3.5. Fitting results for our proposed circuit model

2.3.5.1 Interface resistance (R_{int}) and transport resistance (R_{tr})

Interface resistance (R_{int}) can provide information about the surface electrochemical reaction on the Mn_3O_4 NPs catalyst (Figure 2.14). This physical meaning of R_{int} is similar to that of the previously discussed parameter R_{CT} in circuit model A but very different in that transport resistance was separately parameterized in our model. Therefore, the measured R_{int} was higher than the R_{CT} fitted with circuit model A. More importantly, a clear dependency on the thickness and applied potential can be observed, as shown in Figure 5b. As the film thickness increased from 70 nm to 500 nm, R_{int} decreased more distinctly at lower potentials. The thickness-dependent change was caused by the increase in electrochemically active area with increased thickness of the NP-assembled film, although the geometric area did not vary with thickness. As the applied potential increased from 1.2 to 1.35 V vs. NHE, log values for R_{int} linearly decreased at all thicknesses. The potential-dependent change of R_{int} can be explained by the Butler-Volmer equation, which shows that the catalytic current density has an exponential relationship with the applied potential. The thickness-dependence was more distinctly at lower potential due to the effect of Mn redox process. The faradaic current density was almost mainly caused by oxygen evolving catalysis at higher potential. But, at lower potential, the current density from oxygen evolving catalysis decreased and the contribution of Mn redox process cannot be negligible. For Mn redox process, all

Mn species can participate, whereas only small ratio of Mn species was associated in the surface catalysis. Thus, the thickness-dependent decrease of R_{int} became more noticeably at lower potential.

Electron transport resistance (R_{tr}) is a meaningful parameter in our circuit model in terms of identifying authentic electron transport characteristics in electrocatalyst films (Figure 2.15). As shown in Figure 5c, R_{tr} showed a clear dependence on thickness at all potentials (1.2, 1.25, 1.3 and 1.35 V vs. NHE). R_{tr} gradually increased as the film thickness increased from 70 to 500 nm. At 1.35 V vs. NHE, R_{tr} was measured as 4.79, 9.07, 10.80 and 45.7 Ω at 70-, 150-, 300- and 500-nm thicknesses, respectively. The thickness dependence was explained by the increase in the electron transport distance from the surface of the catalyst film to the bottom FTO electrodes.

From the comparison between R_{tr} and R_{int} , we determined which process acted as the rate-determining factor for the overall efficiency of the Mn_3O_4 NPs film (Figure 2.14, 2.15). At a low potential of 1.2 V vs. NHE, R_{int} ($10^{2.75\sim3.41} \Omega$) was more significant than R_{tr} ($10^{0.61\sim1.21} \Omega$). This difference indicated that electron transport occurred more rapidly than surface catalysis at low potential. Thus, the overall catalytic performance at low potential was mainly determined by surface catalysis; this relationship is identified as “surface-catalysis-limited kinetics ($R_{int} >> R_{tr}$)”. As applying potential increases, the gap between R_{tr} and R_{int} decreased due to the linear decrease in R_{int} . At 1.35 V vs. NHE, the ranges of R_{int} and R_{tr} were similar ($R_{int} = 10^{1.41\sim1.64} \Omega$ and $R_{tr} = 10^{0.61\sim1.65} \Omega$). This similarity indicated that electron transport became the dominant process in determining the overall efficiency of the Mn_3O_4 NPs

film at high potential. For this reason, OER activity decreased at thicknesses greater than 300 nm at 1.35 V vs. NHE due to electron transport restriction (Figure 2.5).

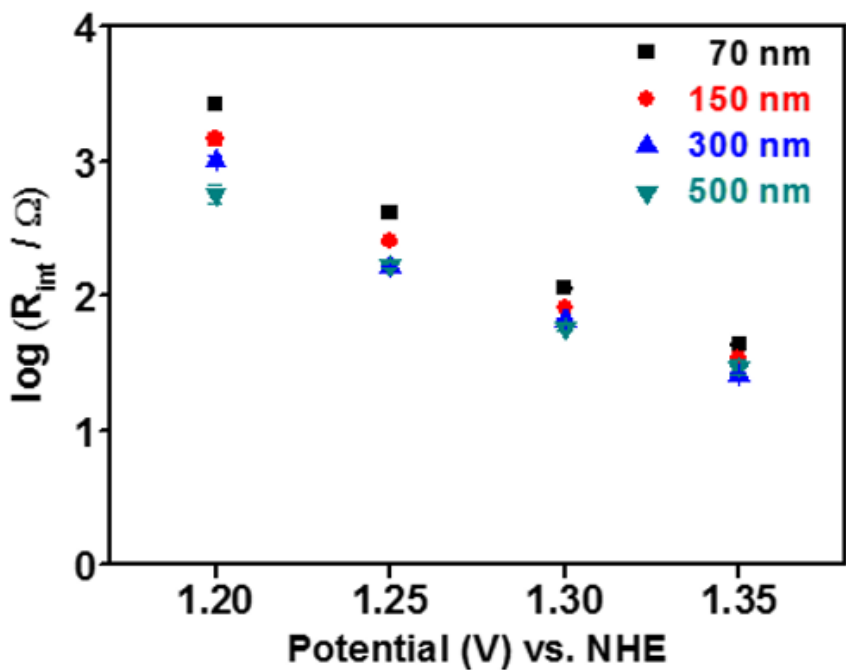


Figure 2.14. Interface resistance (R_{int}) for Mn_3O_4 NPs film with various thicknesses (70 nm, 150 nm, 300 nm and 500 nm) at various applying potential (1.2, 1.25, 1.3 and 1.35 V vs. NHE) from fitting analysis with our proposed circuit model.

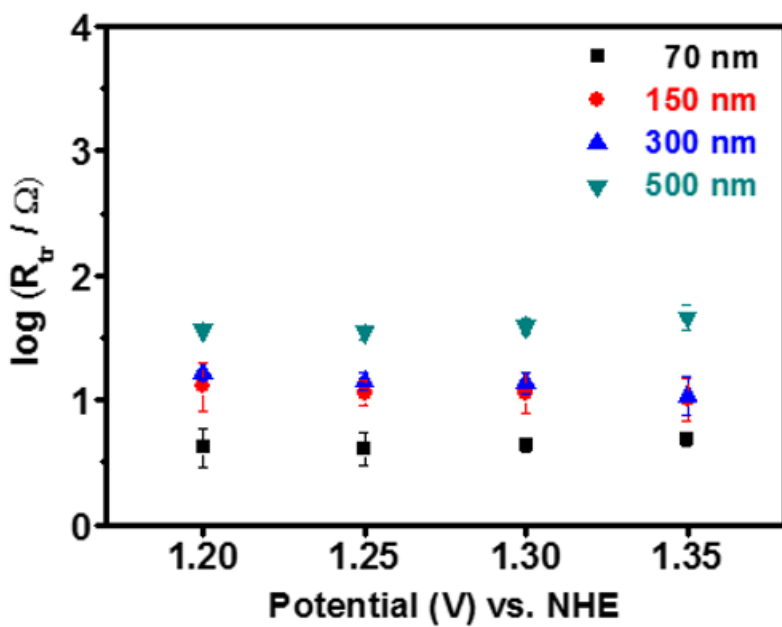


Figure 2.15. Transport resistance (R_{tr}) for Mn_3O_4 NPs film with various thicknesses (70 nm, 150 nm, 300 nm and 500 nm) at various applying potential (1.2, 1.25, 1.3 and 1.35 V vs. NHE) from fitting analysis with our proposed circuit model.

2.3.5.2 Interface capacitance (C_{int})

Interface capacitance (C_{int}) between the Mn_3O_4 NPs and electrolyte was induced by electrolyte ions and surface-charged intermediates during catalysis. As shown in Figure 2.16, C_{int} remained constant with changing potential at each film thickness. In contrast, a clear dependence on thickness was observed at all potentials (1.2, 1.25, 1.3 and 1.35 V vs. NHE). As the film thickness increased from 70 to 500 nm, C_{int} gradually increased from ~0.1 to ~10 mF. At 1.35 V vs. NHE, where the OER progressed briskly, C_{int} values for 70-, 150-, 300- and 500-nm-thick films were measured as 0.43, 0.82, 1.74 and 2.35 mF, respectively. For a 300-nm thickness, the mass capacitance (F/g) was calculated from the loading mass (~0.24 mg) as 8.97 F/g. The mass capacitance of the Mn_3O_4 NPs film was smaller than the mass capacitance of Mn oxide-based supercapacitors (> 100 F/g) because, unlike the situation with supercapacitors, charge did not accumulate on the surface of the Mn_3O_4 NPs due to OER catalysis (Figure 2.17).^[77-81] Additionally, the thickness-dependent change was caused by the increase in the electrochemically active area with film thickness for the nanoparticle-assembled catalysts.

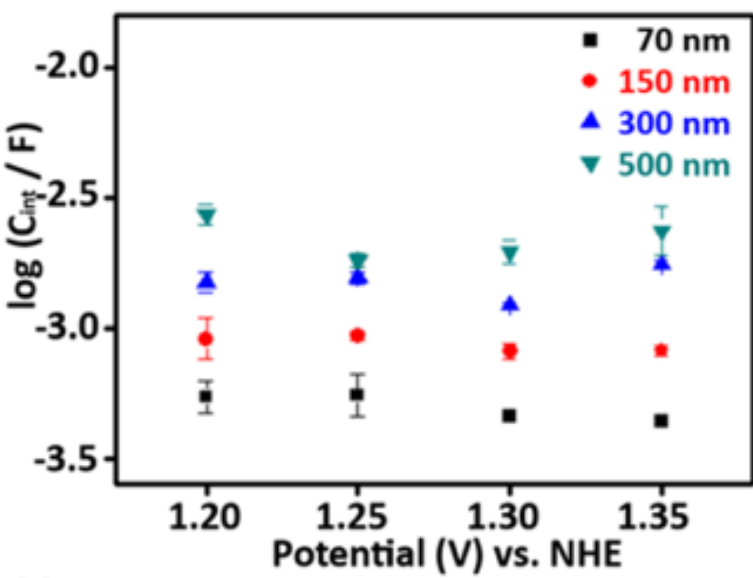


Figure 2.16. Interface capacitance (C_{int}) for Mn_3O_4 NPs film with various thicknesses (70 nm, 150 nm, 300 nm and 500 nm) at various applying potential (1.2, 1.25, 1.3 and 1.35 V vs. NHE) from fitting analysis with our proposed circuit model.

Nature of Mn-oxide	Preparation method	Mass of electroactive materials (mg/cm ²)	Electrolyte	Capacitance (F/g)
p-MnO NPs	Spin-coating	0.24	0.5 M PBS	8.97
Mn ₃ O ₄ film	Electrostatic spray deposition	0.116	0.1 M Na ₂ SO ₄	150
Mn ₃ O ₄ film	Chemical bath deposition	0.57	1 M Na ₂ SO ₄	193
MwCNT/Mn ₃ O ₄ film	Dip-casting method	10.1	0.5 M Na ₂ SO ₄	143
Graphene/Mn ₃ O ₄ powder	Hydrothermal	2.0	1 M Na ₂ SO ₄	114
	Precipitation from MnO ₂ organosol	0.75	1 M Na ₂ SO ₄	175

Figure 2.17. Summary for reported capacitance for several Mn-oxide electrodes.^[77-81]

2.3.5.3 Measurement of intrinsic resistance (R_{air}) for Mn_3O_4 NPs under ambient condition

We further measured the intrinsic resistance (R_{air}) of the Mn_3O_4 NPs film under ambient conditions at room temperature for comparison with R_{tr} under OER conditions. As shown in Fig. 6a, we performed current-voltage (I-V) measurements from -1 to +1 V in a planar two-electrode configuration with gold contacts. The conductivity (σ_{air}) for Mn_3O_4 NPs in ambient condition was measured as $6.40 \times 10^{-9} S \cdot cm^{-1}$ by the equation, $\sigma = L/A \cdot R$, where L, A and R are the electrode distance, electrode area and resistance (the slope of the I-V curve), respectively (Figure 2.18). The σ_{OER} was calculated as $2.78 \times 10^{-6} S \cdot cm^{-1}$ by $\sigma = L/A \cdot R$, where L, A and R are 300 nm, 1 cm^2 and 10.80 Ω , respectively ($R_{tr, 300\text{ nm}} = 10.80 \Omega$ at 1.35 V vs. NHE, Figure 5a). Additionally, to confirm the effect of interfacial resistance for different substrates (Au and FTO), EIS analysis was performed for Mn_3O_4 NPs on Au/FTO electrode fabricated by sputtering Au. The conductivity calculated from R_{tr} on Au/FTO substrates was also larger than σ_{air} . Thus, the effect of substrates (Au or FTO) on R_{tr} can be negligible to compare σ_{OER} and σ_{air} (Figure 2.19). This difference ($\sigma_{OER} > \sigma_{air}$) indirectly supported that surface catalysis, electrolyte species or protons could accelerate the electron transport process through the Mn_3O_4 NPs film during the OER.

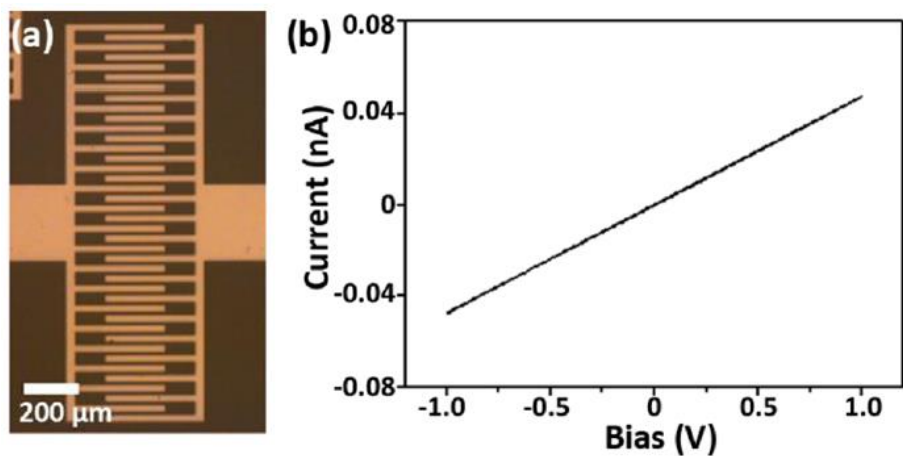


Figure 2.18. Measurement of intrinsic resistance in air. (a) Planar twoelectrode configuration with gold electrodes for DC measurement; and (b) I–V curves of MnO NPs in ambient conditions on planar gold electrodes.

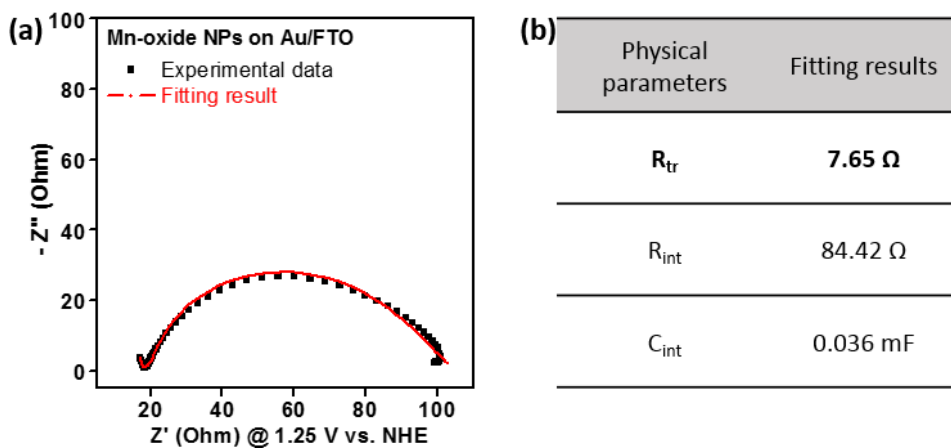


Figure 2.19. (a) Nyquist plot for 150 nm-thickness Mn-oxide NPs film on Au/FTO substrates at 1.25 V vs. NHE in 0.5 M phosphate buffer solution. The black dots and red line indicated experimental data and fitting result using our proposed circuit model. (b) The values for physical parameters (R_{tr} , R_{int} and C_{int}) from fitting with our circuit model.

2.3.5.4 Proton involvement in electro transport during catalysis

To examine proton involvement in the electron transport process during the OER, we conducted an H/D isotope experiment through impedance analysis. We compared transport resistance in H_2O and D_2O electrolyte at 1.35 V vs. NHE, where the potential was high enough to promote the OER (Figure 2.22). We observed that $R_{\text{tr},\text{D}2\text{O}}$ was larger than $R_{\text{tr},\text{H}2\text{O}}$ at all thicknesses. At 1.35 V vs. NHE, the transport resistance in the H_2O electrolyte ($R_{\text{tr},\text{H}2\text{O}}$) was measured as 4.79, 9.07, 10.80 and 45.7 Ω at 70-, 150-, 300- and 500-nm thicknesses, respectively. The transport resistance in the D_2O electrolyte ($R_{\text{tr},\text{D}2\text{O}}$) was 30.62, 31.19, 32.73 and 48.38 Ω at 70-, 150-, 300- and 500-nm thicknesses, respectively. The increase of R_{tr} for all thickness directly indicated that protons were involved not only in oxygen evolving catalysis on the surface of Mn_3O_4 NPs but also in the electron transport mechanism from the surface active site to the bottom electrodes. The proton involvement implies that electrons were not conducted through the inner part of nanoparticles but were transported on their surface during catalysis.

Previous studies have examined whether protons are involved in electron transport in catalyst films during the OER. The Frei group revealed that Co(IV)=O intermediate species moved thermodynamically favorably on the Co_3O_4 (001) surface via proton-electron hopping.^[69] The facile movement of Co(IV)=O easily generated an active structure to form O-O bonding and accelerate oxygen evolving catalysis. However, it was still difficult to obtain experimental evidence for proton

involvement in electron transport during the OER. Interestingly, the observed H/D isotope effect in R_{tr} indicated that protons accelerate electron transport on the surface of Mn_3O_4 NPs by proton-electron hopping. Additionally, we previously captured $Mn(IV)=O$ species as reaction intermediates based on *in-situ* spectroscopic analysis.^[50] Therefore, it was expected that $Mn(IV)=O$ species migrated on the surface of Mn_3O_4 NPs to form O-O bonds by proton-electron hopping in oxygen evolving catalysis.

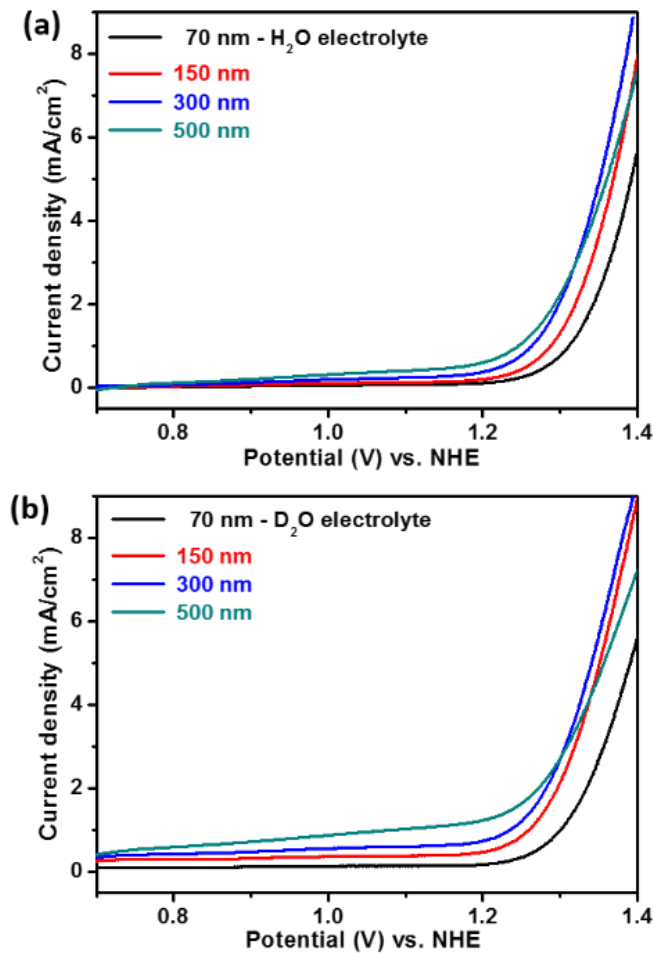


Figure 2.20. Polarization-corrected cyclic voltammetry curves from 0.7 V to 1.4 V vs. NHE for Mn₃O₄ NPs film of various thicknesses (70, 150, 300 and 500 nm) at 0.5 M phosphate buffer solution under pH 7. (a) H₂O electrolyte (b) D₂O electrolyte

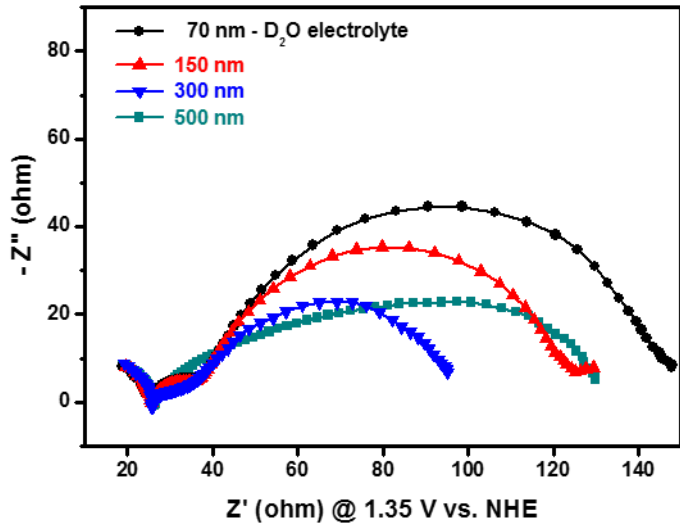


Figure 2.21. Nyquist plots for several thickness (70, 150, 300 and 500 nm) of Mn₃O₄ NPs film at 1.35 V vs. NHE in D₂O electrolyte. The black, red, blue and dark cyan spectra were for 70, 150, 300 and 500 nm-thickness, respectively

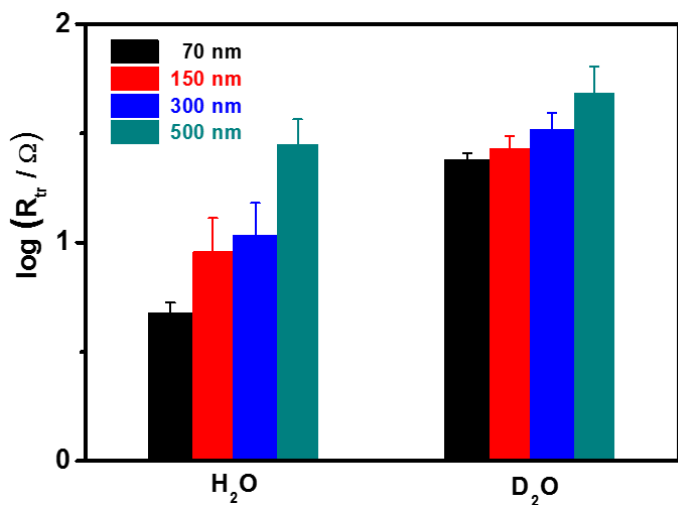


Figure 2.22. Comparison between transport resistance in H_2O and D_2O electrolyte

2.3.5.5 Relaxation time constant (τ) for OER kinetics on Mn₃O₄ NPs

As shown in Figure 2.23, the relaxation time constant (τ) was obtained from the transport resistance and interface capacitance ($\tau = R_{tr} \cdot C_{Int}$). This physical parameter indicated the relaxation time for electron transport coupled with the generation of surface-charged intermediates, such as Mn(IV)=O species. The relaxation time constant showed a clear thickness dependence at each potential. At 1.35 V vs. NHE, τ was measured as 2.09, 8.26, 18.84 and 107.6 msec for the 70-, 150-, 300- and 500-nm-thick films, respectively. The thickness-dependent change indicated that the relaxation time constant reflected electron transport restriction, which contributed to the overall catalytic efficiency. The decrease in catalytic efficiency at thicknesses greater than the optimal value was caused by the increase in the relaxation time constant. In this regard, the relaxation time constant could be a meaningful parameter describing the electron transport characteristics of film-type electrocatalysts.

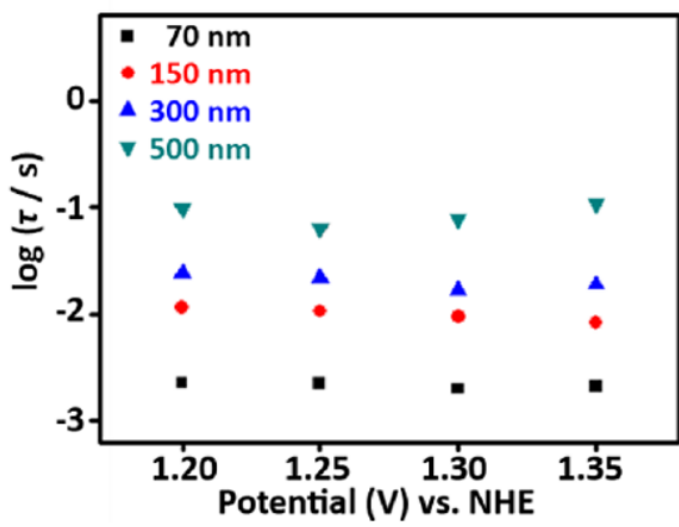


Figure 2.23. Relaxation time constant for the OER kinetics of Mn_3O_4 NPs catalyst film

2.3.5.6 Reaction rate constant (k) for surface catalysis on Mn_3O_4 NPs

Furthermore, the OER kinetics for Mn_3O_4 NPs were further elucidated by the reaction rate constant (k) from impedance analysis (Figure 2.24). The value of k reflected OER kinetics on the surface of Mn_3O_4 NPs. We previously investigated the unique water-oxidizing mechanism of Mn_3O_4 NPs by combining electrokinetic studies and *in-situ* spectroscopic analyses.^[50] The 1 H^+ and 1 e^- coupled transfer process occurred prior to the rate-determining step, and Mn(IV)=O species were generated as reaction intermediates on the Mn_3O_4 NP surface. In the proposed mechanism, O-O bond formation on Mn(IV)=O species was a rate-determining step for the OER. The k value obtained from fitting analysis corresponded to the rate-determining step that generated O-O bonding with Mn(IV)=O species.

As shown in Figure 2.24, the log-transformed values for the reaction rate constant (k) linearly increased with overpotential (η). The linear dependence on overpotential was explained by the k - η relationship ($k = k_0 \cdot \exp(\alpha F \eta / RT)$), where α , F , R and T are the transfer coefficient, faradaic constant, ideal gas constant and temperature, respectively. Thus, α could be estimated from the slopes for the η -log (k) graph. The transfer coefficient for the 70-nm thickness was calculated as 0.74 from the k - η relationship. In a previous study, we also measured the transfer coefficient via Tafel analysis. The Tafel slope (b) is inversely related to α ($b = 2.3 RT/\alpha F$). Thus, α was calculated as 0.72 from the Tafel slope (82.6 mV/dec) for the 70-nm thickness.^[50] The analogous values of the transfer coefficient obtained from

the k - η relationship and the value of b support the validity of the k value obtained from impedance analysis.

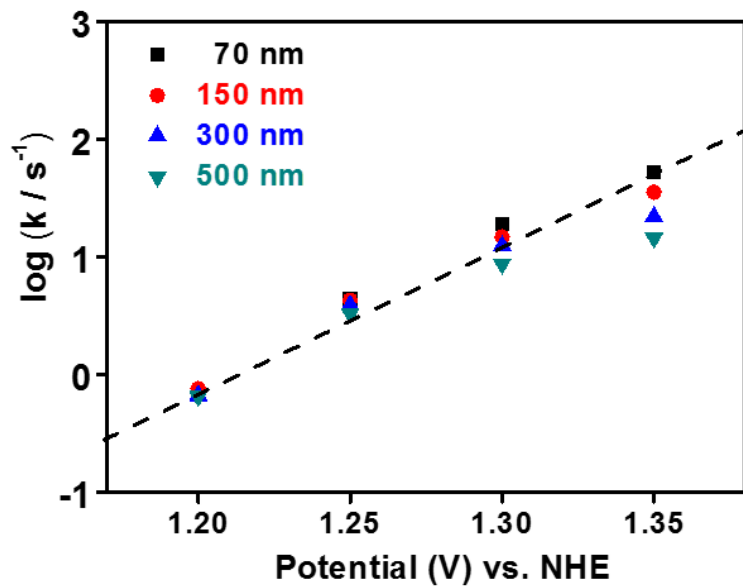


Figure 2.24. Reaction rate constant (k) for the OER kinetics of Mn_3O_4 NPs catalyst film

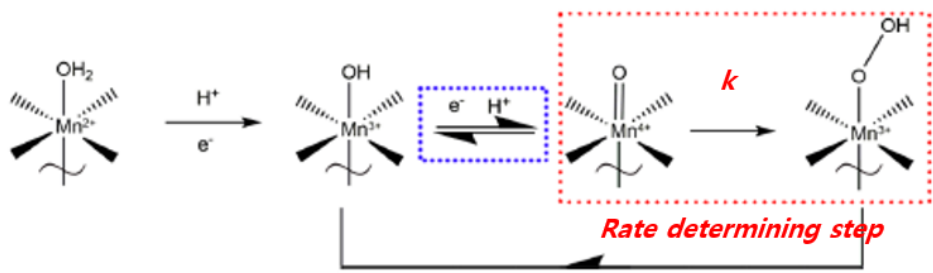


Figure 2.25. Scheme of reaction mechanism for OER on the Mn_3O_4 NPs and reaction-determining step for O-O bond formation^[50]

2.3.5.7 Methodology to estimate the ratio of active sites on Mn₃O₄ NPs

The reaction rate constant (k) has a close relationship with the TOF for film-type electrocatalysts. TOF can generally be calculated from the following equation.

$$\text{TOF} = \frac{j}{4F \cdot (\# \text{ of active sites})}$$

For homogeneous catalysis, the number of active sites is estimated by the concentration of the dispersed catalyst. However, for heterogeneous catalysis, the evaluation of the number of active sites requires additional assumptions. For electrodeposited catalysts, the number of active sites is estimated by the charge amount passed during film deposition with the assumption that all deposited metal sites serve as active sites.^[21, 82] Additionally, the number of active sites is estimated by measuring the electrochemically active surface area (ECSA). We performed ECSA analysis to calculate TOF values for Mn₃O₄ NPs. ECSA is estimated by dividing double-layer capacitance (C_{dl}) by the specific capacitance (C_s). C_{dl} can be estimated from the following equation, where i_c and ν are the charging current and scan rate, respectively (Figure 2.26). This methodology requires the assumption that the charging current (i_c) in the nonfaradaic region is totally caused by double-layer charging.

$$\text{ECSA} = \frac{C_{DL}}{C_s} \quad i_c = \nu C_{DL}$$

For 300 nm-thickness, the double-layer capacitance (C_{DL}= 5.91 mF) was determined by the average of the absolute values of the slope of the linear fits to the data (Figure 7b). The ratio of ECSA to geometric area was calculated as 147.8 by double layer

capacitance (C_{DL}) divided by specific capacitance ($C_s = 0.04$ mF). Then, the value of TOF at 1.35 V vs. NHE was calculated as 0.052 s^{-1} with the assumption that all Mn sites participated in catalysis. The number of active sites for 300 nm-thickness Mn_3O_4 NPs film was calculated with the assumption that all Mn atoms on the surface of nanoparticles serve as the active sites. The number of active sites for 300 nm-thickness Mn_3O_4 NPs film was calculated by the following equation with assumption that the surface of Mn_3O_4 NPs was (100) facet. The crystal structure and lattice parameter for Mn_3O_4 were face-centered cubic structure and $4.43 \times 10^{-8}\text{ cm}$.

(The number of active sites)

$$\begin{aligned} &= (ECSA) \times (\text{the moles of Mn atoms / cm}^2) \\ &= (147.8) \times \left(\frac{2}{(4.43 \times 10^{-8})^2 \times (6.02 \times 10^{23})} \right) \\ &= 2.502 \times 10^{-7} \text{ moles / cm}^2 \end{aligned}$$

TOF at 1.35 V vs. NHE can be calculated by calculated by the following equation based on the above values.

$$\begin{aligned} (\text{TOF}) &= \frac{(\text{current density at } 1.35\text{ V vs. NHE})}{4 \cdot F \cdot (\text{the number of active sites})} \\ &= \frac{0.00496\text{ A/cm}^2}{4 \cdot (96485\text{ A} \cdot \text{s/mol}) \cdot (2.502 \times 10^{-7} \text{ moles / cm}^2)} = 0.052\text{ s}^{-1} \end{aligned}$$

As shown in Figure 2.24, the reaction rate constant for the 300-nm thickness at 1.35 V vs. NHE was 22.1 s^{-1} . The only small ratio (~ 0.0016) of k to TOF was caused by the excessive assumption in the TOF calculation that all Mn sites on the surface of

the catalyst film serve as active sites for the OER. The ratio of k to TOF indicated that only a small amount of Mn sites participated in the catalytic cycle and generated Mn(IV)=O species on the surface of Mn_3O_4 NPs during catalysis. The ratio is similar to the reported value (~0.001) for Co-Pt films, confirming the validity of our kinetic analysis. The high OER activity of Mn_3O_4 NPs with a small ratio of Mn(IV)=O species could be attributed to the facile movement of Mn(IV)=O species with a proton-electron hopping process.

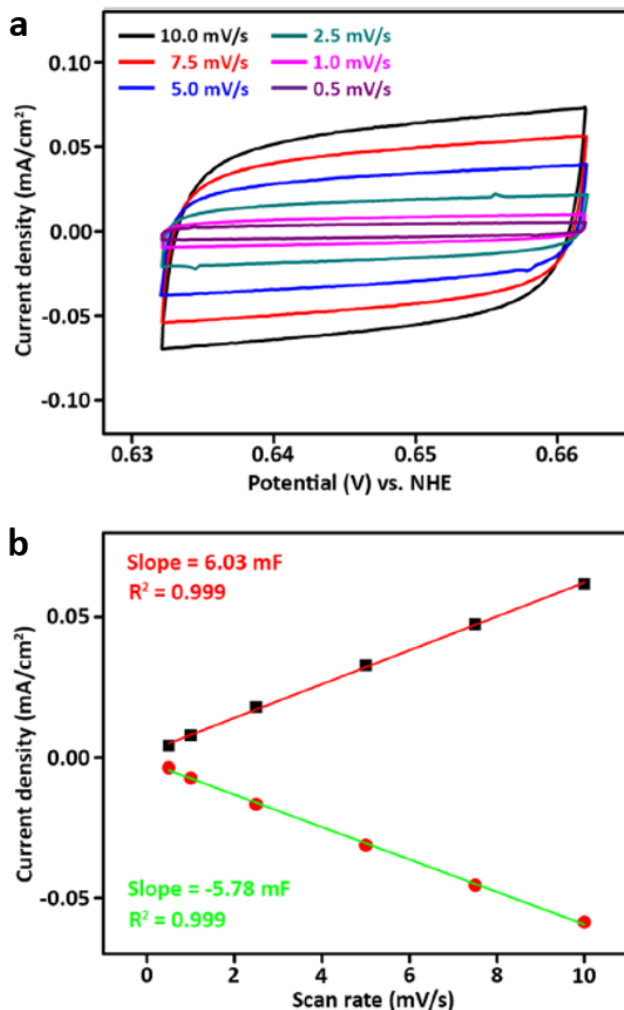


Figure 2.26. Double-layer capacitance measurements for determining electrochemically active surface area for 300 nm-thickness Mn_3O_4 NPs film. (a) Cyclic voltammetry was measured in a non-Faradaic region at the following scan rates: 0.5 (purple line), 1 (magenta line), 2.5 (dark cyan line), 5 (blue line), 7.5 (red line), and 10 (black line) mV/s . (b) The cathodic (■) and anodic (●) charging current density measured at 0.645 V (open-circuit potential) are plotted as a function of scan rates.

2.3.5.8 Measurement of reaction rate constant (k) for Co-Pi catalyst

The estimation of reaction rate constant for heterogeneous electrocatalysts is challenging issue because it is difficult to measure the number of active sites. In this regard, previous studies attempted to measure reaction rate constant (k) for Co-Pi catalyst by various experimental methodologies. Co-Pi is well-known amorphous cobalt oxide-based electrocatalyst for OER, which exhibits benign catalytic activity in neutral condition. In 2010, Nocera group reported that reaction rate constant (k) for OER was measured as $> 0.002 \text{ s}^{-1}$ at 1.23 V vs. NHE by geometric assumption.^[21] However, the value was underestimated due to assumption that all cobalt sites on the catalyst surface were participated in OER catalysis. Then, Bard group measured reaction rate constant (k) for Co-Pi by surface interrogation scanning electrochemical microscopy (SI-SECM).^[83] For SI-SECM experiment, surface active site density was evaluated by amperometric titration using redox mediators, $\text{FcDM}^+/\text{IrCl}_6^{2-}$. The value was measured as 3.2 s^{-1} at 1.23 V vs. NHE.

To confirm validity for reaction rate constant (k) from impedance analysis, we conducted EIS analysis for Co-Pi heterogeneous catalysts at various applying potential, 1.2, 1.25, 1.3 and 1.35 V vs. NHE. Fitting analysis was performed to fit impedance spectra using our proposed circuit model. Reaction rate constant (k) was measured as 2.82 s^{-1} and 13.5 s^{-1} at 1.25 and 1.35 V vs. NHE, respectively. The values of reaction rate constant (k) for Co-Pi was smaller than those for our Mn_3O_4 NPs at each applying potential. It indicated that the Mn_3O_4 NPs showed superior catalytic

activity for OER compared to Co-Pi catalysts. Furthermore, the value of k at 1.25 V, which was estimated by fitting impedance spectra with our circuit model, was similar with that at 1.23 V vs.NHE, which was estimated by SI-SECM. It indicated that the methodology to calculate k by impedance analysis was valid for film-type OER electrocatalysts.

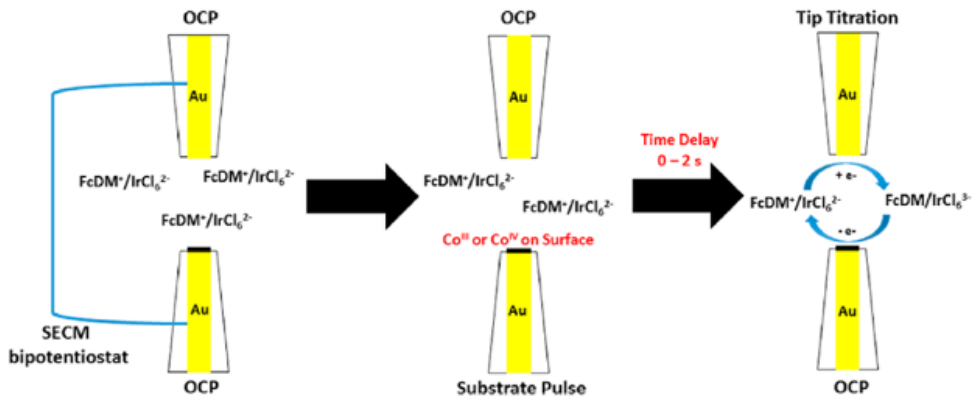


Figure 2.27. Schematic illustration for scanning electrochemical microscopy (SI-SECM) for Co-Pi catalysts^[83]

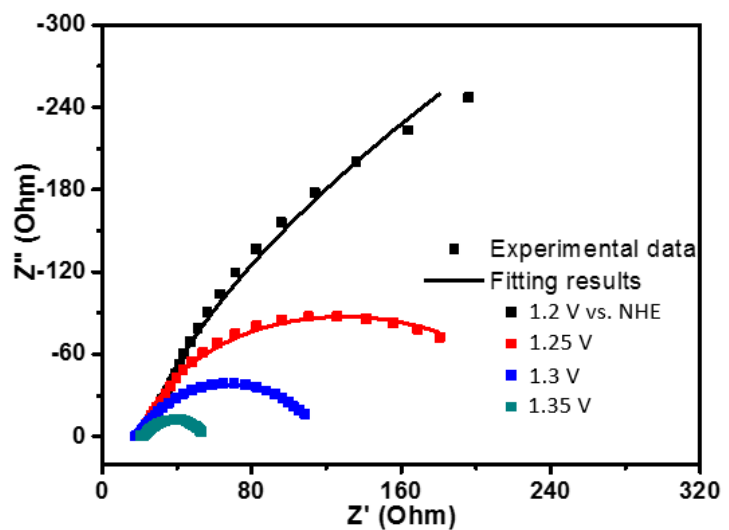


Figure 2.28. Nyquist plot for Co-Pi at various applying potential (1.2 V, 1.25 V, 1.3 V and 1.35 V) during OER catalysis

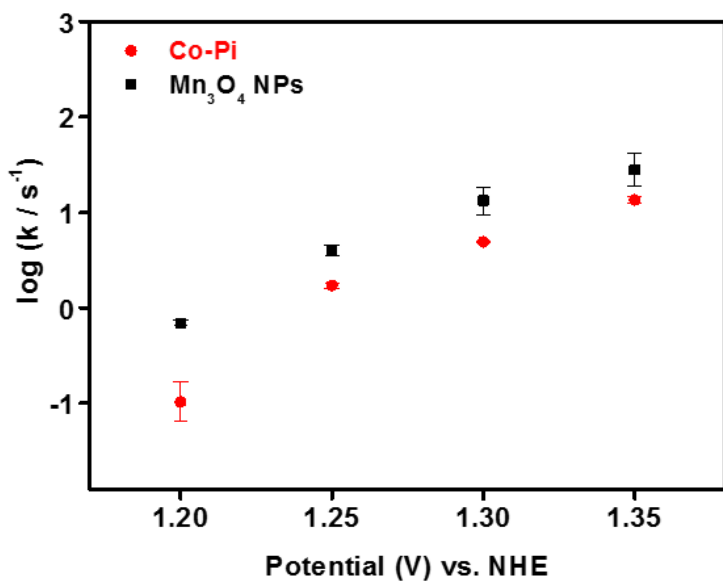


Figure 2.29. Reaction rate constant (k) for Co-Pi catalyst and Mn_3O_4 NPs at various applying potential (1.2, 1.25, 1.3 and 1.35 V vs. NHE)

2.4. Concluding remarks

We performed impedance analysis for a Mn_3O_4 NPs film to extract reasonable physical parameters that provide new insight into OER kinetics. For a well-defined fitting process, we established a new circuit model with Havriliak-Negami capacitors to solve the limitations of CPEs. Using the proposed circuit model, we successfully parameterized the kinetics of the OER catalyzed by Mn_3O_4 NPs films, yielding the parameters R_{tr} , R_{int} , C_{int} , τ , and k . Specifically, the overall OER performance was determined by the competition between surface catalysis and electron transport in terms of the thickness dependence of R_{int} and R_{tr} . Additionally, based on the quantitative comparison of transport resistance between the H and D isotope electrolytes, we can conclude that protons are involved in the electron transport process across the nanoparticle film, which directly proves the ongoing hypothesis of the oxo-hopping mechanism. Furthermore, from the correlation between k and TOF, the ratio (~ 0.001) of total Mn sites on the surface to the actual number of active sites can be evaluated. We believe that this mechanistic investigation using EIS analysis with our circuit model could be an effective platform to investigate comprehensive electrochemical processes in general film-type electrocatalysts.

Chapter 3. Complex capacitance analysis for charging process on Mn₃O₄ electrocatalyst during OER catalysis

3.1. Introduction

Electrochemical water splitting has been regarded as an attractive approach to produce renewable hydrogen energy without undesirable byproducts.^[9,84] Substantial research efforts have been devoted for practical application of water electrolysis technology to obtain environment-friendly hydrogen energy. However, sluggish kinetic for the anodic half reaction, oxygen evolving reaction (OER), is major obstacle to improve overall performance of water electrolysis.^[9] The large overpotential for OER was caused by its complicated four electron transfer steps and O-O bond formation with substantial activation energy. For decades, numerous OER electrocatalysts have been developed to reduce its overpotential. Noble-metal-based catalysts, such as IrO_x and RuO₂, generally showed high efficiency, but their high cost and scarcity were regarded as difficulty for practical application. In this regard, 3d transition-metal-based catalysts were extensively studied to achieve superb activity comparable with noble-metal-based catalyst.^[10]

Copious researches, including *in situ* spectroscopic analyses and computational studies, have been attempted to elucidate OER mechanism for establishment of design rule for highly efficient electrocatalysts.^[21, 85] The electronic structure and bonding characteristic for the catalyst surface were analyzed via *in situ* X-ray absorption spectroscopy (XAS) and Raman analysis.^[54,86-88] Also, reaction intermediates which generated on the surface were detected via *in situ* FT-IR analysis.^[13] Combining these *in situ* spectroscopic studies, computational studies explained energetically favorable pathways and thermodynamically stable structure of intermediate species for electrochemical water oxidation. Specifically, O-O bond formation, generally regarded as rate-determining step, remains challenging issue for the OER electrocatalysts. The possible mechanisms for O-O bond formation were nucleophilic attack of water molecules and radical coupling of adjacent metal-oxo species. Based on the mechanistic studies, facilitating O-O bond formation is effective strategy to enhance catalytic performance for OER electrocatalysts.

Structure-activity correlation for OER electrocatalysts has been widely investigated to achieve the optimal performance strategically. Binding affinity with oxygen species, O*, HO* and HOO*, on the catalyst surface have been regarded as key determinant for catalytic performance. In the Sabatier principle, optimal catalytic performance could be exhibited with intermediate binding affinity between reactant molecules and the catalyst surface. The adsorption for oxygen species is restricted by too weak binding energy of oxygen on the catalyst surface, generation of HOO* species is limited by too strong binding energy of oxygen. Based on density

functional theory (DFT) studies, volcano-type relationship was constructed for the metal oxide-based catalysts using the difference between adsorption energies of HO* and HOO* as descriptor.^[11] Additionally, for perovskite-based catalysts, occupancy of e_g orbital in the surface metal cation was suggested as another descriptor for the OER activity, as the e_g orbital participates in σ bonding with anionic adsorbates.^[12] The e_g occupancy close to unity was the optimal electronic configuration for the lowest OER overpotential.

In the volcano-type relation for OER overpotential, the discrepancy between the theoretical and experimental values is observed. It is attributed that Sabatier principle focused on the bond rearrangement of oxygen species on the catalyst surface among various electrochemical processes in the catalyst-film. Specifically, the DFT studies using ΔG_O - ΔG_{OH} as descriptor predicted that 3d transition metal oxide (TMO)-based catalysts, such as Co₃O₄, NiO and Mn₃O₄, have similar overpotential with IrO_x and RuO₂.^[89] Experimentally, the overpotential values for these TMO-based catalysts are than hundreds millivolts higher than those for IrO_x and RuO₂. The discrepancy between experimental and theoretical values is caused by the structural factors for catalyst-film and detailed mechanistic difference on the active sites.

The TMO-based electrocatalysts are generally fabricated as film-like structures on the conductive bottom electrodes. The morphology and thickness for the catalyst-film are also key factors to determine overall catalytic performance. The high porosity for catalyst film contributed to the increase of surface area. It is related to activity enhancement due to the increase of the number of active sites. Also, the

catalyst-films showed the best efficiency with their optimal thickness. Below the optimal thickness, the activity was enhanced with increasing catalyst loadings. Over the optimal thickness, catalytic activity was saturated or degraded due to the electron transport resistance through the catalyst film. The thickness dependent trend could be explained by the competition between the increase of the number of active sites and electron transport resistance through the film.^[68] Additionally, the interfacial band structure between catalyst and bottom electrode needs to be considered to enhance activity for catalyst materials.^[90] These structural properties for film-type catalyst significantly contributes to the determination for the overall performance and discrepancy between experimental and theoretical overpotential values.^[90]

The reorganization for the chemical bonds entails valence state change of the metal center on the active sites during the multi-electron transfer catalysis. Prior to the O-O bond formation step, charge is accumulated with the metal valence change on the metal oxide-based catalysts. Thus, charge accumulation needs to be evaluated to understand rate-controlling process for the electrochemical OER among the various electrochemical processes in the film-type. For instance, O-O bond formation step is regarded as rate-determining step for the IrO_x catalysts in acidic electrolyte based on DFT and *in situ* spectroscopic studies.^[91] For the conventional 3d transition metal oxide, valence state change is rate determining step before O-O bond formation in neutral condition. In light of this, for the advanced design rule for OER electrocatalysts, charge accumulation process should be understood on the interface between catalyst surface and electrolyte during catalysis.

We previously developed sub 10 nm-sized Mn oxide nanocatalysts, which exhibited benign OER activity in neutral condition.^[49, 92] Combined with *in situ* spectroscopic analysis (XAS, UV-vis, Raman) and electrokinetic studies, we revealed their unique reaction mechanism which was totally different from the conventional Mn-based catalysts.^[50] Mn(IV) related species were detected as reaction intermediates from *in situ* spectroscopic analysis. It indicated that charge accumulation process was facilitated via Mn valence change prior to O-O bond formation step. Furthermore, electron transport characteristic for Mn oxide nanocatalyst film was analyzed via electrochemical impedance spectroscopy (EIS) using newly modified transmission line model.^[72] From the EIS study, overall catalytic performance was determined by the competition between charge transport and surface catalysis. Additionally, it was previously reported that electron transfer between the catalyst and bottom electrode was strongly affected the catalytic efficiency.^[90] From these mechanistic studies, various electrochemical process should be understood to achieve optimal catalytic activity and establish advanced design rule for film-type OER electrocatalysts.

Here, we analyzed complex capacitance on the Mn-oxide nanocatalyst film during OER via EIS study. For general capacitive materials, real (C') and imaginary (C'') capacitance indicated charge accumulation behavior and energy dissipation process on the interface, respectively.^[93-95] From this viewpoint, complex capacitance analysis could decouple charge accumulation process and electron transfer steps for OER on our Mn oxide nanocatalyst film. Furthermore, we newly proposed

dissipation factor ($D = C'/C''$) to describe the ratio of energy balance between charge accumulation process and electron transfer step. The potential dependent change for these parameters provided insight for charge accumulation on the heterogeneous electrocatalysts during OER. It could be applicable to establish design rule for OER electrocatalysts to describe experimental values clearly.

3.2. Results and Discussions

3.2.1. Mn valency change on Mn₃O₄ nanoparticles during catalysis

We previously synthesized sub 10-nm sized Mn oxide nanoparticles (NPs) via thermal decomposition method.^[49] The Mn oxide NPs were uniformly spin-coated on the conductive fluorine-doped tin oxide (FTO) substrates to fabricate nanoparticles film with hundreds-nanometers thickness. Then, the electrodes were annealed at 300 °C for 5 hour to form assembled Mn₃O₄ NPs film with removing organic ligands. The Mn₃O₄ NPs showed superb catalytic activity for OER compared to their bulk counterparts in neutral condition. The various electrochemical processes, such as surface catalysis, charge transport and charge accumulation occurred concurrently in the Mn₃O₄ NPs films during catalysis. The overall catalytic performance was determined by theses electrochemical processes. In this regard, the detailed mechanism and correlation between each processes is necessary to be understood to enhance the overall efficiency for the film-type electrocatalysts.

The unique reaction mechanism on the Mn₃O₄ NPs was previously investigated by electrokinetic studies and *in situ* spectroscopic analyses (Figure 3.1).^[50] From the previous mechanistic studies, the active Mn species were oxidized from Mn(II) to Mn(IV) during catalytic cycle. The Mn(III) species regarded as key species for OER were also stabilized on the NPs surface with asymmetric geometry during catalysis (Step I). Then, a concerted one proton (H⁺) and one electron (e⁻) transfer take place as quasi-equilibrium step (Step II). The Mn(IV) species were detected as reaction

intermediates by *in situ* spectroscopic analyses. Followed by the quasi-equilibrium step, the O-O bonds formation on Mn(IV)-oxo species proceeded as rate-determining step (RDS) for the surface catalysis (Step III). Oxygen molecules were generated in the subsequent process with the decrease of Mn valence (Step IV). In the proposed mechanism, the Mn valence showed reversible change with chemical bond rearrangement. It indicated that surface catalysis could be complementary process with charge accumulation and dissipation on the catalyst surface.

As shown in Figure 3.2, it showed cyclic voltammetry curve for 70 nm-thickness of Mn oxide NPs film under 0.5 M phosphate buffer solution (PBS) at pH 7. The catalytic current for markedly increased above 1.2 V vs. NHE, which was onset potential for electrochemical OER. Under 1.2 V vs. NHE, oxidative and reductive current were observed at forward and backward scan, respectively. The current was attributed to charge accumulation and dissipation which were related to Mn valence change between Mn(II) and Mn(III) species before OER. The overall OER activity was strongly correlated to the Mn redox capability because the stability Mn(III) species act as key determinant for OER in neutral condition.

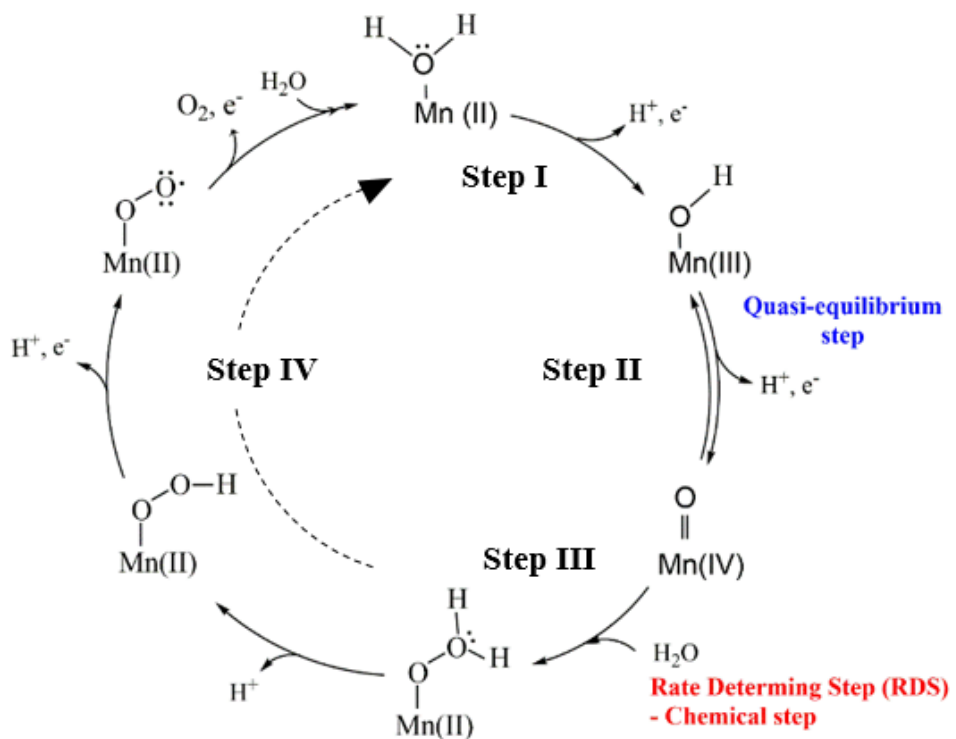


Figure 3.1. The proposed oxygen evolving reaction mechanism on Mn_3O_4 NPs (b) cyclic voltammetry curve for 70 nm-thickness Mn_3O_4 NPs electrodes under 0.5 M phosphate buffer solution (pH 7)

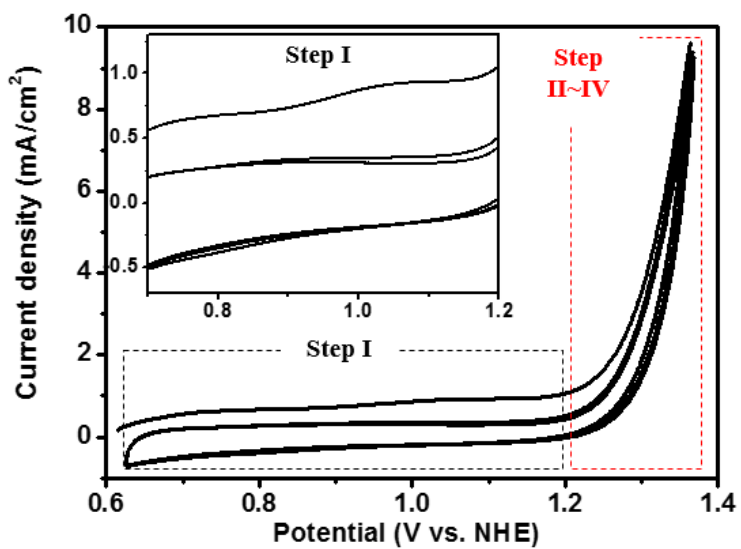


Figure 3.2. Cyclic voltammetry curve for 70 nm-thickness Mn_3O_4 NPs electrodes under 0.5 M phosphate buffer solution (pH 7)

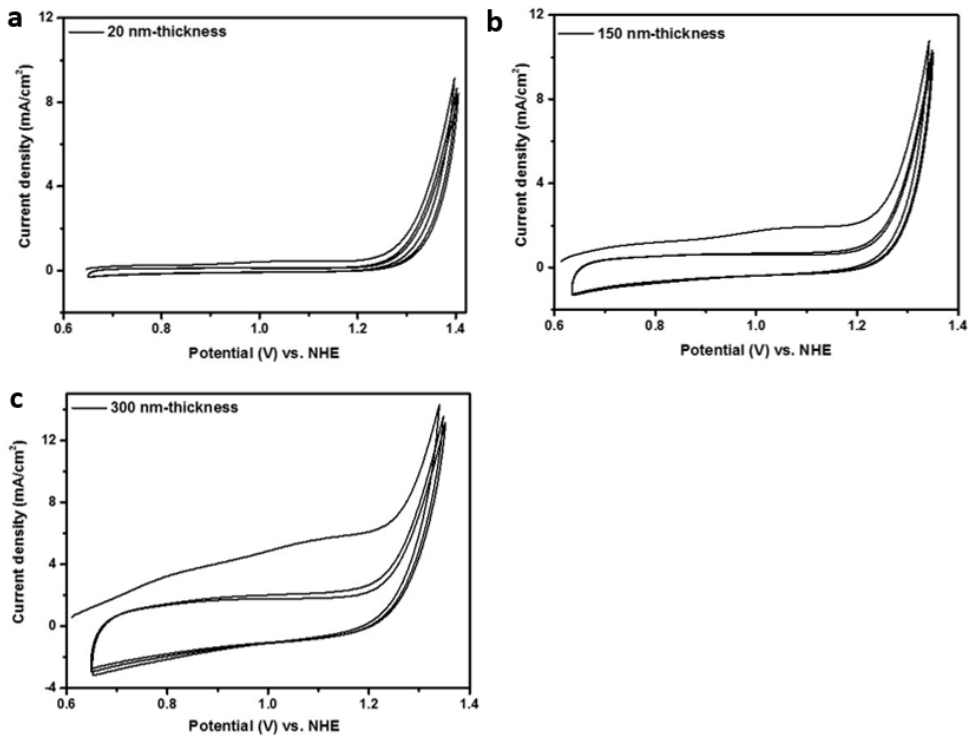


Figure 3.3. Cyclic voltammetry curves for Mn_3O_4 NPs on FTO substrates with (a) 20 nm- (b) 150 nm- and (c) 300 nm-thickness in 0.5 M phosphate buffer solution (pH 7)

3.2.2. Complex capacitance analysis from electrochemical impedance spectroscopy

3.2.2.1. Introduction for complex capacitance analysis

We conducted electrochemical impedance spectroscopic (EIS) analysis to understand charge accumulation process for Mn₃O₄ NPs film during catalysis. EIS analysis is effective tool to decouple various electrochemical processes. We previously parameterized electron transport and surface catalysis in the Mn₃O₄ NPs film using the proposed circuit model. Herein, we understood charge accumulation and dissipation process from impedance data (Z^*) which could be converted in to complex capacitance (C^*) into the following equation (Equation 1, 2).

$$C^*(\omega) = \frac{1}{j\omega Z^*(\omega)} \quad (1)$$

$$C^*(\omega) = C'(\omega) - jC''(\omega) \quad (2)$$

In the Equation 1 and 2, ω , j , C' and C'' were frequency, imaginary unit, real capacitance and imaginary capacitance, respectively. Real (C') and imaginary (C'') capacitance were calculated from real (Z') and imaginary (Z'') impedance according the following equation. (Equation 3, 4)

$$C'(\omega) = \frac{Z''(\omega)}{\omega |Z(\omega)|^2} \quad (3)$$

$$C''(\omega) = \frac{-Z'(\omega)}{\omega |Z(\omega)|^2} \quad (4)$$

Complex capacitance analysis was previously utilized to investigate capacitive characteristics for various energy materials.^[96-100] The complex capacitance analysis is effective tool to understand capacitive response at low frequency range, while impedance spectra generally concentrate on the analysis of the resistive behavior at high frequency range. The real capacitance represents the ability of the system to store electrical energy and imaginary capacitance indicates losses in the form of energy dissipation. For electrocatalyst system, real capacitance can be interpreted as the energy storage ability by charge accumulation process on the interface of catalyst and electrolyte, and imaginary capacitance is related to the energy losses by electrochemical catalytic reaction. In this regard, the complex capacitance analysis can show energy balance between charge accumulation and charge dissipation for OER on the Mn₃O₄ NPs film.

We measured EIS for 70 nm-thickness Mn₃O₄ NPs film in 0.5 M PBS at pH 7 between open circuit potential (OCP) to 1.35 V vs. NHE. As shown in Figure 3a, impedance data for the Mn₃O₄ NPs were displayed as Nyquist plot (Z' vs Z''). In the impedance spectra at OCP, semicircle and curve with low curvature were observed at lower and higher frequency range, respectively. The curve at high frequency range indicated the electrochemical processes on the interface between catalyst and electrolyte, and the semicircle at low frequency range was related to electron transport behavior through catalyst film and charge transfer process on the interface between catalyst and bottom electrode. As applying potential increased, semicircle shape disappeared and only curve with low curvature was observed at 0.8 and 1.0 V

vs. NHE. Above 1.2 V vs. NHE, new semicircle was emerged, which corresponds to oxygen evolving reaction on the catalyst surface. The size of semicircles reduced as potential increased from 1.2 to 1.35 V vs. NHE. The spectra change was attributable to the decrease of interfacial charge transfer resistance for OER with increasing potential.

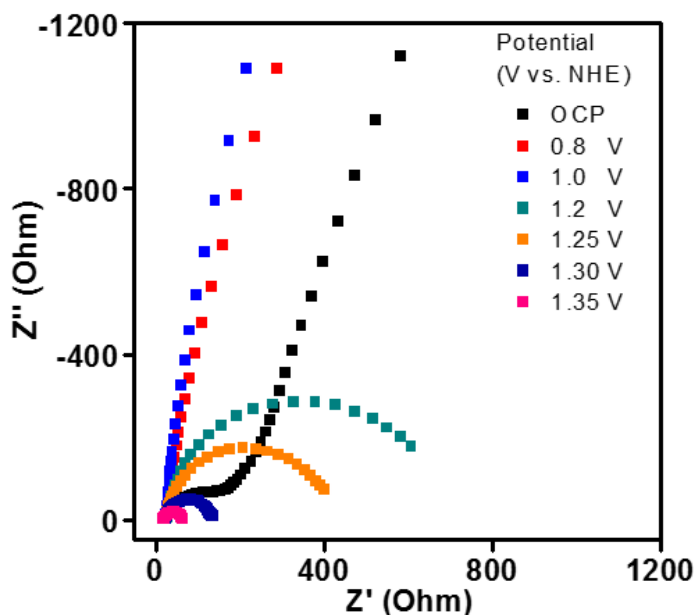


Figure 3.4. Nyquist plots (Z' vs Z'') for 70 nm-thickness Mn_3O_4 nanoparticles film at open circuit potential, 0.8, 1.0, 1.2, 1.25, 1.3 and 1.35 V vs. NHE.

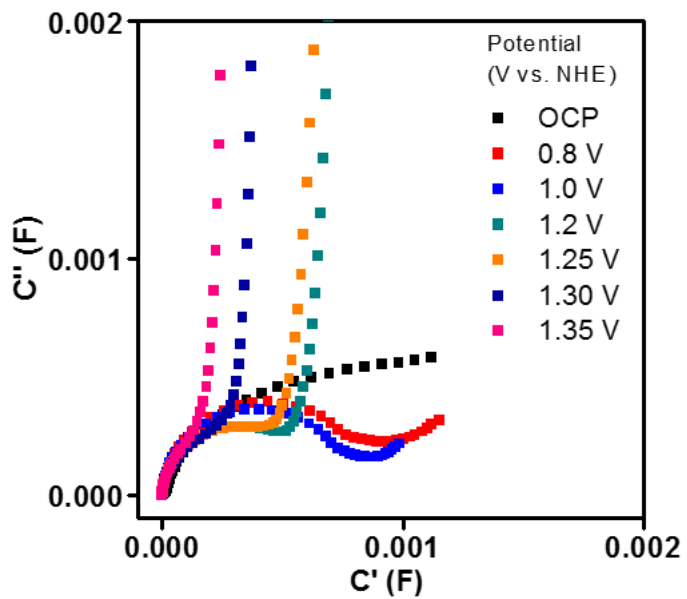


Figure 3.5. Complex capacitance (C' vs C'') plots for 70 nm-thickness Mn_3O_4 nanoparticles film at open circuit potential, 0.8, 1.0, 1.2, 1.25, 1.3 and 1.35 V vs. NHE

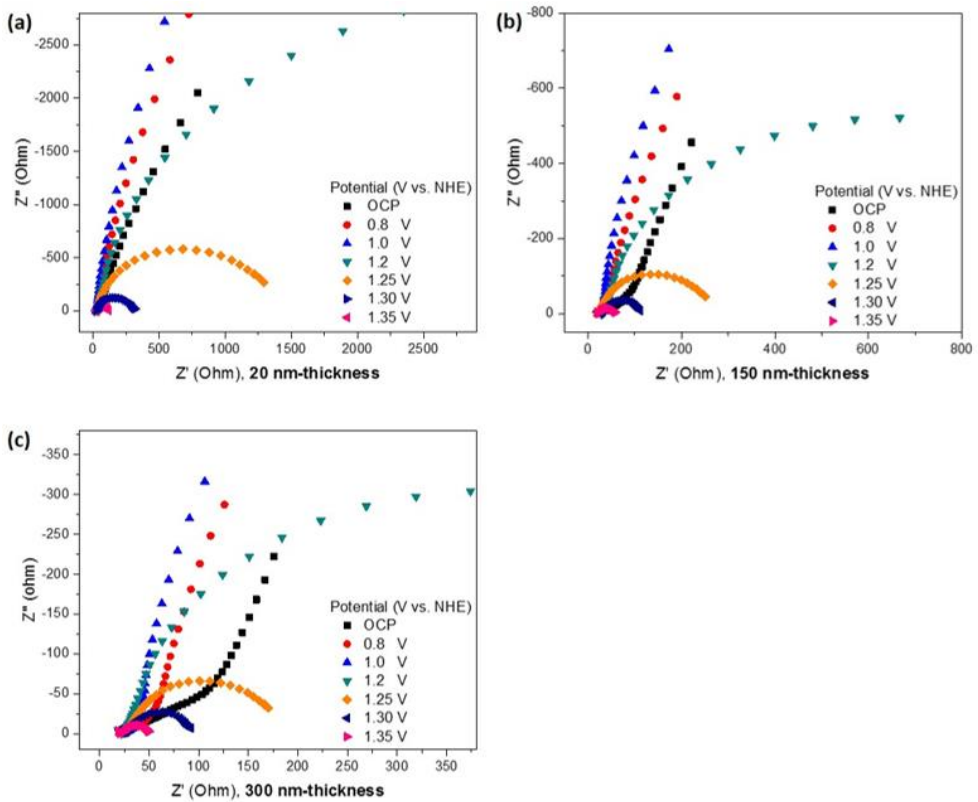


Figure 3.6. Nyquist plots (Z' vs Z'') for (a) 20 nm- (b) 150 nm- (c) 300 nm-thickness Mn₃O₄ NPs film at open circuit potential, 0.8, 1.0, 1.2, 1.25, 1.3 and 1.35 V vs. NHE

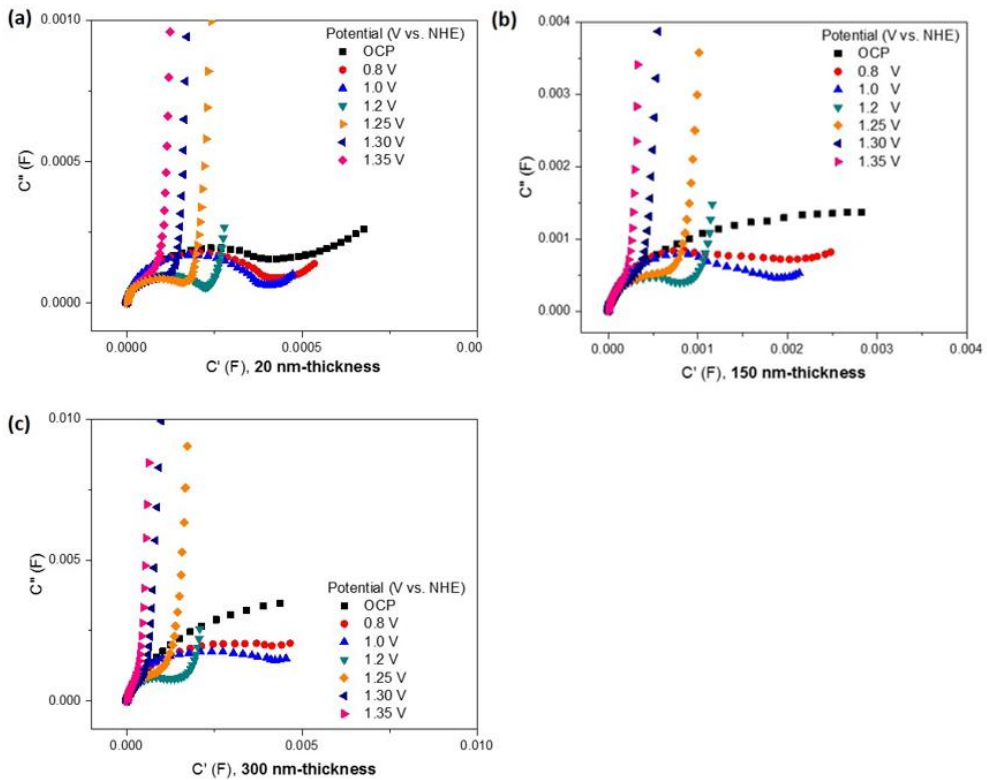


Figure 3.7 Complex capacitance plots (C' vs C'') for (a) 20 nm- (b) 150 nm- (c) 300 nm-thickness Mn_3O_4 NPs film at open circuit potential, 0.8, 1.0, 1.2, 1.25, 1.3 and 1.35 V vs. NHE

3.2.2.2. Complex capacitance analysis under OER onset potential

Complex capacitance were converted from impedance data using Equation 3 and 4 to analyze charge accumulation process in the Mn₃O₄NPs film during OER (Figure 3b). Additionally, the real and imaginary part of the complex capacitance were plotted as a function of frequency on a log scale. As shown in Figure 3.8, the values for C' and C'' were zero over 10² Hz. This resistive behavior indicated that charge was difficultly accumulated and energy dissipation process was inhibited at high frequency. At lower frequency range, capacitive behavior where C' increased was observed. As shown in Figure 3.8, capacitive peak and energy dissipative tail were observed. It indicated that charge accumulation and energy dissipation process were complementary interaction during OER on electrocatalyst film.

At open circuit potential, C' increased below 10¹ Hz and capacitive peak in log f vs C'' plot was observed around 10⁻¹ Hz. It was attributed to the formation of electric double layer near the catalyst surface. At 0.8 V vs. NHE, the increase of C' was observed at higher frequency range (~ 10² Hz) and the slope for C' changed at 10^{0.33} Hz (Figure 3.9 a). In the Figure 3.9 b, capacitive peak was positively shifted to 10¹ Hz. This spectra change was attributed for the charge accumulation with Mn valency change between Mn(II) and Mn(III) on the Mn₃O₄ NPs surface. At 1.0 V vs. NHE, C' slightly decreased at low frequency range (< 10^{0.33} Hz) and capacitive peak frequency was nearly unchanged (Figure 3.9 a).

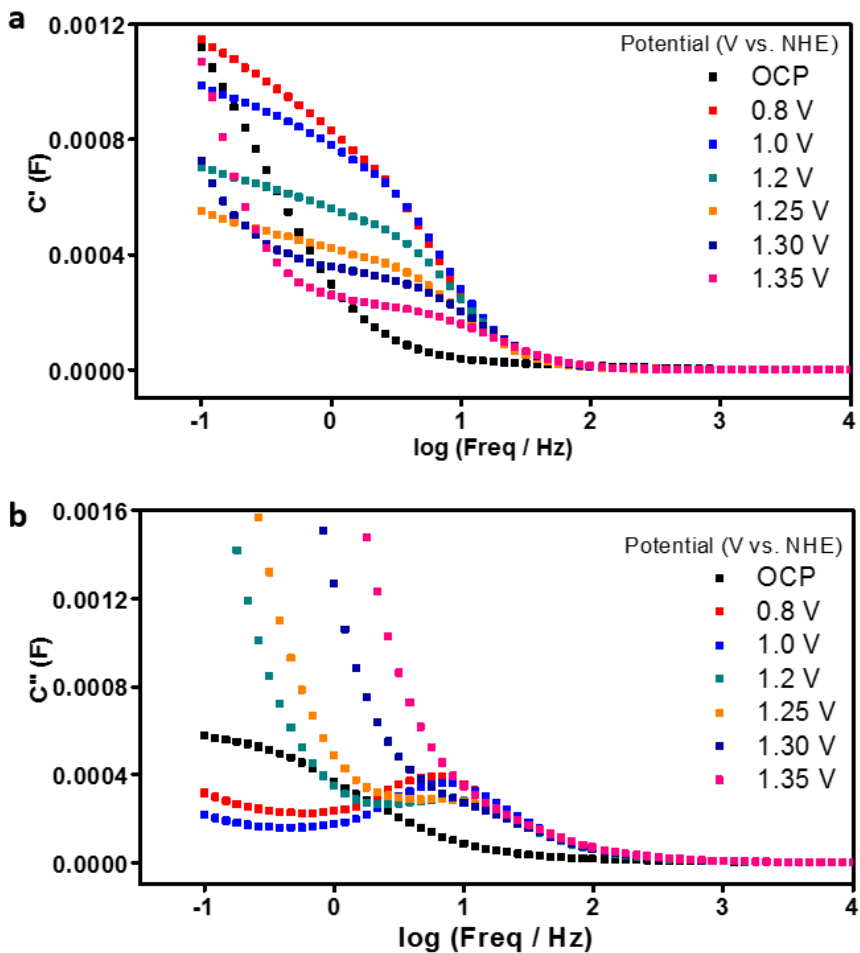


Figure 3.8 (a) Real part (C') and (b) Imaginary part (C'') for complex capacitance as a function of $\log (\text{Frequency} / \text{Hz})$ at open circuit potential (OCP), 0.8, 1.0, 1.2, 1.25, 1.3 and 1.35 V vs. NHE

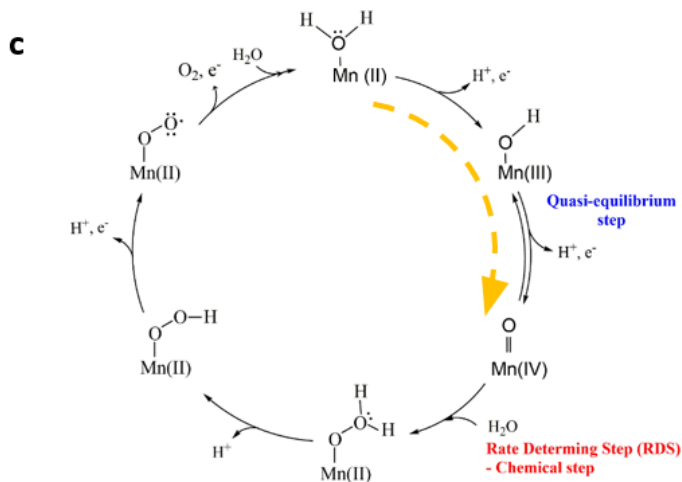
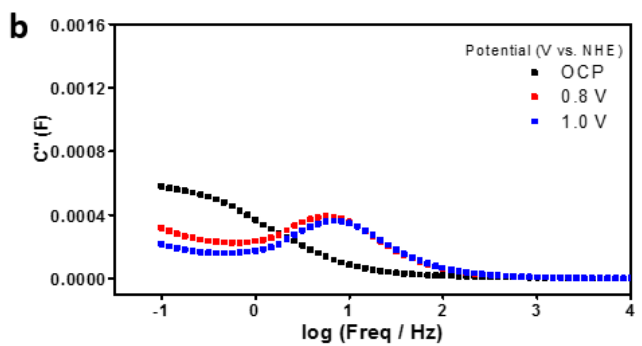
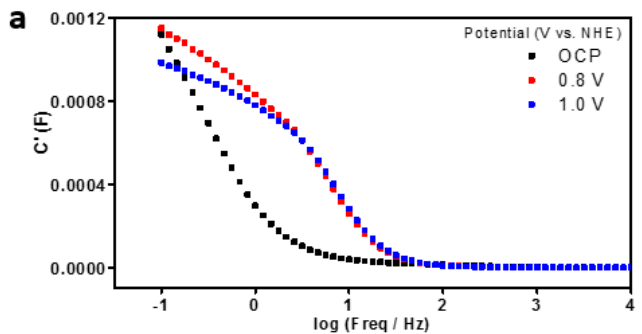


Figure 3.9 (a) Real part (C') and (b) Imaginary part (C'') for complex capacitance as a function of $\log (\text{Frequency} / \text{Hz})$ under OER onset potential ($\leq 1.0 \text{ V vs. NHE}$) (c) Scheme for OER mechanism on the Mn_3O_4 NPs

3.2.2.3. Complex capacitance analysis above OER onset potential

Above 1.2 V vs. NHE, substantial decrease of C' was observed at low frequency range (< 10 Hz). Also, in the Figure 3d, dissipative tails were emerged at low frequency range, which represented the charged dissipation on the interface between catalyst and electrolyte by oxygen evolving catalysis. The spectra change indicated that *Step III and IV* initiated at this potential range, where Mn(III)-OH and Mn(IV)=O species were sufficiently generated on the Mn_3O_4 NPs surface (Figure 3.1).^[50] The dissipative tail was positively shifted as potential increased from 1.2 to 1.35 V vs. NHE, which represents that OER proceeded briskly at higher potential. Additionally, above 1.3 V vs. NHE, the slope for C' became steeper at lower frequency range ($< 10^0$ Hz). It was attributed that charge was accumulated on the Mn_3O_4 NPs surface by electron transport limitation when OER occurred briskly at higher potential.

From the complex capacitance analysis, the increase of real part at low frequency range indicated that charge was accumulated by Mn valence change on the Mn_3O_4 NPs surface below OER onset potential. Above the onset potential, 1.2 V vs. NHE, the real part decreased and dissipative tail was observed in the imaginary part plot at the low frequency range. The spectra change represents that the accumulated charge was consumed to proceed the further steps for OER (Step III-IV, Figure 3.10 c). At higher potential (> 1.30 V vs. NHE), electron transport limitation contributed to the charge accumulation, which was In this regard, complex capacitance analysis

demonstrated energy balance between charge accumulation and dissipation for various electrochemical processes on the Mn₃O₄ NPs during OER.

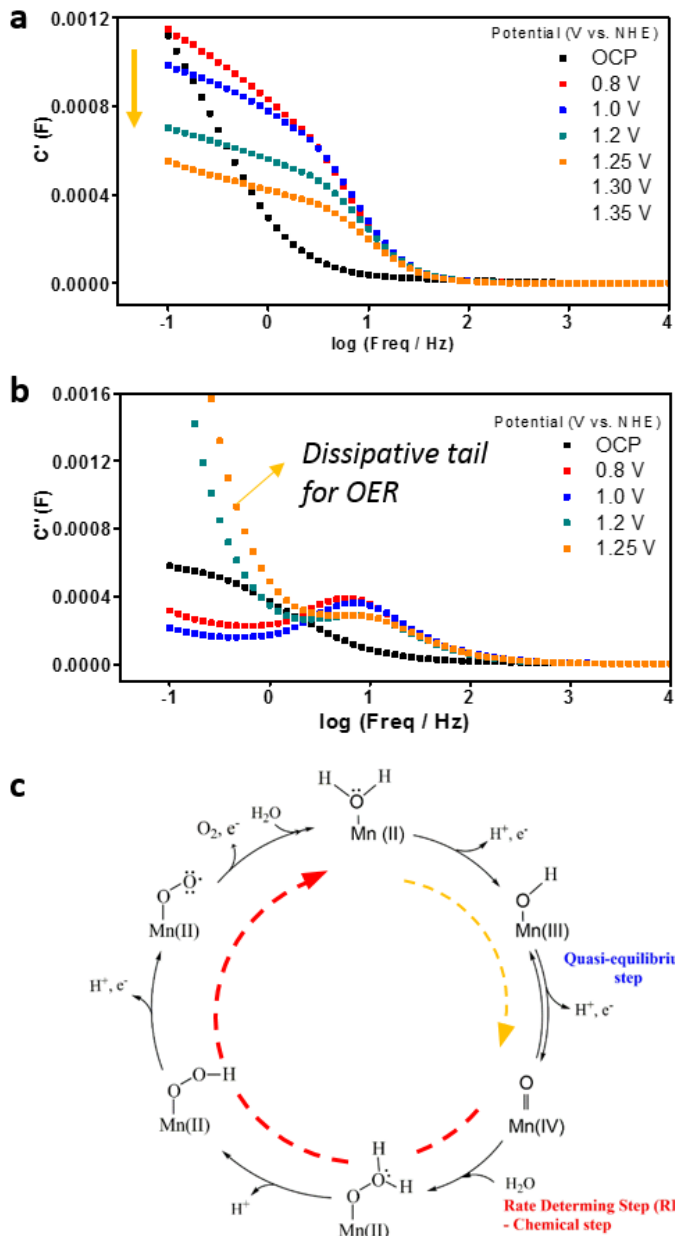


Figure 3.10 (a) Real part (C') and (b) Imaginary part (C'') for complex capacitance as a function of $\log (\text{Frequency} / \text{Hz})$ under OER onset potential ($\geq 1.2 \text{ V}$ vs. NHE) (c) Scheme for OER mechanism on the Mn_3O_4 NPs

3.2.3. Dissipation ratio ($D = C' / C''$) for OER onset potential

Furthermore, we introduced the dissipation factor (D) which is calculated by the ratio of C' and C'' to analyze the correlation between energy balance and various electrochemical processes in Mn_3O_4 NPs film during OER (Equation 5).

$$D(f) = \frac{C'(f)}{C''(f)} \quad (5)$$

The dissipation factor (D) indicated the ratio of charge accumulation ability with respect to the dissipation processes. On the Mn_3O_4 NPs film, charge could be accumulated by the formation of electric double layer, Mn valence change and electron transport limitation during catalysis. The energy dissipation process was attributed to the charge consumption by oxygen evolving reaction.

As shown in Figure 3.11, the dissipation factors were plotted as a function of frequency on log scale at several applying potentials. We found that dissipation factor (D_{max}) was maximized at the specific frequency (f_{max}) at each spectra (Figure 4a). Below 1.0 V vs. NHE, the D_{max} increased and f_{max} was not significantly changed as the potential rose. The values for D_{max} were measured as 4.2 and 5.6 at 0.8 V and 1.0 V vs. NHE, respectively. The f_{max} were estimated as $10^{-0.5}$ Hz. The increase of D_{max} was attributed that charge accumulation was superior to energy dissipation process with Mn valence change in the Step I (Figure 3.1). Above 1.0 V vs. NHE, where $\text{Mn}(\text{III})\text{-OH}$ species were sufficiently generated, D_{max} decreased and f_{max} positively shifted with increasing potential. The values for D_{max} were 1.91, 1.52, 0.79 and 0.47 at 1.2, 1.25, 1.3 and 1.35 V vs. NHE, respectively. The f_{max} were measured

as $10^{0.25}$, $10^{0.5}$, $10^{0.83}$ and $10^{1.17}$ Hz at 1.2, 1.25, 1.3 and 1.35 V vs. NHE, respectively.

The decrease in D_{max} represents that charge consumption for catalysis was dominant process compared to charge accumulation on the Mn_3O_4 NPs. The increase of f_{max} was due to the increase of kinetics dissipation process as increasing potential above 1.2 V vs. NHE (Figure 3.13 b).

In the Figure 3.12, the dissipation factors were measured for the 20 nm-, 70 nm-, 150 nm- and 300 nm-thickness Mn_3O_4 NPs film at 1.35 V vs. NHE. As the thickness for Mn_3O_4 NPs film increased, D_{max} and f_{max} concomitantly decreased at 1.35 V vs. NHE. The D_{max} were measured as 0.64, 0.47, 0.37 and 0.28 for 20 nm, 70 nm, 150 nm and 300 nm thickness, respectively. The values for f_{max} were $10^{1.33}$, $10^{1.08}$, $10^{0.92}$ and $10^{0.67}$ Hz for 20 nm, 70 nm, 150 nm and 300 nm thickness, respectively. The decrease for D_{max} was due to the enhancement of dissipation process, surface catalysis for the porous Mn_3O_4 NPs electrode. The decrease of f_{max} reflected that the kinetics for overall oxygen evolving catalysis was slower for thicker Mn_3O_4 NPs film due to electron transport limitation.

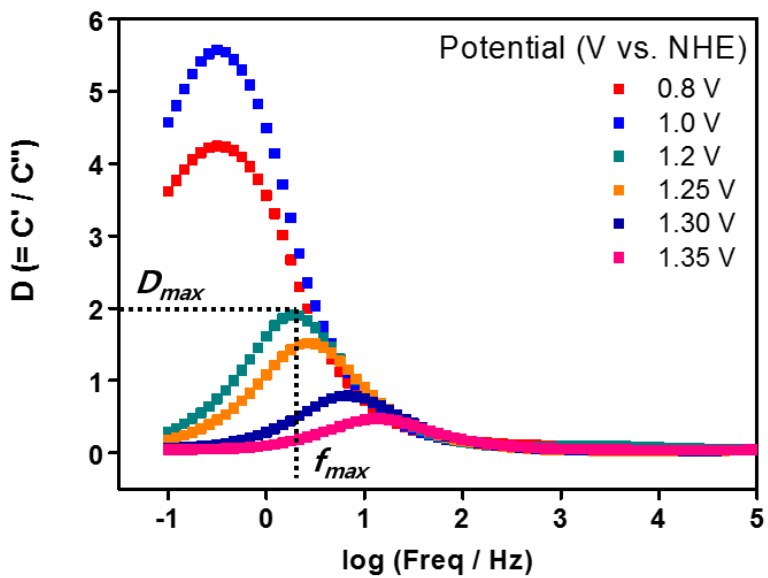


Figure 3.11 Dissipation factors (C'/C'') as a function of frequency for 70 nm-thickness film at OCP, 0.8, 1.0, 1.2, 1.25, 1.3 and 1.35 V vs. NHE.

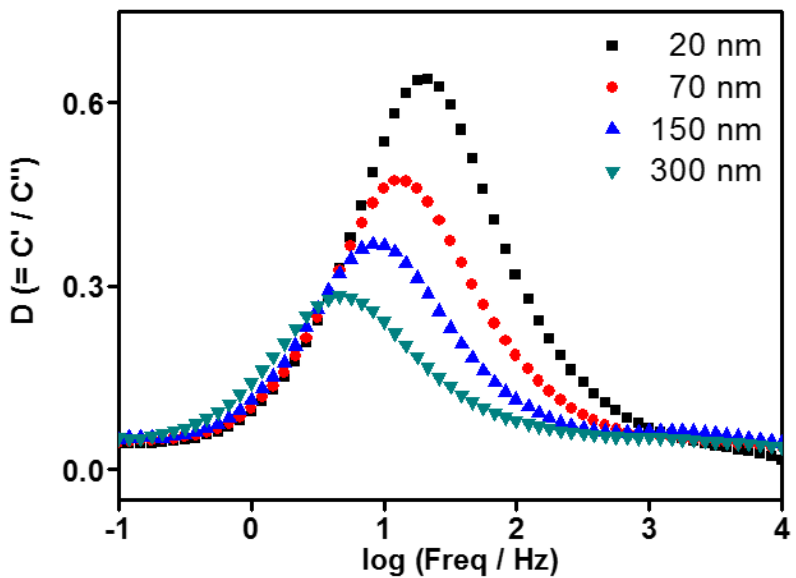


Figure 3.12 Dissipation factors (C'/C'') as a function of frequency at 1.35 V vs. NHE with 20 nm-, 70 nm-, 150 nm- and 300 nm-thickness.

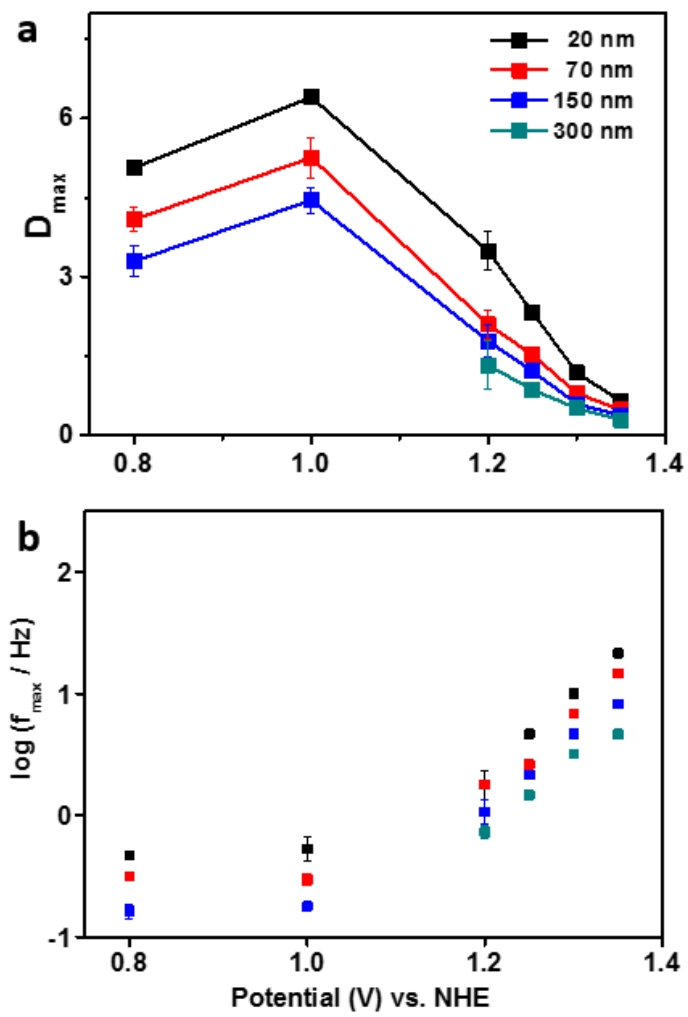


Figure 3.13 Dissipation factors (C'/C'') as a function of frequency at 1.35 V vs. NHE with 20 nm-, 70 nm-, 150 nm- and 300 nm-thickness.

3.3. Concluding Remarks

We conducted complex capacitance analysis for Mn₃O₄ NPs film to understand charge accumulation process on the catalyst surface during OER. From complex capacitance analysis, charge was accumulated on the catalyst surface by Mn valence change between Mn(II) to Mn(IV) below 1.2 V vs. NHE. Above 1.2 V vs. NHE, the accumulated charge was used up by oxygen evolving catalysis. We newly proposed dissipation factor as the ratio of real capacitance with respect to imaginary capacitance to analyze the energy balance between charge accumulation process and charge dissipation for catalytic reaction. The potential dependence for dissipation ratio represented that charge dissipation process was superior to charge accumulation at higher potential. Additionally, the thickness dependence for dissipation factor indicated that electron transport limitation induced charge accumulation on the catalyst surface for the thicker catalyst film. We believe that the complex capacitance analysis using EIS could be generalized for various film-type electrocatalyst to investigate charge accumulation process on the catalyst surface.

Chapter 4. Conclusion

In Chapter 2, we conducted electrochemical impedance spectroscopy analysis for our Mn_3O_4 NPs electrocatalysts to extract kinetic parameters. The overall catalytic performance was determined by various electrochemical processes, such as surface catalysis, electron transport and charging processes. We established the suitable circuit model including Havriliak-Negami capacitors, which represents the electrochemical phenomena on the Mn_3O_4 NPs during catalysis. From fitting analysis, we clearly decoupled electron transport and surface catalysis from extracting transport resistance (R_{tr}) and interface resistance (R_{int}). Furthermore, we found that protons (H^+) are involved in not only surface catalysis but also electron transport process in the Mn_3O_4 NPs catalyst film during catalysis. It indirectly supported ongoing hypothesis that protons are hopping with oxo species in the film-type electrocatalysts. Also, reaction rate constant (k) could be estimated for heterogeneous electrocatalysts from fitting analysis with our proposed circuit model. It has been regarded as challenging issue due to difficulty to evaluate the ratio of active sites on the catalyst surface. We believe that impedance analysis with our proposed circuit model could be powerful tool to understand and parameterize various electrochemical processes in the film-type electrocatalysts.

In Chapter 3, our studies explained charging process on the interface between catalyst and electrolyte. We previously demonstrated water oxidizing mechanism on

the Mn₃O₄ NPs with Mn valence change from Mn(II) to Mn(IV). The charging behavior on the Mn₃O₄ NPs was strongly attributed for the Mn valency change during OER catalysis. We converted impedance data into complex capacitance for the Mn₃O₄ NPs electrocatalysts. Real part of capacitance represents charging process on the interface between catalyst and electrolyte. Imaginary part of capacitance indicates charge dissipation process, such as OER catalysis. Charge was accumulated on the catalyst surface by Mn valence change between Mn(II) to Mn(IV) below 1.2 V vs. NHE. Above 1.2 V vs. NHE, the accumulated charge was dissipated by oxygen evolving catalysis. Furthermore, we established dissipation ratio as a parameter to understand the kinetics of Mn valency change. We believe that the complex capacitance analysis could be generalized to understand charging behavior by metal valency change on heterogeneous electrocatalysts for various electrochemical reactions.

References

- [1] A. Kudo, Y. Miseki, *Chemical Society Reviews* **2009**, *38*, 253-278.
- [2] World Energy Outlook 2015, *International Energy Agency*, **2015**
- [3] U. S. E. I. Administration., **2013**.
- [4] M. M. Rashid, M. K. Al Mesfer, H. Naseem, M. Danish, *Int. J. Eng. Adv* **2015**, *4*, 3, 80-93
- [5] A. Ursua, L. M. Gandia, P. Sanchis, *Proceedings of the IEEE* **2012**, *100*, 410-426.
- [6] M. A. Khan, H. Zhao, W. Zou, Z. Chen, W. Cao, J. Fang, J. Xu, L. Zhang, J. Zhang, *Electrochemical Energy Reviews* **2018**, *1*, 483-530
- [7] Y. Jiao, Y. Zheng, M. Jaroniec, S. Z. Qiao, *Chem. Soc. Rev.* **2015**, *44*, 2060-2086
- [8] J. K. Nørskov, T. Bligaard, A. Logadottir, J. R. Kitchin, J. G. Chen, S. Pandelov, U. Stimming, *J. Electrochem. Soc.* **2005**, *152*(3), J23-J26
- [9] Z. W. Seh, J. Kibsgaard, C. F. Dickens, I. Chorkendorff, J. K. Nørskov, T. F. Jaramillo, *Science* **2017**, *355*, 146
- [10] C. C. McCrory, S. Jung, I. M. Ferrer, S. M. Chatman, J. C. Peters, T. F. Jaramillo, *J. Am. Chem. Soc.* **2015**, *137* (13), 4347–4357
- [11] I. C. Man, H. –Y. Su, F. Calle-Vallejo, H. A. Hansen, J. I. Martinez, N. G. Inoglu, J. Kitchin, T. F. Jaramillo, J. K. Nørskov, J. Rossmeisl, *ChemCatChem* **2011**, *3*, 1159–1165
- [12] J. Suntivich, K. J. May, H. A. Gasteiger, J. B. Goodenough, Y. Shao-Horn, *Science* **2011**, *334*, 1383
- [13] M. Zhang, M. de Respinis, H. Frei, *Nat. Chem.* **2014**, *6*, 362-367
- [14] J. B. Gerken, J. G. McAlpin, J. Y. C. Chen, M. L. Rigsby, W. H. Casey, R. D. Britt, S. S. Stahl, *J. Am. Chem. Soc.* **2011**, *133*, 14431-14442
- [15] L.-P. Wang, T. Van Voorhis, *J. Phys. Chem. Lett.* **2011**, *2*, 2200

- [16] K. Takada, K. Fukuda, M. Osada, I. Nakai, F. Izumi, R. A. Dilanian, K. Kato, M. Takata, H. Sakurai, E. T.-Muromachi, T. Sasaki, *J. Mater. Chem.* **2004**, *14*(9) 1448-1453
- [17] T. Motohashi, Y. Katsumata, T. Ono, R. Kanno, M. Karppinen, H. Yamauchi, *Chem. Mater.* **2007**, *19*(21), 5063-5066
- [18] M. Huynh, D. K. Bediako, D. G. Nocera, *J. Am. Chem. Soc.* **2014**, *136*(16), 6002-6010
- [19] L. Duan, F. Bozoglian, S. Mandal, B. Stewart, T. Privalov, A. Llobet, L. Sun, *Nat. Chem.* **2012**, *4* (5), 418-423
- [20] M. M. Najafpour, M. A. Isaloo, *RSC Advances* **2014**, *4* (13), 6375-6378
- [21] Y. Surendranath, M. W. Kanan, D. G. Nocera, *J. Am. Chem. Soc.* **2010**, *132*, 16501-16509
- [22] H. Seo, K. H. Cho, H. Ha, S. Park, J. S. Hong, K. Jin, K. T. Nam, *J. Korean Ceram. Soc.* **2017**, *54*(1), 1-8
- [23] Y. Kim, D. Shin, W. J. Chang, H. L. Jang, C .W. Lee, H. -E. Lee, K. T. Nam, *Adv. Funct. Mater.* **2015**, *25*, 2369–2377
- [24] A. Klauss, M. Haumann, H. Dau, *Proc. Natl. Acad. Sci. U.S.A.* **2012**, *109*, 16035–16040.
- [25] J. Lavergne, W. Jung, *Photosynth. Res.* **1993**, *38*, 279-296
- [26] B. Kok, B. Forbush, M. McGloin, *Photochem. Photobiol.* **1970**, *11*, 457–475.
- [27] A. Zouni, H. -T. Witt, J. Kern, P. Fromme, N. Krauss, W. Saenger, P. Orth, *Nature* **2001**, *409*, 739–743
- [28] Y. Umena, K. Kawakami, J.-R. Shen, N. Kamiya, *Nature* **2011**, *473*, 55–60
- [29] M. Pérez-Navarro, F. Neese, W. Lubitz, D.A. Pantazis, N. Cox, *Curr. Opin. Chem. Biol.* **2016**, *31*, 113–119.
- [30] V. Krewald, M. Retegan, N. Cox, J. Messinger, W. Lubitz, S. DeBeer, F. Neese, D.A. Pantazis, *Chem. Sci.* **2015**, *6*, 1676–1695.
- [31] M. Suga, F. Akita, K. Hirata, G. Ueno, H. Murakami, Y. Nakajima, T.

- Shimizu, K. Yamashita, M. Yamamoto, H. Ago, *Nature* **2015**, *517*, 99-103
- [32] J. Yano, V. Yachandra, *Chem. Rev.* **2014**, *114*, 4175–4205
- [33] N. Cox, M. Retegan, F. Neese, D. A. Pantazis, A. Boussac, W. Lubitz, *Science* **2014** *345*, 804–808
- [34] V. Krewald, M. Retegan, F. Neese, W. Lubitz, D.A. Pantazis, N. Cox, *Inorg. Chem.* **2015**, *55*, 488–501
- [35] M. P. Navarro, W. M. Ames, H. Nilsson, T. Lohmiller, D. A. Pantazis, L. Rapatskiy, M. M. Nowaczyk, F. Neese, A. Boussac, J. Messinger, *Proc. Natl. Acad. Sci. U.S.A.* **2013**, *110*, 15561–15566
- [36] S. Park, Y. H. Lee, S. Choi, H. Seo, M. Y. Lee, M. Balamurugan, K. T. Nam, *Energy Environ. Sci.* **2020**, *13*, 2310-2340
- [37] D. A. Kitchaev, S. T. Dacek, W. Sun, G. Ceder, *J. Am. Chem. Soc.* **2017**, *139*, 2672-2681
- [38] W. Sun, D. A. Kitchaev, D. Kramer and G. Ceder, *Nat. Commun.* **2019**, *10*, 573
- [39] Y. Meng, W. Song, H. Huang, Z. Ren, S. Y. Chen, S. L. Suib, *J. Am. Chem. Soc.* **2014**, *136*, 11452–11464
- [40] C. -H. Kuo, I. M. Mosa, A. S. Poyraz, S. Biswas, A. M. El-Sawy, W. Song, Z. Luo, S. -Y. Chen, J. F. Rusling, J. He, S. L. Suib, *ACS Catal.* **2015**, *5*, 1693–1699
- [41] P. F. Smith, B. J. Deibert, S. Kaushik, G. Gardner, S. Hwang, H. Wang, J. F. Al-Sharab, E. Garfunkel, L. Fabris, J. Li, G. C. Dismukes, *ACS Catal.* **2016**, *6*, 2089–2099
- [42] I. Zaharieva, P. Chernev, M. Risch, K. Klingan, M. Kohlhoff, A. Fischer, H. Dau, *Energy Environ. Sci.* **2012**, *5*, 7081–7089
- [43] A. Bergmann, I. Zaharieva, H. Dau, P. Strasser, *Energy Environ. Sci.* **2013**, *6*, 2745–2755

- [44] A. Indra, P. W. Menezes, I. Zaharieva, E. Baktash, J. Pfrommer, M. Schwarze, H. Dau and M. Driess, *Angew. Chem., Int. Ed.* **2013**, *52*, 13206–13210
- [45] M. Huynh, C. Shi, S. J. Billinge, D. G. Nocera, *J. Am. Chem. Soc.* **2015**, *137*, 14887–14904
- [46] Z. Morgan Chan, D. A. Kitchaev, J. Nelson Weker, C. Schnedermann, K. Lim, G. Ceder, W. Tumas, M. F. Toney, D. G. Nocera, *Proc. Natl. Acad. Sci. U.S.A.* **2018**, *115*, 5261–5268
- [47] T. Takashima, K. Hashimoto, R. Nakamura, *J. Am. Chem. Soc.* **2012**, *134*, 1519–1527
- [48] T. Takashima, K. Hashimoto, R. Nakamura, *J. Am. Chem. Soc.* **2012**, *134*, 18153–18156
- [49] K. Jin, A. Chu, J. Park, D. Jeong, S. E. Jerng, U. Sim, H.-Y. Jeong, C. W. Lee, Y.-S. Park, K. D. Yang, G. K. Pradhan, D. Kim, N.-E. Sung, S. H. Kim, K. T. Nam, *Sci. Rep.* **2015**, *5*, 10279, 1–11
- [50] K. Jin, H. Seo, T. Hayashi, M. Balamurugan, D. Jeong, Y. K. Go, J. S. Hong, K. H. Cho, H. Kakizaki, N. Bonnet-Mercier, M. G. Kim, S. H. Kim, R. Nakamura, K. T. Nam, *J. Am. Chem. Soc.* **2017**, *139*, 2277–2285
- [51] R. L. Doyle, M. E. G. Lyons, *Phys. Chem. Chem. Phys.* **2013**, *15*, 5224–5237
- [52] D. K. Bediako; C. Costentin, E. C. Jones, D. G. Nocera, J. –M. Saveant, *J. Am. Chem. Soc.* **2013**, *135* (28), 10492–10502
- [53] G. Kwon, H. Jang, J. -S. Lee, A. Mane, D. J. Mandia, S. R. Soltau, L. M. Utschig, A. B. Martinson, D. M. Tiede, H. Kim, *J. Am. Chem. Soc.* **2018**, *140* (34), 10710–10720
- [54] Y. Gorlin, B. Lassalle-Kaiser, J. D. Benck, S. Gul, S. M. Webb, V. K. Yachandra, J. Yano, T. F. Jaramillo, *J. Am. Chem. Soc.* **2013**, *135* (23), 8525–8534
- [55] M. Risch, K. A. Stoerzinger, B. Han, T. Z. Regier, D. Peak, S. Y. Sayed, C. Wei, Z. Xu, Y. Shao-Horn, *J. Phys. Chem. C* **2017**, *121* (33), 17682–17692

- [56] Y. Deng, A. D. Handoko, Y. Du, S. Xi, B. S. Yeo, *ACS Catal.* **2016**, *6* (4), 2473–2481
- [57] F. Fabregat-Santiago, J. Bisquert, G. Garcia-Belmonte, G. Boschloo, A. Hagfeldt, *Sol. Energy Mater. Sol. Cells* **2005**, *87*, 117–131
- [58] Q. Wang, S. Ito, M. Grätzel, F. Fabregat-Santiago, I. Mora-Sero, J. Bisquert, T. Bessho, H. Imai, *J. Phys. Chem. B* **2006**, *110* (50), 25210-25221
- [59] Q. Wang, J.-E. Moser, M. Grätzel, *J. Phys. Chem. B* **2005**, *109* (31), 14945-14953
- [60] L. Tao, Z. Huo, Y. Ding, Y. Li, S. Dai, L. Wang, J. Zhu, X. Pan, B. Zhang, J. Yao, *J. Mater. Chem. A* **2015**, *3* (5), 2344-2352
- [61] T. Lopes, L. Andrade, F. Le Formal, M. Gratzel, K. Sivula, A. Mendes, *Phys. Chem. Chem. Phys.* **2014**, *16* (31), 16515–16523
- [62] R. Barfod, M. Mogensen, T. Klemensø, A. Hagen, Y.-L. Liu, P. V. Hendriksen, *J. Electrochem. Soc.* **2007**, *154* (4), B371-B378
- [63] A. Leonide, Y. Apel, E. Ivers-Tiffey, *ECS Trans.* **2009**, *19*(20), 81-109
- [64] H. Vrubel, T. Moehl, M. Grätzel, X. Hu, *Chem. Commun.* **2013**, *49* (79), 8985-8987
- [65] K. S. Cole, R. H. Cole, *J. Chem. Phys.* **1941**, *9* (4), 341-351.
- [66] S. Havriliak, S. Negami, *Journal of Polymer Science Part C: Polymer Symposia*, Wiley Online Library, **1966**, 99-117
- [67] Lee, J.-S. *J. Korean Ceram. Soc.* **2016**, *53* (2), 150-161
- [68] C. G. Morales-Guio, L. Liardet, X. Hu, *J. Am. Chem. Soc.* **2016**, *138* (28), 8946-8957
- [69] H. H. Pham, M. –J. Cheng, H. Frei, L. –W. Wang, *ACS catal.* **2016**, *6* (8), 5610-5617
- [70] K. Jin, J. Park, J. Lee, K. D. Yang, G. K. Pradhan, U. Sim, D. Jeong, H. L. Jang, S. Park, D. Kim, N. –E. Sung, S. H. Kim, S. Han, K. T. Nam, *J. Am. Chem. Soc.* **2014**, *136* (20), 7435-7443
- [71] J. Park, H. Kim, K. Jin, B. J. Lee, Y. –S. Park, H. Kim, I. Park, K. D. Yang,

- H. -Y. Jeong, J. Kim, K. T. Hong, H. W. Jang, K. Kang, K. T. Nam, *J. Am. Chem. Soc.* **2014**, 136 (11), 4201-4211
- [72] H. Seo, K. Jin, S. Park, K. H. Cho, H. Ha, K. -G. Lee, Y. H. Lee, D. T. Nguyen, H. Randriamahazaka, J. -S. Lee, K. T. Nam, *ACS Sustainable Chem. Eng.* **2019**, 7, 10595-10604
- [73] K. H. Cho, H. Seo, S. Park, Y. H. Lee, M. Y. Lee, N. H. Cho, K. T. Nam, *Adv. Funct. Mater.* **2020**, 30, 1910424, 1-9
- [74] M. E. Lyons, M. P. J. Brandon, *Electroanal. Chem.* **2009**, 631 (1-2), 62-70.
- [75] H. T. Nguyen, T. L. Tran, D. T. Nguyen, E.-C. Shin, S.-H. Kang, J. -S. Lee, *J. Korean Ceram. Soc.* **2018**, 55 (3), 244-260
- [76] S. -H. Moon, Y. H. Kim, D. -C. Cho, E. -C. Shin, D. Lee, W. B. Im, J. -S. Lee, *Solid State Ionics* **2016**, 289, 55-71
- [77] K.-W. Nam, K.-B. Kim, *J. Electrochem. Soc.* **2006**, 153 (1), A81-A88
- [78] K. Jang, S.-W. Lee, S. Yu, R. R. Salunkhe, I. Chung, S. Choi, H. Ahn, *Bull. Korean Chem. Soc.* **2014**, 35 (10), 2975.
- [79] X. Cui, F. Hu, W. Wei, W. Chen, *Carbon*, **2011**, 49 (4), 1225-1234.
- [80] J. W. Lee, A. S. Hall, J.-D. Kim, T. E. Mallouk, *Chem. Mater.* **2012**, 24 (6), 1158-1164.
- [81] B. Wang, J. Park, C. Wang, H. Ahn, G. Wang, *Electrochimica Acta*, **2012**, 55 (22), 6812-6817.
- [82] D. K. Bediako, B. Lassalle-Kaiser, Y. Surendranath, J. Yano, V. K. Yachandra, D. G. Nocera, *J. Am. Chem. Soc.* **2012**, 134 (15), 6801-6809
- [83] H. S. Ahn, A. J. Bard, *J. Am. Chem. Soc.* **2015**, 137, 2, 612–615
- [84] M. Dresselhaus, I. Thomas, *Nature* **2001**, 414 (6861), 332-337
- [85] D. K. Bediako, Y. Surendranath, D. G. Nocera, *J. Am. Chem. Soc.* **2013**, 135 (9), 3662-3674
- [86] K. Zhu, X. Zhu, W. Yang, *Angew. Chem. int. Ed.* **2019**, 58 (5), 1252-1265.
- [87] H. -Y. Wang, S. -F. Hung, Y. -Y. Hsu, L. Zhang, J. Miao, T. -S. Chan, Q. Xiong, B. Liu, *J. Phys. Chem. Lett.* **2016**, 7 (23), 4847-4853.

- [88] B. S. Yeo, A. T. Bell, *J. Phys. Chem. C* **2012**, *116* (15), 8394-8400
- [89] M. Busch, E. Ahlberg ,I. Panas, *J. Phys. Chem. C* **2013**, *117* (1), 288-292
- [90] M. Y. Lee, H. Ha, K. H. Cho, H. Seo, S. Park, Y. H. Lee, S.-J. Kwon, T.-W. Lee, K. T. Nam, *ACS Catal.* **2020**, *10*, 2, 1237-1245
- [91] H. Ooka, A. Yamaguchi, T. Takashima, K. Hashimoto, R. Nakamura, *J. Phys. Chem. C* **2017**, *121* (33), 17873-17881.
- [92] J. S. Hong, H. Seo, Y. H. Lee, K. H. Cho, C. Ko, S. Park, K. T. Nam, *Small Methods* **2020**, *4*, 190073, 1-7
- [93] C. Yang, C.-Y. V. Li, F. Li, K.-Y. Chan, *J. Electrochem. Soc.* **2013**, *160* (4), H271-H278
- [94] J. M. Soon, K. P. Loh, *Electrochem. Solid-State Lett.* **2007**, *10*(11), A250-A254
- [95] J. H. Jang, S. Yoon, B. H. Ka, Y.-H. Jung, S. M. Oh, *J. Electrochem. Soc.* **2005**, *152*(7), A1418-A1422
- [96] J. Jamnik, J. Maier, *Phys. Chem. Chem. Phys.* **2001**, *3* (9), 1668-1678.
- [97] J. H. Jang, S. M. Oh, *J. Electrochem. Soc.* **2004**, *151* (4), A571-A577
- [98] H. Randriamahazaka, K. Asaka, *J. Phys. Chem. C*, **2010**, *114* (41), 17982-17988
- [99] M. Schönleber, E. Ivers-Tiffée, *Electrochem. Commun.* **2015**, *61*, 45-48.
- [100] J. Bisquert, L. Bertoluzzi, I. Mora-Sero, G. Garcia-Belmonte, *J. Phys. Chem. C* **2014**, *118* (33), 18983-18991.

국 문 초 록

현대 사회에 대두되고 있는 주요 에너지 문제를 해결하기 위해서 고부가기치 화합물 및 에너지 전환 전기화학 반응 시스템 및 촉매에 대한 연구가 활발하게 이루어지고 있다. 수소 에너지는 친환경적인 특성으로 인해 차세대 에너지원으로 주목 받고 있다. 특히, 물 전기 분해는 기존 수소 에너지 생산 방법론과 달리 이산화탄소와 같은 환경을 저해하는 부산물이 생성되지 않는다는 장점을 가지고 있다. 하지만 물 전기 분해 시스템의 반쪽 산화 반응인 산소 발생 반응의 높은 과전압은 물 전기 분해 기술의 산업화를 위해 해결해야 되는 우선 과제로 여겨지고 있다.

산소 발생 반응의 과전압을 줄이기 위해 연구 초기에는 활성도가 높은 이리듐, 루테늄과 같은 귀금속 기반의 전기화학 촉매들이 보고되었지만, 귀금속의 희소성으로 인해 전이금속 기반 촉매들이 활발하게 연구되고 있다. 한편, 자연계에서 광계 II에 존재하는 칼슘 망간 클러스터는 어떤 인공 촉매 보다도 뛰어난 산소 발생 효율을 보인다. 이에 착안하여, 칼슘 망간 클러스터의 구조적 특징들을 모방한 망간 기반 촉매들이 개발되었지만, 망간 기반의 인공 촉매들은 성능이 좋지 못하다고 보고되고 있다.

이를 해결하기 위해, 10 nm 이하의 망간 산화물 기반 나노 입자를 합성하여 망간 기반 인공 촉매들 중 매우 뛰어난 활성도를 달성하였고, 실시간 분광학적 분석법을 통하여 망간 산화물 나노 입자의 다른 망간 기반 인공 촉매들과는 다른 독특한 물 산화 반응 메커니즘을 규명하였다. 이런 우수한 망간 산화물 나노 촉매에서의 물 산화 전기화학 반응을 심도 있게 이해하기 위해서는 전도성 기판 위에 나노 입자가 펠름 형태로 구성되어 있는 전극 구조에서 일어나는 다양한 현상들을 이해하는 연구가 중요하다. 본 연구에서는 전기화학 임피던스 분광법을 적용하여 망간 산화물 나노 입자로 이루어진 펠름 형태의 전극에서

일어나는 다양한 전기화학 현상들을 이해하고자 한다.

Chapter 2에서는 망간 산화물 나노 촉매 전극의 임피던스 분석에 적합한 회로 모델을 설계하고, 임피던스 데이터를 피팅하여 주요 반응 동역학적 인자들을 도출하고자 한다. 본 연구에서 제안하는 회로 모델을 통해 망간 산화물 나노 촉매 전극에서 일어나는 전자 전달 현상과 표면 반응 현상을 분리하였고, 전자 전달 저항과 표면 반응 저항의 비교를 통해 촉매 전체 성능에 크게 영향을 미치는 인자를 평가하였다. 그리고 H/D 동위원소 실험을 통해 전자 전달 과정에서 양성자(H^+)가 관여함을 증명했다. 더 나아가, 필름 형태의 전기화학 촉매의 반응속도상수(k) 측정을 아직 전기화학 촉매 분야에서 명료하게 해결되지 않은 과제로 여겨지고 있는데, 임피던스 분석 기반의 계산법을 제안하였다.

Chapter 3에서는 촉매 표면과 전해질로 이루어진 계면 사이에서 일어나는 전하 충전 현상을 이해하기 위하여 복소수 캐패시턴스 분석법을 시도하였다. 특히 망간 산화물 나노 촉매는 산소 발생 반응 도중 표면의 망간 산화가수가 Mn(II)부터 Mn(IV)까지 변화하기 때문에 전하 충전 현상을 이해하는 것은 주요하다. 복소수 캐패시턴스에서 실수 캐패시턴스 변화를 통해 실제로 촉매와 전해질 사이 계면에서 일어난 전하 충전 현상을, 허수 캐패시턴스의 변화를 통해 촉매 반응을 통하여 충전된 전하의 소진 현상을 이해하였다.

종합적으로, 본 연구에서는 전기화학적 임피던스 분광학적 분석법을 통해 망간 산화물 기반 나노 촉매 전극에서 일어나는 다양한 전기화학적 현상들을 이해하였다. 이 분석법은 망간 산화물 나노 촉매 전극뿐 만이 아니라 다양한 전기화학 반응 및 촉매 전극들에 적용하여 성능 및 메커니즘에 대한 심도있는 분석을 가능케 할 수 있을 것으로 기대한다.

주요어: 물 전기 분해, 산소 발생 촉매, 망간 산화물 나노 입자, 전기화학적 임피던스 분광법, 복소수 캐패시턴스 분석법

학 번: 2015 – 20828

감사의 글 (Acknowledgement)

‘연구’라는 것을 경험해보지 않고 마냥 설레는 마음으로 석·박사 통합 학위 과정을 시작한지 어느덧 6년이 시간이 지났습니다. 이 시간이 결코 순탄치만은 않았지만 훌륭한 교수님과 좋은 동료들의 도움으로 학위 과정을 마무리할 수 있게 되었습니다. 이 뿐 만이 아니라, 필요한 순간마다 공동 연구들을 통해 인연을 맺게 된 훌륭하신 분들 덕분에 연구를 행복하게 수행하였고 많은 것들을 배울 수 있었습니다. 지난 학위 기간을 돌아보면서, 저에게 도움을 주신 분들에게 감사의 글을 적습니다.

제일 먼저, 20대 중후반의 6년이라는 시간 동안 연구적으로, 그리고 그 외적으로 성장시켜주시고, 정말 많은 도움을 주신 남기태 지도 교수님께 진심으로 감사드립니다. 교수님께 가르침을 받으며, 연구실에서 유익한 경험들을 할 수 있었던 것은 제 인생의 큰 축복이었습니다. 입학부터 전기화학적 물 산화 반응 관련 연구 분야를 소개시켜 주시고, 이에 대해 연구하며 많은 것들을 배우고 경험할 수 있었으며, 많은 훌륭한 선, 후배들의 도움을 받을 수 있었습니다. 지난 시간을 돌아보면, 낮은 연차부터 꾸준히 해외 학회를 보내주시고, 뛰어난 해외 연구자들과 공동 연구를 했던 것은 저에게 매우 값진 경험이었습니다. 그리고 힘든 일이나 고민이 있을 때마다 신경써주시고, 격려해주신 덕분에 의미있는 연구실 생활을 할 수 있었습니다. 진심으로 감사드립니다.

학위 과정 중 많은 교수님들께 지도를 받을 수 있어서 영광이었습니다. 먼저, 학위 논문 심사위원장을 허락해주신 장호원 교수님께 진심으로 감사드립니다. 심사 기간 동안 유익한 커멘트들 주시고 격려해주셔서 진심으로 감사드립니다. 2018년 일본에서 학회 참석하고 교수님과 같은 비행기로 돌아온 적이 있었는데, 그 당시 편안한 분위기에서 따뜻한 말씀들을 해주셔서 힘이 되었습니다. 그리고 심사 과정에서 필름 타입의 heterogeneous 촉매 소재 성질 관점에서 유익한 커멘트들을 주셔서 이렇게 학위 과정을 마무리할 수 있게 되었습니다. 그리고 심사위원을 흔쾌히 수락해주신 김진영 교수님께서도 감사드립니다. 미래소

재디스커버리 과제를 추진하면서 여러 요청 메일을 드릴 때마다 친절하게 회신해 주셔서 감사합니다. 그리고 심사 과정에서도 전기화학 임피던스 분석 연구에 대한 조언들을 주셔서 졸업 논문을 작성하는 과정에 도움이 많이 되었습니다. 그리고 과제 작업 관련해서 자주 연락드렸던 이민형 교수님께도 감사 인사를 드립니다. 수년 동안 과제 작업으로 자주 연락드렸는데 항상 따뜻한 격려해주신 것이 기억납니다. 제 연구 주제 의미에 대한 본질적인 커멘트들을 주시고 개선 방안들도 가르쳐주셔서 감사드립니다. 최창혁 교수님께도 심사 위원을 수락해주세요서 진심으로 감사드립니다. 심사 과정에서 주신 전기화학 촉매의 reaction kinetic 관점에서의 통찰력 있는 조언들을 얻을 수 있었습니다.

학위 과정 기간 동안 공동 연구로 큰 도움을 주신 여러 교수님들과 박사님들께 진심으로 감사드립니다. 먼저 저의 임피던스 분석 논문 작업에 도움을 주셨던 이종숙 교수님께 진심으로 감사 인사를 드립니다. 처음 전기화학적 임피던스 분석에 대해 공부할 때 생소하였는데 뭘 때마다 여러 질문들에 대해 자세히 가르쳐 주시고, 직접 방문하였을 때에도 따뜻하게 환대주시고, 머물러 있는 동안 피팅 분석 방법론에 대한 많은 가르침을 주셔서 진심으로 감사드립니다. 그리고 포항가속기 연구소의 김민규 박사님께 감사드립니다. XAS 분석 관련하여 아낌없는 조언과 적극적으로 도와주셔서 좋은 실험 결과들을 얻을 수 있었습니다. 저도 학위 과정 기간 동안 도움을 받았던 여러 교수님과 박사님들처럼 누군가에게 도움이 될 수 있는 연구자가 될 수 있도록 끊임없이 성장하겠습니다.

학위 과정을 훌륭한 연구실에서 배울 점이 많은 동료들과 함께 할 수 있었던 것은 큰 축복이었습니다. 부족한 저를 적극적으로 도와주셔서 진심으로 감사드립니다. 짧게나마 한 번씩 감사 인사를 전합니다.

연구실 선배이자, 배울 점이 많은 승학아, 힘든 순간마다 필요한 조언을 해주고 큰 도움을 주어서 진심으로 고마워. 너도 힘든 부분이 있을텐데, 도움을 줬던 만큼 도움이 되지 못한 것 같아서 미안한 마음이 있어. 항상 좋은 일들 가득하고 원하는 것들이 순조롭게 이루어지길 기원할게. 나의 얘기를 잘 들어주는 석아 작년 너 옆자리에서 연구할 수 있어서 즐거웠어. 졸업 준비할 때 옆에서 격려해주고 응원해줘서 고마워. 준비하고 있는 진로에 좋은 일들 가득하길 기원

할게. Dr. Bala, thank you for your contribution to our laboratory. I wish you successful research and happiness. 연구와 다양한 분야에서 해박한 경도아, 예전에는 일상적인 대화를 자주 했었던 것 같은데, 자리가 멀어진 후에는 그때 보다는 자주 교류하지 못했네. 지금 하고 있는 연구들에서 좋은 결과 맷길 바라고 응원해. 긍정적이고 항상 친절한 정석아, 물 산화 반응 연구를 함께 할 때가 떠오르네. 너의 좋은 마음과 여려 경험들이 지금 하고 있는 연구에 큰 도움이 되길 바라고 응원해. 나와 함께 물 산화 팀에서 오랫동안 연구한 강희야, 그동안 수고를 많이 했던 것만큼 작년부터 좋은 결실들 맺고 있는데 축하하고, 끝까지 건강하게 학위과정 마치길 진심으로 바랄게. 다양한 분야에 대해서 해박한 상원아, 여러 연구 분야를 경험하고 카이랄 나노 입자 연구에 집중하여 훌륭한 연구를 하는 모습이 멋지고 대단하다고 느꼈어. 앞으로 지금처럼 좋은 연구하길 기원해. 어떤 부탁이든 항상 긍정적으로 들어줘서 고마운 승우야, 지금 집중하고 있는 연구들이 좋은 성과들로 이루어지길 진심으로 바라고, 항상 응원하고 있어. 나와 함께 졸업을 준비한 남현아, 너와 함께 준비하면서 많이 의지했는데 정말 고마워. 포닥으로의 연구실 생활과 앞으로의 진로도 항상 응원할게. 이산화탄소 환원 연구의 주축인 준호야, 연구실 입학 후부터 정말 열심히 연구하고 있는데 좋은 성과들 있을 것이고 원하는 진로로 이루어지길 기원해. 연구실에서 밝은 에너지를 전파하는 정은아, 연구실 생활하면서 많이 교류하지는 못했던 것 같은데, 앞으로도 주변 사람을 밝게 해주면서 너도 행복하고 훌륭한 연구실 생활하길 바래! 항상 열심히 노력하는 령명아, 내가 옆에서 지켜봤을 때는 잘하고 있으니까 끝까지 포기하지 말고 원하는 바를 이루길 바래. 열정 넘치고 똑똑한 윤호야, ECS 학회로 미국에 함께 갔었던 것이 기억나네. 덕분에 즐겁게 잘 다녀왔었어. 앞으로 연구실 생활에 꽂길 있길 바랄게. 센스 넘치고 주변을 잘 배려하는 혜온아, 지금처럼 긍정적인 성격과 꾸준함으로 연구하면 원하는 바를 이룰 수 있을거야. 응원할게. 모든 일에 적극적으로 도와주는 무영아, 다양한 업무들을 부탁했었는데 항상 잘 도와줘서 고마워. 묵묵하고 꾸준한 원일아, 너의 노력과 고생들이 좋은 결과로 이루어지길 바랄게. 작년에 나와 함께 연구한 창완아, 함께 좋은 성과를 냈으면 좋았을 텐데 그러지 못해서 미안해. 항상 많이

응원하고 있으니까 종종 연락하며 지내자. 밝은 에너지가 넘쳐났던 다해야, 졸업 너무나도 축하하고 행복한 앞길 열리길 바랄게. 준호와 함께 항상 열심히 실험하는 규민아, 많은 교류는 못했지만 연구실 생활과 이후 진로에 좋은 일 가득 하길 응원해. 능력도 많고 항상 솔선수범하는 예찬아, 연구실 생활에 빠르게 적응하고 연구하는 모습이 참 대단하다고 생각해. 이 모습 변치 않고 원하는 꿈을 이루길 기원해. 주위 사람들에게 리액션이 좋고 친절한 정원아, 1년 동안 보여준 연구에 대한 열정과 성실함이 정말 대단한 것 같아. 잘하고 있으니까 낙담하지 말고 원하는 진로를 성취하길 바랄게. 연구실 적응이 정말 빠른 영인아, 신입생임에도 불구하고 정말 열심히 하고 잘하고 있는데 이에 맞는 좋은 성과들도 있을 거라 확신해. 선배들에게 항상 예의 바른 성호야, 주변에 긍정적인 에너지를 전해줘서 고맙고, 성공적이고 의미 있는 연구실 생활하길 응원할게. 올해 입학하여 잠깐 함께 생활한 정현, 창현아, 마지막에 너희를 알게 되어 좋았고, 너희의 연구들과 연구실의 발전이 기대되는 것 같아. 그리고 연구실 인턴 생활을 하는 분들도 모두 힘내셔서 원하는 꿈들 성취하시길 응원합니다. 덧붙여서, 박현주 선생님께도 규모가 큰 연구실의 행정적인 부분을 성실히 지원해주세요, 진심으로 감사드립니다.

그리고 저의 부족한 부분들을 채워주시고 격려해주신 많은 선배님들께 감사 인사를 전합니다. 제 사수로서 정말 많은 것들을 가르쳐주신 경석이 형, 형 연구실의 발전과 가정이 형통하길 진심으로 기원합니다. 종종 연락드리겠습니다. 찾아뵐 때마다 따뜻하게 격려해주신 육 형, 본받을 점이 많은 찬우 형, 연구실 밖에서도 후배들을 응원해주시고 조언해주셔서 감사드립니다. 그리고 다음 스텝을 위해 열심히 연구하고 계시는 혜은 누나, 희윤이 형, 효용이, 유경이, 우제도 좋은 연구와 원하는 시기에 평탄한 진로가 열리길 응원합니다. 그리고 졸업 후 진로에 대해 조언해준 재훈, 기동, 영혜, 윤영에게도 감사드립니다. 그리고 도와주신 많은 선배님들에게 감사드리고, 선배님들처럼 저도 연구실 후배들에게 도움을 주는 선배가 되겠습니다.

마지막으로 저에게 너무나도 큰 힘이 되었던 가족들에게 감사 인사를 드립니다. 현덕아 연구실 생활을 하며 너를 만날 수 있었던 것은 정말 큰

행운이었고, 내가 힘들어하던 시기에 버팀목이 되어줘서 정말 너무 고마워. 나도 너에게 그런 사람이 될 수 있도록 성장할게. 아버지, 어머니의 기도와 응원이 없었으면 대학원 생활을 이렇게 마무리할 수 없었습니다. 늦은 나이까지 많은 지원을 받고 걱정 드린 것을 효도로 보답 드리겠습니다. 윤미야, 너도 항상 수고 많고, 앞으로의 사회생활 파이팅해. 결혼 후 항상 기도로 응원해주신 아버님, 어머님께도 정말 감사드립니다. 기도해주시는 것처럼 행복하고 올바른 가정을 위해 끊임없이 노력하겠습니다. 그리고 처남의 평탄한 앞길을 위해서도 기도하고 응원합니다. 그리고 저희 가정을 위해 기도해주시는 외할머니, 할머님께도 감사드리고, 저희 가정을 응원해주시는 많은 친척들에게도 감사 인사를 드립니다. 서로 사랑하고 주변에 좋은 영향을 끼치는 가정을 이루겠습니다.

제게 도움주신 모든 분들에게 다시 한번 진심으로 감사 인사를 드립니다. 항상 좋은 일들 가득하시길 바랍니다.

2021년 2월

서 흥 민